博士論文

(題目)

Power distribution system voltage control using customer air-conditioning facilities

令和4年度

岐阜大学大学院工学研究科
工学専攻

氏名：IQBAL ASIF

指導教員：CHUZO NINAGAWA

Abstract

In recent years, more and more Distributed Energy Resources (DER) have been introduced into the electric distribution networks, raising concerns about destabilization of the voltage. The use of quick charging stations for electric vehicles creates an extra challenge for the operation of the distribution network due to the abrupt load spike during their charge. The significant drawbacks of the higher DERs integration and quick charging stations are rapid voltage rise and fall. Because it is difficult to predict where and when the voltage change would occur, handling it just on the substation side would require a huge investment for installing the voltage control devices.

Traditionally, the reactive power support devices such as capacitor banks, Step Voltage Regulator (SVR), Static Synchronous Compensator (SATCOM), etc., are used to handle the voltage violations. However, some of these devices respond slowly, while others are quick but fixed in one place, not scattered over the distribution network.

For managing the DERs, research is progressing on Distributed Energy Resource Management System (DERMS) that maintains the grid voltage by controlling the output of the DERs which are equipped with smart inverters. It controls the DERs remotely through droop curves from the utility control center. To date, DERs such as PV and BESSs have been considered as resources of DERMS Volt-Var droop curve control. These DERs are installed at a fixed location and use their own droop curve, that is, these DERs are not treated as a cluster.

The objective of this research is to develop a control method for reactive power by using building multi-type air-conditioners that can realize the reactive power control from consumer's load in future power grid. In addition, another aim is to design a system for performing the reactive power demand response from DERMS without significantly degrading in the original function of costumer's load.

Recently, the technology of controlling the customer load's reactive power to stabilize the power distribution system has been attracting attention. Since building multi-type air-conditioners are widely installed in office buildings, they have the potential to participate in distribution system stabilization if they can fulfill the request of the reactive power demand response (Var Demand Response: VarDR).

This research proposes a new approach of reactive power demand response using group of buildings (cluster) equipped with building multi-type air-conditioners which are neighboring the feeder location where a voltage violation has occurred. For introducing building multi-type air-conditioner as reactive power support device, the set of operation modes are defined for the active converter built-in each air-conditioner to inject/absorb the reactive power.

Next, to preserve the original function of building multi-type air-conditioners, a reactive power allocation algorithm is proposed which allocate the reactive power to each air-conditioner taking into account the air-conditioning load and comfort. For forming the clusters, a Voltage Load

Sensitivity Matrix (VLSM) is formulated using line parameters to decide the target nodes that will help in recovering the voltage when the problem's location changes.

In case of VarDR, which is presented in this research, there are two distinct challenges for implementation of DERMS control. First, because VarDR clusters exist in different locations, the DERMS center has to select clusters at effective locations according to the current voltage distribution problem. Second, because a cluster consists of a large number of air-conditioners that are cost-sensitive, it is desirable to concentrate all the DERMS droop curve functionalities within an aggregator, that is, to leave air-conditioners in off-the-shelf configurations.

In this research a new method is proposed for implement a DERMS Volt-Var droop curve control system with VarDR for building multi-type air-conditioner clusters. The novelty of this method will be to select clusters near the node with a voltage problem and to use a reference node voltage for a single droop curve for the whole cluster.

An integrated simulator has been developed combining the model of air-conditioner's transient behaviors and a model of the standard urban distribution system. In addition, in order to demonstrate the usefulness of VarDR with DERMS control, a model scenario was created in which the voltage violations occurred due to the change in DERs output in a short period of time, and conducted an experiment using a DERMS real-time simulator.

Furthermore, an example microgrid model has been developed and VarDR applied. Simulations are conducted to investigate whether VarDR could support Grid ForMing (GFM) inverter that are saturated near the rated capacity.

The simulation result has shown, for example, a neighboring cluster of 25 air-conditioners in 5 office buildings continued the aggregated reactive power injection of approximately 400 kVar for 10 minutes while maintaining room-temperatures within the comfort range. In addition, results show, for example scenario, the reactive power can be supplied without deviating from set temperature limit for 30 minutes with VarDR DERMS Volt-Var droop curve control.

The main findings are as following.

① The VarDR method uses only everywhere-existing equipment i.e. building multi-type air-conditioners; consequently it can select an ad hoc cluster of buildings neighboring the problematic location in the distribution system.

② In model scenario, the VarDR method can utilize approximately 86% of maximum reactive power from the active converter built-in the air-conditioner while maintaining comfort within ±1.0 ℃ deviation from the set point temperature.

③ The proposed system design of DERMS Volt-Var control for VarDR effectively calculate the target reactive power and distributes it to the aggregators using proposed allocation algorithm while maintaining room comfort within set temperature limit.

This research is valuable in promoting the use of costumer’s existing equipment to tackle with issues brought on by DERs and EVs, and in realizing a society with low CO2 emissions.

Table of Contents

Chapter 1 Introduction

This chapter explains the motivation and background of this research. The contribution of this research in countermeasures of global warming is also elaborated. Finally, the objectives of this research are listed.

１．１ Background of this Research

Global warming countermeasures are the global issue, and the Paris Agreement [1] agreed in 2015 set a common long-term global goal of limiting the global warming less than ２ ℃. Similar to other countries, Japan has also developed a global warming countermeasures plan and set a national goals of reducing greenhouse gas emissions to ２６% below the 2013 level by FY2030 and ８０% below by FY2050 [2]. According to International Energy Agency, Japan met its 2020 climate change mitigation target ahead of time [3]. The electric power sector plays a major role in achieving these goals and the plan aims for strongly promotion of energy conservation, maximum introduction of renewable energy and introduction of electric vehicles.

When Distributed Energy Resources (DER) such as solar power and wind power are introduced in large quantities, the flow of electricity will become bidirectional, flowing from the consumer-side to the grid [4]-[6]. Furthermore, the output of renewable energy depends on weather changes, etc., [7]-[9], making it difficult to maintain the voltage within acceptable range [10]-[12].

On the other hand, the use of quick charging stations of electric vehicles adds another challenge to the operation of distribution networks because of the abrupt load increase during their charging. The serious weaknesses of the higher Distributed Energy Resources (DER) integration and quick charging stations are the rapid voltage rise and fall, respectively.

So far, the voltage control has traditionally been performed with reactive power support in electric power distribution networks [13]. The traditional reactive power support devices are capacitor banks, Step Voltage Regulator (SVR), Static Synchronous Compensator (SATCOM), etc., as shown in Fig. 1.1. Capacitor banks provide the reactive power support on slower timescale. Studies suggest that the traditional reactive power support devices and techniques cannot mitigate the effect of high penetration of renewable energies [14]. Voltage control on fast time scale is necessary.

For the fast countermeasures, so-called smart inverters have been introduced [15]. Many approaches recommended in the literature suggest that smart inverters connected to DERs should,

to some extent, have some extra power capability to inject or absorb the reactive power for voltage control. Smart inverters are excellent controllable resources because they can vary their active and reactive power in response to a remote command and actively manage the voltage at the connecting point. Smart inverter control on a fast timescale has been studied in some recent research [16]-[18].

Consequently, another possible method is to utilize the costumer facilities to provide reactive power support to the power grid. Many modern buildings are equipped with Building Energy Management System (BEMS) that are capable of monitoring and adjusting their power consumption. Many researchers, in literature [19]-[24], have explored the use of building air-conditioning systems and other Thermostatically Controlled Loads (TCLs) to provide active power management services to the grid, that is called Demand Response (DR).

Among these, building air-conditioning systems account for approximately 40% of the total power consumption of a customer's building [25], making them a good candidate as a target load for demand response. Building air-conditioning systems can be broadly classified into two types: centralized air-conditioning systems, in which a turbo chiller is driven in the basement, and building multi-type air-conditioning systems [26], in which a compressor is driven by an inverter

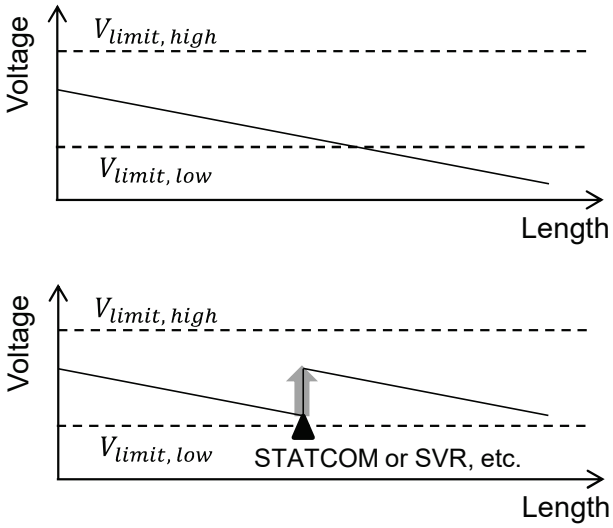

Fig. 1.1 Traditional grid-side voltage control with traditional voltage control device(s)

in an outdoor unit installed outdoors.

This research focused on the control of building multi-type air-conditioners. The reason for this is that building multi-type air-conditioners are capable of fine control of inverter-driven loads and are installed in large numbers in office buildings of a wide range of sizes. As an example, according to statistics compiled by the Japan Refrigeration and Air Conditioning Industry Association [27], there are approximately 1.52 million units (13 years accumulated units) of building multi-type air-conditioners installed in Japan. As well as, 1.80 million units of building multi-type air-conditioners are annually shipped globally [74]. Fig. 1.2 shows the annually shipped outdoor units of building multi-type air-conditioners in different regions of the world.

In [28], author presented the reactive power support with centralized air-conditioning system. In that research the author assumed simple control, i.e., just ON/OFF of air-conditioner. Also, the adjustment of power consumption and consumer's comfort has not been considered.

So, the potential benefits of reactive power support from building multi-type air-conditioners and real-time Volt-Var control system were not discussed in any of the previous research to the best of author's knowledge.

For managing the DERs, a new system control architecture called the Distributed Energy Resource Management System (DERMS) [29]-[33], which centrally controls and manages the

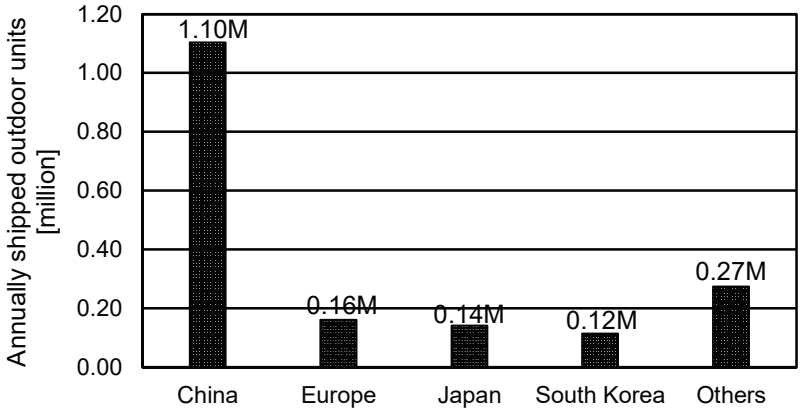

Fig. 1.2 Globally installed units of building multi-type air-conditioners; reference [74]

reactive power of distributed energy resources, has attracted attention. The core of this system is the Volt-Var droop curve control [34] and [35].

The concept of microgrid emerges from increasingly dominated DERs and emergency situations such as disaster or accident. Without substation, the DERs with Grid ForMing (GFM) inverters play the role as power source reference. This research also investigates whether it's possible to support continuous operation of saturated GFM inverter by reactive power demand response (VarDR) using costumer's air-conditioning facilities.

This research presents a method of reactive power demand response with building multi-type air-conditioners; formulates the relationship between active power consumption and reactive power of building multi-type air-conditioner; develops the reactive power allocation algorithm that takes consumer comfort into account; and designs a system architecture to perform the reactive power demand response from DERMS using advanced smart inverters functionality, i.e., Volt-Var curve control.

This research is valuable in promoting the use of costumer's existing equipment to tackle with issues brought on by DERs and EVs, and in realizing a society with low CO2 emissions.

1．2 Objectives of this Research

The objective of this research is to develop a control method for reactive power by using building multi-type air-conditioners that can realize the reactive power control from consumer's load in future power grid. To this end, this research will clarify the following.

① To present an idea of reactive power demand response with building multi-type air-conditioners.

② To develop the reactive power allocation algorithm that takes consumer comfort into account.

③ To design a system for performing the reactive power demand response from DERMS using advanced smart inverters functionality, i.e., Volt-Var curve control.

④ To apply the VarDR idea in mirogrid.

Chapter 2 Problem Description

This chapter describes the voltage problem in future power grid and the relationship between voltage and reactive power using Voltage Load Sensitivity Matrix (VLSM). VLSM shows that the voltage sensitivity coefficients will change as the problem location changes. Furthermore, the challenges are addressed which associated with consumer load facilities while participating in reactive power demand response program. The challenges with DERMS control for implement reactive power demand response are presented in the final section.

２．１ Voltage Violation Problem in Future Power Grid

In the study of power grids, voltage control of distribution networks has a significant position. Renewable energy source's intermittent nature results in rapid voltage changes that are challenging to manage and reduce the quality of the power.

Due to the abrupt load rise during their charge, using quick charging stations for electric vehicles presents an additional difficulty to the functioning of the distribution network. Rapid voltage rise and fall are, respectively, the significant drawbacks of quick charging stations and higher DERs integration.

Current utility-side voltage regulation cannot react quickly enough to voltage limit violation that may arise as a result of DERs power injection and EV charging. This is because it uses conventional voltage control devices like, SVR, On Load Tap Changer (OLTC), static capacitors, etc. Among the traditional voltage control devices, STATCOMs are quick enough but are fixed to specific locations in distribution networks. However, advances in power electronics technology and contemporary Information and Communication Technologies (ICT) open up new opportunities for managing and effectively integrating small scale generation at the distribution level.

An example voltage issue in the future power grid is shown in Fig. 2.1. As we can see, the

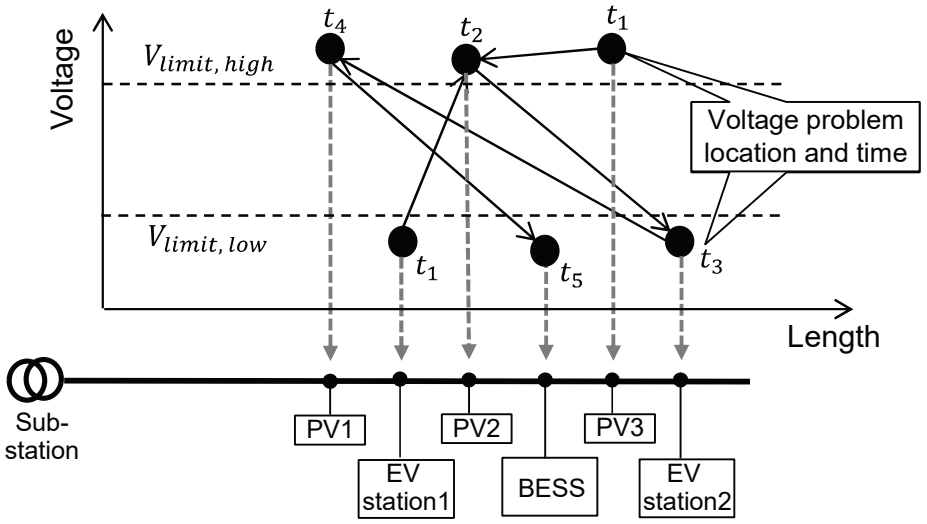

Fig. 2.1 Voltage volition problem based on location and time in future grid

voltage volition problem manifests itself at various times and locations. At t_1 at different locations, the voltage maximum and minimum limits may volatile simultaneously. At t_3 due to EV quick charging, the voltage minimum limit may volatile, and the next time t_4, the voltage maximum limit may volatile due to light load and high PV output.

A real world example, is shown in Fig. 2.2. In the United States, some consumers have started to rapidly switch charging/discharging every few minutes in units of hundreds of kW for trading in the electricity balancing market [36].

In the near future, as shown in Fig. 2.3, the centralized introduction of high voltage grid connected DERs for large scale commercial use will make the grid voltage distribution more complex, making it difficult to control the voltage of the 6.6 kV high voltage system. As a result, it also affects the low voltage system as well. Since it is difficult to predict where and when this voltage change will occur, it would require a huge investment in infrastructure to deal with it on

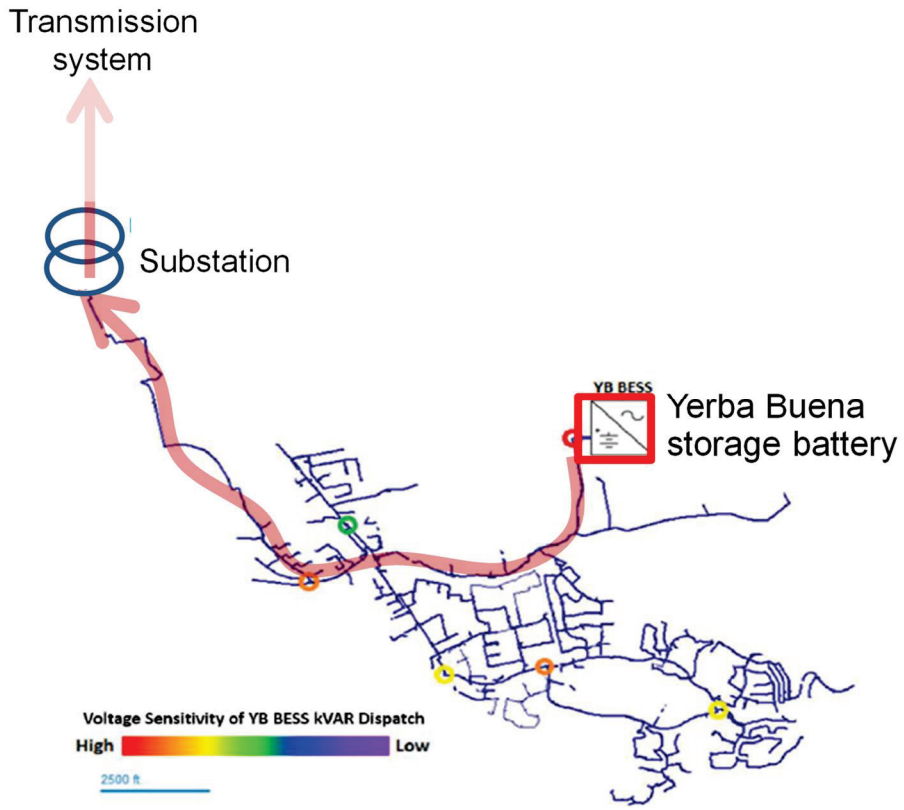

Fig. 2.2 Yerba Buena storage battery trading demonstration feeder; adopted from [58], Fig. 29

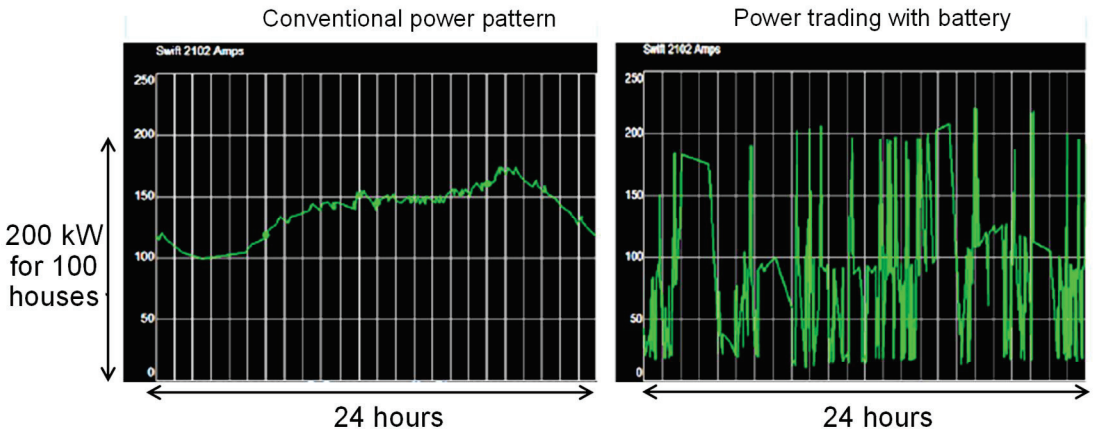

Fig. 2.3 Impact on feeder load when Yerba Buena storage battery participate in trading; adopted from [58], Fig. 12

the substation side alone. There is a concern that it will become difficult to deal with the voltage problem.

So, it is necessary to develop a voltage control which has two features: first, a fast response and second, locational flexibility in choosing the reactive power support devices that are near to the voltage problem point in the distribution network.

2．2 Formulation of Voltage and Reactive Power Relationship

In this section the node voltage and reactive power relationship in electric power network is formulated using Voltage Load Sensitivity Matrix (VLSM). A VLSM is developed using line parameters to decide the target nodes that will help for recovering the voltage when the problem's location changes.

Let's consider a three phase symmetrical, radial distribution network with N nodes and N line segments. Where the 'segment' is defined as the conductor between two nodes.

Let ΔU_m be the total voltage drop from source node to node m and V_s be the source node voltage. Considering the simple network as shown in Fig. 2.4, the voltage at node m can be expressed as Eq. (2.1).

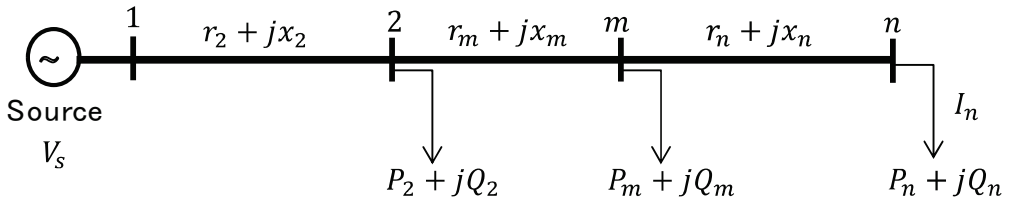

Fig. 2.4 Simple network

$$V_m = V_s - \Delta U_m = V_s - [\sum_{n=1}^{N} I_n . Z_{mn}] \tag{2.1}$$

Here, I is the load current at n node and Z is the impedance matrix of considered distribution network. The graph theory can be used to obtain the impedance matrix Z as reported in literature [37]. Using graph theory, the impedance matrix Z and length matrix L of considered distribution network can be expressed as Eq. (2.2).

$$Z = A.z_s.A^T \\ L = A.l_s.A^T \tag{2.2}$$

Here, A is called incidence matrix. Incidence matrix A is a square matrix, dimension $(N\text{x}N)$, whose store the topology or structure of the distribution network. z_s [Ω/km] and l_s [km] are the diagonal matrixes, dimension$(N\text{x}N)$, whose main diagonal elements are the complex impedances $(r + jx)$ of corresponding line segments and lengths of corresponding line segments, respectively. z_s can be represented in matrix form as Eq. (2.3).

$$z_s = \begin{bmatrix} r_{11} & \cdots & 0 \\ \vdots & \ddots & \vdots \\ 0 & \cdots & r_{NN} \end{bmatrix} + j \begin{bmatrix} x_{11} & \cdots & 0 \\ \vdots & \ddots & \vdots \\ 0 & \cdots & x_{NN} \end{bmatrix} \tag{2.3}$$

The elements of incidence matrix, a_{mn}, can be calculated using Eq. (2.4).

$$a_{mn} = \begin{cases} 1 & If\ n^{th}\ segment\ is\ in\ the\ path\ formed\ by\ source\ node\ and\ m^{th} node, \\ 0 & Otherwise \end{cases} \tag{2.4}$$

The rows (m) of incidence matrix represent the corresponding nodes and columns (n) represent

the corresponding line segments.

Impedance matrix is expressed in Eq. (2.5) as matrix form.

$$\mathrm{Z} = \begin{bmatrix} R_{11} & \cdots & R_{1N} \\ \vdots & \ddots & \vdots \\ R_{N1} & \cdots & R_{NN} \end{bmatrix} + j \begin{bmatrix} X_{11} & \cdots & X_{1N} \\ \vdots & \ddots & \vdots \\ X_{N1} & \cdots & X_{NN} \end{bmatrix} \tag{2.5}$$

Let's consider the constant power load model, so, the load current I at nth node is expressed as Eq. (2.6).

$$I_n = \frac{P_n - jQ_n}{V_n^*} \tag{2.6}$$

Substitute the Eq. (2.6) and impedance matrix Z as $(R + jX)$ in Eq. (2.1). And simplify it by assuming that only real component of complex voltage V^* is considered, while phase angles of node voltages are ignored. The phase angle quantity is ignored because the variation in phase angles between nodes is very small due short length of distribution network. So, we can obtain the node voltage expression as Eq. (2.7).

$$V_m \approx V_s - [\sum_{n=1}^{N} \frac{P_n . R_{mn}}{V_n} + \sum_{n=1}^{N} \frac{Q_n . X_{mn}}{V_n}] \tag{2.7}$$

In general, this type of expressions often be solved by using a numerical method, because, the node voltages are unknown other than source node. However, obtaining the voltage at each node using Eq. (2.7) is outside the scope of this research. This expression is only used in this research to obtain the VLSM matrix.

Let ΔV_m be the voltage variation as the difference between pre-disturbance voltage and post-disturbance voltage at mth problematic node. The ΔV_m can be estimated [38] by the real power change ΔP_n and reactive power change ΔQ_n at all nodes (i.e., $n = 1, \ldots, N$) followed by the sensitivity coefficients with respect to power modulation.

$$\Delta V_m = \sum_{n=1}^{N} \frac{\partial V_m}{\partial P_n} \Delta P_n + \sum_{n=1}^{N} \frac{\partial V_m}{\partial Q_n} \Delta Q_n \tag{2.8}$$

The derivatives $\frac{\partial V}{\partial P}$ and $\frac{\partial V}{\partial Q}$ can be seen as sensitivity coefficients.

The focus area of this research is to utilize the costumer facilities for voltage control. Active power is used to operate the consumer loads. Therefore, to avoid the disruption in original function of costumer loads, the $\frac{\partial V}{\partial P}\Delta P$ part of Eq. (2.8) is considered as fixed. So, Eq. (2.8) will be expressed as following.

$$\Delta V_m \approx \sum_{n=1}^{N} \frac{\partial V_m}{\partial Q_n}\Delta Q_n \tag{2.9}$$

As in [39], the relative voltage variation can be presented by multiply and dividing the V_m on right side of Eq. (2.9). And it can be expressed as Eq. (2.10).

$$\frac{\Delta V_m}{V_m} \approx \frac{1}{V_m}\sum_{n=1}^{N} \frac{\partial V_m}{\partial Q_n}\Delta Q_n \tag{2.10}$$

Considering the N number of node equations, Eq. (2.10) can be expressed in matrix form as Eq. (2.11).

$$\begin{bmatrix} \frac{\Delta V_1}{V_1} \\ \vdots \\ \frac{\Delta V_N}{V_N} \end{bmatrix} = \begin{bmatrix} \frac{1}{V_1}\frac{\partial V_1}{\partial Q_1} & \cdots & \frac{1}{V_1}\frac{\partial V_1}{\partial Q_N} \\ \vdots & \ddots & \vdots \\ \frac{1}{V_N}\frac{\partial V_N}{\partial Q_1} & \cdots & \frac{1}{V_N}\frac{\partial V_N}{\partial Q_N} \end{bmatrix} \cdot \begin{bmatrix} \Delta Q_1 \\ \vdots \\ \Delta Q_N \end{bmatrix} \tag{2.11}$$

The derivatives $\frac{\partial V}{\partial Q}$ of N nodes form a matrix and that matrix is called Voltage Load Sensitivity Matrix, S_q. The S_q matrix can be written as Eq. (2.12).

$$S_q = \begin{bmatrix} \frac{1}{V_1}\frac{\partial V_1}{\partial Q_1} & \cdots & \frac{1}{V_1}\frac{\partial V_1}{\partial Q_N} \\ \vdots & \ddots & \vdots \\ \frac{1}{V_N}\frac{\partial V_N}{\partial Q_1} & \cdots & \frac{1}{V_N}\frac{\partial V_N}{\partial Q_N} \end{bmatrix} \tag{2.12}$$

The elements of Voltage Load Sensitivity Matrix S_q are called sensitivity coefficients and, hereafter, will be denoted by α_{mn}.

Now, by taking the partial derivatives of Eq. (2.7) with respect to reactive power and considering the longitudinal parameters (i.e., line length), we can calculate the sensitivity coefficients α_{mn} as Eq. (2.13) and can obtain the Voltage Load Sensitivity Matrix, S_q.

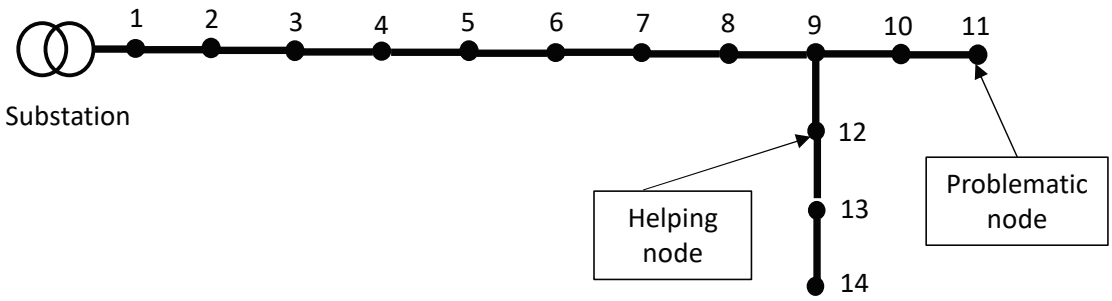

Fig. 2.5 An example of "problematic node" and "helping node" in a distribution network

$$\alpha_{mn} = \frac{1}{V_m}\frac{\partial V_m}{\partial Q_n} = -\frac{1}{V_m V_n}.X_{mn}.L_{mn} \tag{2.13}$$

Here, the term X [Ω/km] is the imaginary component of impedance matrix Z which can be obtained by Eq. (2.2).

The physical meaning of L_{mn} is that it is the sum of segment lengths that make the common path between nodes m and n from the source node. Similarly, X_{mn} is the sum of segment reactances that make the common path between nodes m and n from the source node. It can be summarized in Eq. (2.14). For example, considering the distribution network shown in Fig. 2.5, the problematic node $m = 11$ and the helping node $n = 12$.

$$\begin{aligned} X_{11,12} &= x_1 + x_2 + \cdots + x_9 \\ L_{11,12} &= l_1 + l_2 + \cdots + l_9 \end{aligned} \tag{2.14}$$

Therefore, the sensitivity coefficients, α_{mn}, can be expressed in a function form as Eq. (2.15).

$$\alpha_{mn} = f(V, \sum_{Path_c} x, \sum_{Path_c} l) \tag{2.15}$$

In Eq. (2.15), $Path_c$ is the common path helping node and problematic node from the source node. So, the sensitivity coefficients are the function of voltage, sum of segments reactance and sum of segments length. The sensitivity coefficients rely on both the helping node voltage and problematic node voltage. Also, regarding distribution network topology, the sensitivity coefficients depend on only the line segments that make the common path between helping node and problematic node from the source node.

２．３ Air-conditioner as Reactive Power Support Device

The demand response technology to utilize the costumer facilities for power systems supply and demand balance has been well studied. So far, DR was considered only for active power control.

Many studies have been conducted on demand response for building air-conditioning [40]-[42]. Some of them respond to real-time electricity rates in hours [43]-[45], some control the trade-off between electricity rates and room temperature comfort [46], and some use a linear model to represent the power dynamic characteristics of air-conditioners and adapt to real-time electricity rates [47]. However, all of these studies target centralized air-conditioning systems. For building multi-type air-conditioners, which are widely used in office buildings in Japan, there are studies on the adjustment of power consumption and comfort [48] and [49], but these studies did not deal with reactive power control.

Recently, however, costumer side reactive power control to deal with voltage fluctuation in distribution system has attracted attention [50]. Building multi-type air-conditioners are widely installed in office buildings, and considered to be a candidate of costumer side controllable load [51]. If the reactive power of these air-conditioners can be controlled from a utility control center, e.g., Distributed Energy Resource Management System (DERMS), it would be possible to develop the reactive power demand response for participating the distribution system voltage control.

The DERMS controls reactive power of demand side DER's devices so-called "smart inverters". In fact, demand side controllable loads driven by inverters could be subject of DERMS. Building multi-type air-conditioners may also have the potential to perform the reactive power control because their refrigerant compressor is driven by an inverter which is often combined with a standard active converter built-in the air-conditioner [52].

A variety of names has been used for this device such as "active filter", "active converter", or "PWM converter". Hereafter, it called as "active converter". Although the primary objective of the active converter is to reduce the harmonics of the input AC current. It also has the functionality of power factor control, in other words, reactive power control [53].

In [54], author reported that the active converter installation rate is more than 30% and increasing. Another paper [55] mentioned a possibility of utilize consumer products such as room air-conditioners for reactive power control. However, there is no detailed article which describes an implementation method of reactive power control by using the active converter built-in a building multi-type air-conditioner. Especially, regarding the balance with side-effect of room temperature, any concrete method of the reactive power target allocation to each air-conditioner has not been proposed so far.

This research proposes a concrete implementation method for reactive power demand response of building multi-type air-conditioners, it called “VarDR”.

The VarDR forms a cluster of several buildings which are close to each other in the distribution system. The advantage of the VarDR is that it is possible to select a “neighboring cluster” which is close to the voltage problem point in the distribution system and is effective for voltage recovery.

In addition, other studies on reactive power control using a built-in active converter in air-conditioners have been reported in [56] and [57]. These previous research concentrated on the idea of using the reactive power of air-conditioner inverters. No research has been carried out regarding the entire system control for VarDR aggregation by clustering building multi-type air-conditioners.

２．４ Preserve the Comfort of VarDR’s Participants

Similar to conventional demand response, the cooling performance of building multi-type air-conditioners is also declined during VarDR. So, the next challenge is to develop the VarDR allocation method which can taking into account the active power consumption and room temperature.

Figure 2.6 shows an example of reactive power injection/absorption and constraints on active power to a compressor, and the impact on air-conditioning performance (i.e., deviations in room temperature). As shown in Fig. 2.6, normally, the air-conditioner is operated at a power factor of

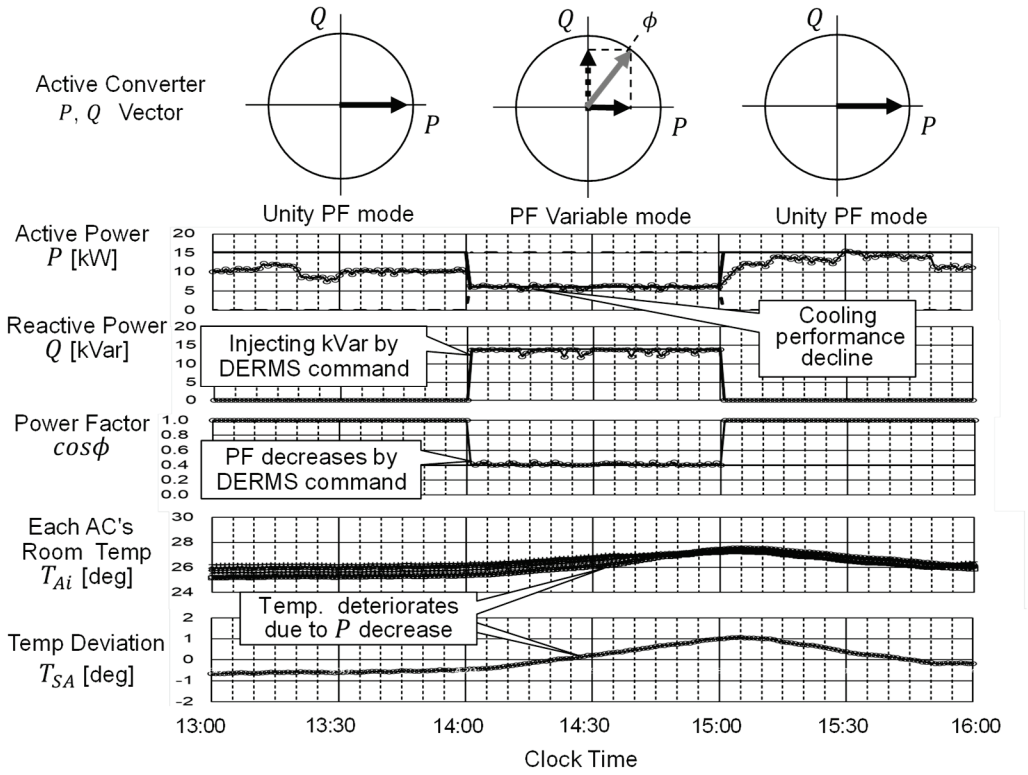

Fig. 2.6 Relationship between active/reactive power, power factor, and room temperature for an air-conditioner

unity. Thus, air-conditioning active power is not curtailed. However, when a reactive power inject/absorb command is received, as in the case of VarDR, the air-conditioning active power is curtailed depending on the control strategy. As a result, the air-conditioning capacity, which is the system's purpose, decreases and the room temperature rises.

When capacities of reactive power support devices are limited and the site of disturbance occurrence changes, the better idea may be to forming a cluster of reactive power support devices to deal with voltage violations.

The algorithm 1, shown in Fig. 2.7, explains how the cluster can be formed using VLSM. Let m be the problematic node, p be the participating node, N^p be the set of nodes which are willing to participate in VarDR event, Q_p^{cap} be the allowable capacity of pth participating node and cluster is denoted by C. So, C can be defined as: $C \subset N^p$.

Considering the example distribution network shown in Fig. 2.8, algorithm finds the cluster C

Algorithm 1: Cluster Forming

Input: Network data, N^p, Q_p^{cap} and V_i $(i = 1,2, \dots m, \dots N)$.

Output: Forming the cluster, $C \subset N^p$ and ΔQ_p.

1: **If** $V_{min} < V_m < V_{max}$ and $\Delta V_m \cong 0$ is violated **then**
2: Compute S_q, using Eqs. (2.12 and 2.13).
3: Calculate C_{idx} as Eq. (2.16).
4: Search, Max $\{C_{idx}(p)\}$, $p \in N^p$.
5: Calculate ΔQ_p as: $\Delta Q_p = \Delta V_m / \alpha_{mp}$.
6: **If** $\Delta Q_p < Q_p^{cap}$ **then**
7: Go to 1.
8: **Else**,
9: Set $\Delta Q_p = Q_p^{cap}$.
10: Update ΔV_m as: $\Delta V_m = \Delta V_m - \Delta Q_p . \alpha_{mp}$.
11: Go to 4.
12: **Else**, End and exit the whole algorithm.

Fig. 2.7 Cluster forming algorithm

to deal with voltage violation at mth problematic node while considering the allowable capacities and room temperature deviation of participating buildings. The inputs of algorithm are physical information of distribution network, i.e. line impedances, lengths and topology, set of participating nodes N^p, capacities of participating nodes Q_p^{cap} and node voltage V_i $(i = 1, 2, \dots, N)$. Nodes voltages are obtained by conducting the load flow using OpenDSS [64].

To visualizing the cluster forming, the cluster index C_{idx} is formulated as Eq. (2.16). The cluster index C_{idx} is the measure that take into account both the normalized sensitivity coefficient and temperature deviation factor of a building.

$$C_{idx}(n) = K_n . S_q(n) + T_{sc}^p \tag{2.16}$$

Here, C_{idx} is the cluster index of nth node , K_n is weighting factor of VLSM coefficients, $S_q(n)$ is VLSM coefficient of nth node and T_{sc}^p is temperature deviation factor of participating whole building. T_{sc}^p is formulated as Eq. (2.17).

$$T_{sc}^{p} = \left(T_{SA}^{max} - \sum_{b=1}^{B} \frac{T_{SA}^{b}}{B} \right)^{2} \tag{2.17}$$

Here, B is the total number of outdoor units in a building. T_{SA}^{b} is the room temperature deviation between set temperature and room temperature of bth outdoor unit, and T_{SA}^{max} is the maximum room temperature deviation.

Algorithm starts by taking the physical information of distribution network into account so that there exists no voltage violation. Then, assume that EVs doing the charging at mth node and the voltage violation is detected. So, the coefficients of VLSM matrix are calculated using Eq. (2.13).

Then cluster index C_{idx} is calculated considering the normalized VLSM coefficients and room temperature deviation factor T_{sc}^{p}. And find the node which has most heights C_{idx} with respect to problematic node m while considering the set N^{p}.

After that, determine the required reactive power change ΔQ_p at that node. If ΔQ_p is not available then set it to its allowable capacity and look for next most sensitive node with respect to m. This procedure is repeated until the voltage variation ΔV_m is reduced to an acceptable level. Finally, the voltage violation is checked and cluster C is formed.

Let's assume that all the buildings, in Fig. 2.8, can participate in VarDR event and the available

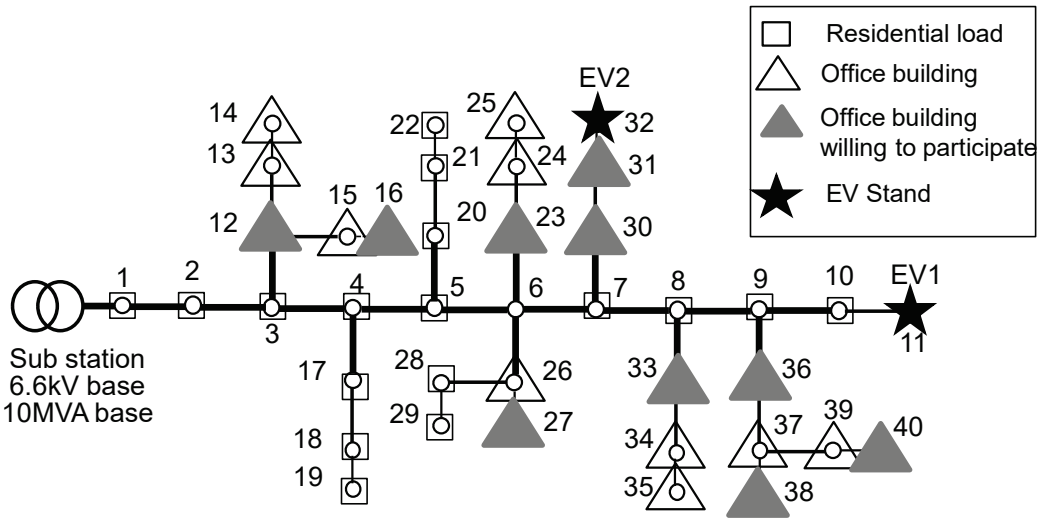

Fig. 2.8 An example distribution network with scattered office buildings

reactive power capacity Q_p^{cap} of each building is 100 kVar. DERMS ask the willingness from building for next 5 minutes VarDR frame. Suppose, 10 out of 19 buildings are willing to participate for next 5 minutes VarDR frame. So, total elements of set N^p are 10. Let $K_n = 40$, $T_{SA}^{max} = 1.0$, $T_{SA}^{b} = -1.0 \sim 0.0$.

2．5 Distributed Energy Resource Management System (DERMS)

For managing the DERs, a new system control architecture called the Distributed Energy Resource Management System (DERMS), which centrally controls and manages the reactive power of distributed energy resources. It controls the DERs remotely through droop curves from the utility control center, as shown in Fig. 2.9.

To date, DERs such as PV and BESSs have been considered as resources of DERMS Volt-Var droop curve control. These DERs are installed at a fixed location and use their own droop curve, that is, these DERs are not treated as a cluster.

In the case of VarDR clusters, which is presented in this research, DERMS implementation has two distinct problems. First, because clusters exist in different locations, the DERMS center

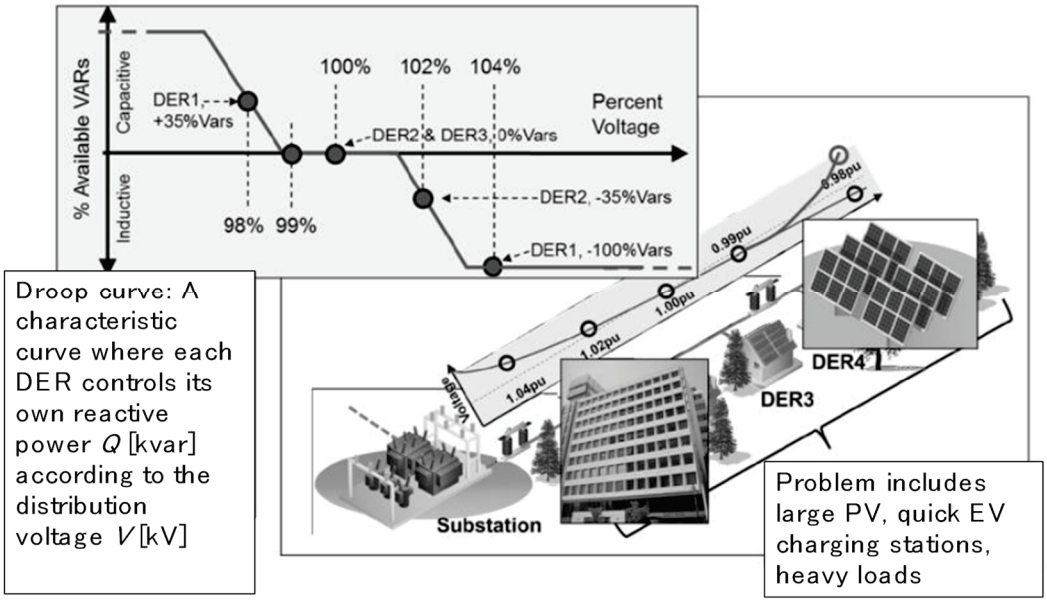

Fig. 2.9 Image of distribution system high voltage control by reactive power control of consumer DER; adopted from [59]

has to select clusters at effective locations according to the current voltage distribution problem. Second, because a cluster consists of a large number of air-conditioners that are cost-sensitive, it is desirable to concentrate all the DERMS droop curve functionalities within an aggregator, that is, to leave air-conditioners in off-the-shelf configurations.

For this purpose, it is necessary to develop a new method for implement a DERMS Volt-Var droop curve control system with VarDR for building multi-type air-conditioner clusters. The novelty of this method will be to select clusters near the node with a voltage problem and to use a reference node voltage for a single droop curve for the whole cluster.

The DERMS droop Volt-Var Control (VVC) is the most popular approach, due to its straightforward design and simple implementation. It was initially proposed in an EPRI technical study [60]. And since then, the IEEE1547 integration standard [61] has accepted it and widely utilized it. As in Fig. 2.9, local node voltage and inverter VAR injection are represented by the horizontal and vertical axes, respectively.

Additionally, this section explains how to determine the $f(V,Q)$, which is required to calculate the slope of the Votl-Var curve. The physical constraint $f(V,Q)$ describes the system voltage's sensitivity to reactive power. In order to determine $f(V,Q)$, consider thevenin equivalent circuit of an inverter in the distribution network in Fig. 2.10.

Let V be the magnitudes of the terminal voltage and θ be the phase angle of the inverter. Additionally, P and Q represent the inverter's active and reactive power outputs. The external impedance's magnitude and angle are represented by Z and φ, respectively. The equivalent

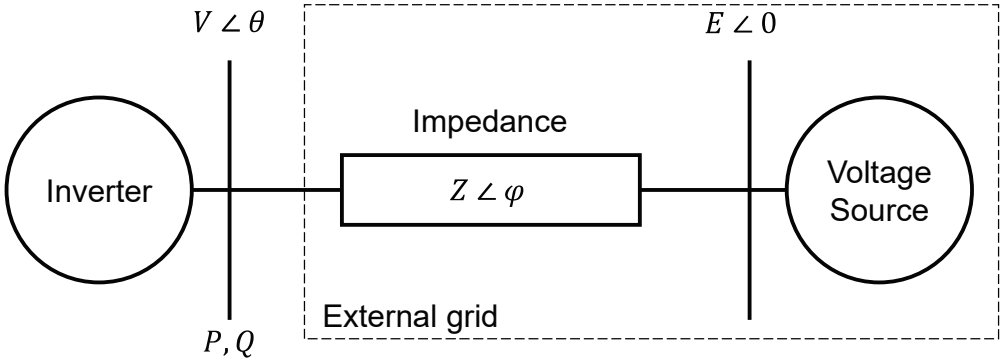

Fig. 2.10 Single inverter connected to the grid.; adopted from [59]

voltage source's magnitude of voltage is represented by E. For this inverter system, the power flow equation is as Eq. (2.18) as in [59].

$$\begin{cases} P = \dfrac{V^2}{Z}\cos\varphi - \dfrac{VE}{Z}\cos(\theta+\varphi) \\ Q = \dfrac{V^2}{Z}\sin\varphi - \dfrac{VE}{Z}\sin(\theta+\varphi) \end{cases} \tag{2.18}$$

These equations are transformed as Eq. (2.19).

$$\begin{cases} \cos(\theta+\varphi) = \dfrac{V}{E}\cos\varphi - \dfrac{PZ}{VE} \\ \sin(\theta+\varphi) = \sqrt{1-\cos^2(\theta+\varphi)} = \sqrt{1-\left(\dfrac{V}{E}\cos\varphi - \dfrac{PZ}{VE}\right)^2} \end{cases} \tag{2.19}$$

The relationship between the terminal voltage of the inverter and the reactive power output is expressed as Eq. (2.20).

$$Q = \frac{V^2}{Z}\sin\varphi - \frac{VE}{Z}\sqrt{1-\left(\frac{V}{E}\cos\varphi - \frac{PZ}{VE}\right)^2} \tag{2.20}$$

This relationship holds regardless of time whether the system is in a steady state or a transient phenomenon. However, only the steady state is considered in this research.

The droop VVC faces the two issues. First, because the droop Volt-Var control is so dependent on the droop (slope) parameter, choosing the wrong slope can result in control instability or voltage oscillations. Second, the trade-off between attaining control stability and a good set-point tracking performance. The droop design itself is the reason of this problem, which is inherent to the droop Volt-Var control.

Another challenge for DERMS VarDR is communication architecture. Fig. 2.11 illustrates centralized control, where all data is gathered in one place and decisions on the management of the entire distribution network are made by a central processor. The creation of effective DERMS control, which may distribute the jobs among numerous aggregator coordinators depicted in Fig. 2.12, is necessary to reduce the burden and cost.

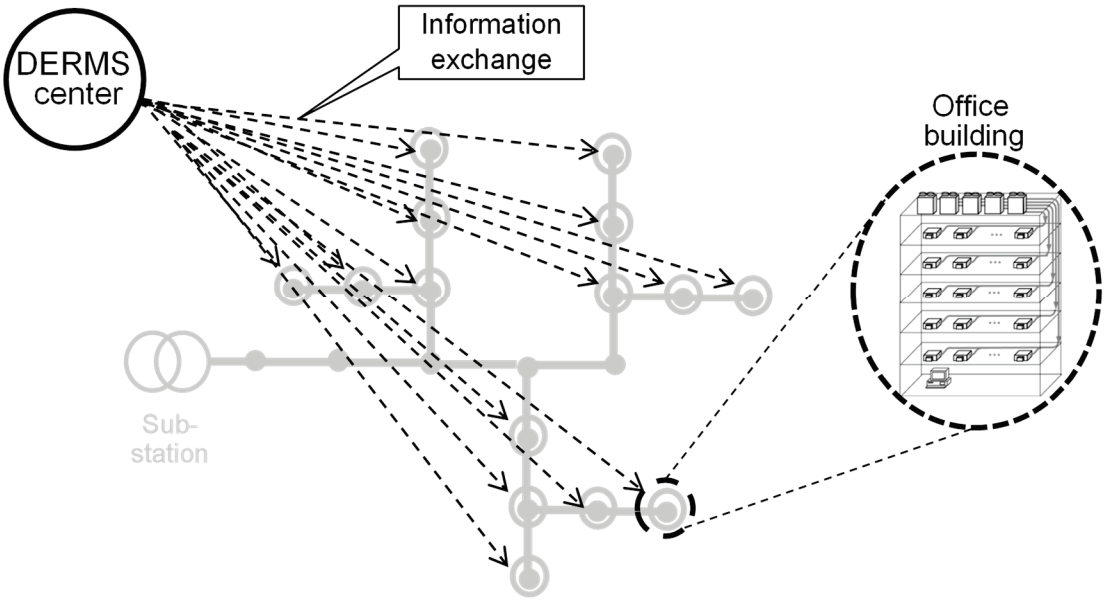

Fig. 2.11 Centralized DERMS control

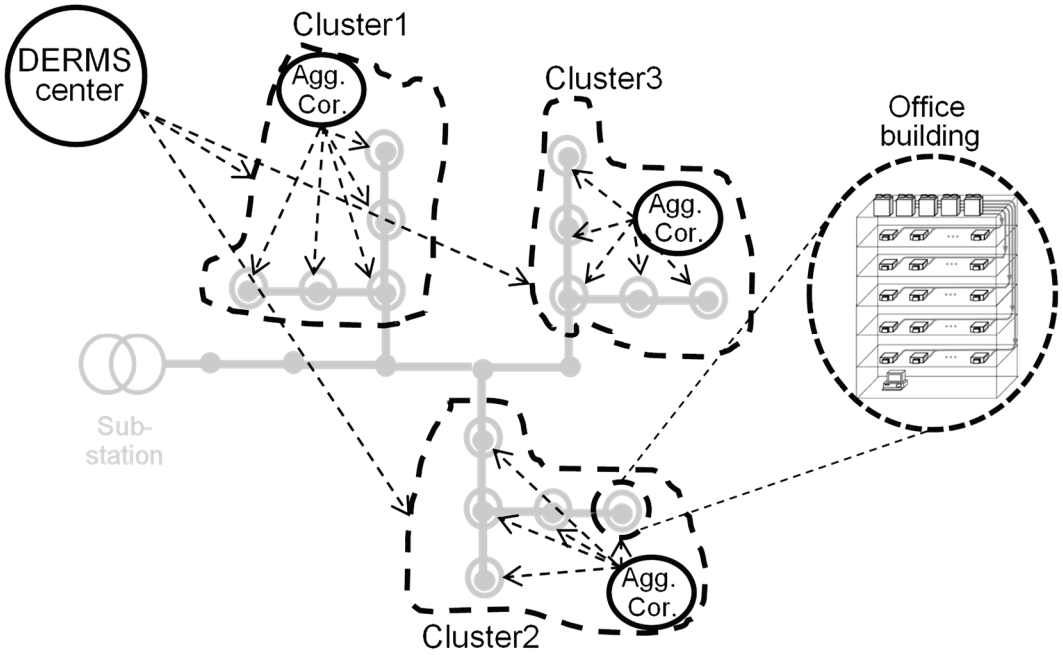

Fig. 2.12 Decentralized DERMS control; Agg. Cor. (Aggregator Coordinator)

Chapter 3 Reactive Power Demand Response

This chapter describes the idea of reactive power demand response of building multi-type air-conditioners. First, the relationship between power consumption and reactive power of building multi-type air-conditioner is explained. Then, an reactive power allocation algorithm is formulated and building multi-type air-conditioner model is described. Finally, for confirmation of reactive power demand response, the simulation results are described with some assumptions of simulation conditions.

３．１ Reactive Power Control of Building Multi-type Air-conditioners

３．１．１ Potential of Building Multi-type Air-conditioners

Building multi-type air-conditioners are widely used in medium-sized office buildings. Especially, in an urban area, thousands of building multi-type air-conditioners are installed in hundreds of buildings. Therefore, there is a potential to obtain a meaningful amount of aggregated reactive power for the distribution system voltage control.

Unlike inverters of photovoltaic power generation or power storage battery systems, the inverters built-in building multi-type air-conditioners have been considered to lack the functionality of control reactive power control. However, in recent years, more and more building multi-type air-conditioners are becoming equipped with active converter as shown in Fig. 3.1 as reported in [52] and [55].

These active converters are originally installed to suppress the harmonics on the AC input side. However, as the input current phase angle is freely adjustable by the active converter, the power factor can be controlled while suppressing the harmonics. Therefore, it is possible to control the injection/absorption of the reactive power to the grid [54].

However, due to restrictions on the minimum operating power factor and rated capacity of the

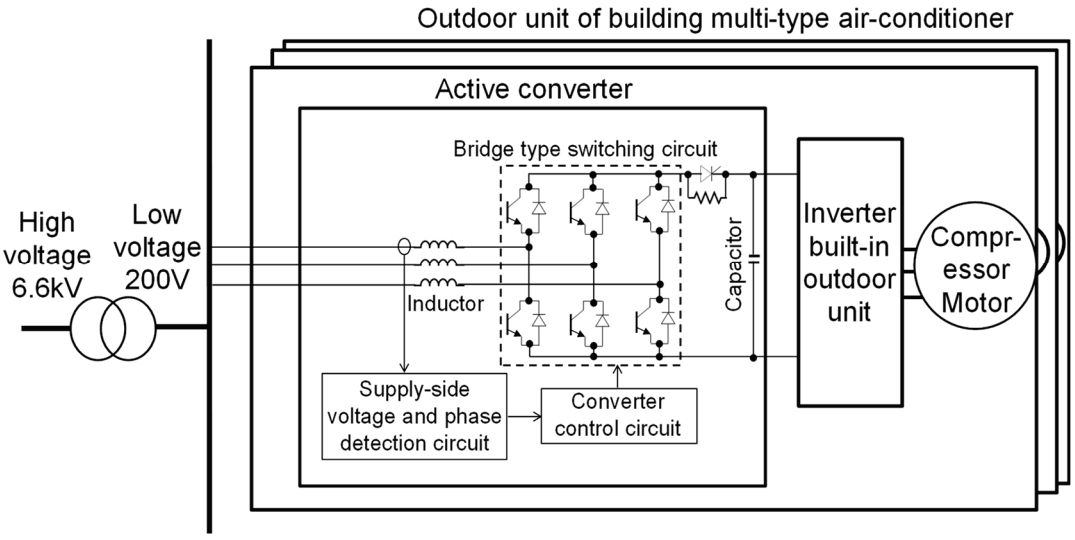

Fig. 3.1 Active converter of building multi-type air-conditioner

active converter, it is necessary to limit the operating range of the active power consumption of building multi-type air-conditioner during the reactive power control as shown in the next section.

3.1.2 Reactive Power Control of Active Converter

In principle, building multi-type air-conditioners can control power factor, as shown in Fig. 3.2, by coordinating the operation of the refrigerant compressor's inverter and the active converter. The injection/absorption of reactive power is corresponded to the lead/lag of power factor. To achieve the target reactive power $\hat{Q}_{AC}$ [kVar], the active converter transits in the operation modes shown in ① to ③ under the constraint of the power factor $\cos\theta_{max}$ (θ_{max} is the maximum operating power factor angle) and the rated apparent power capacity S_{max} [kVA].

$$P_0 = 0 \tag{3.1}$$

$$P_1 = \frac{\hat{Q}_{AC}}{\tan\theta_{max}} = \frac{\hat{Q}_{AC}}{\sqrt{\frac{1}{\cos^2\theta_{max}} - 1}} \tag{3.2}$$

$$P_2 = \sqrt{S_{max}^2 - \hat{Q}_{AC}^2} \tag{3.3}$$

$$P_3 = S_{max} \tag{3.4}$$

In the Fig. 3.2, the operating mode can be determined by operating points P_0, ..., P_3 of the active power consumption and the mathematical formulation of these operating points is shown Eqs. (3.1)-(3.4). The range of active and reactive power and the operation of the building multi-type air-conditioner in each operation mode are shown in Table 3.1.

Operation mode ① is called constant power factor and forced acceleration mode. While accelerating the active power P to the operating point P_1, the reactive power Q [kVar] is supplied under minimum operating power factor $\cos\theta_{max}$ limitation. When the active power reaches the operating point P_1, the reactive power injection reaches the target reactive power $\hat{Q}_{AC}$.

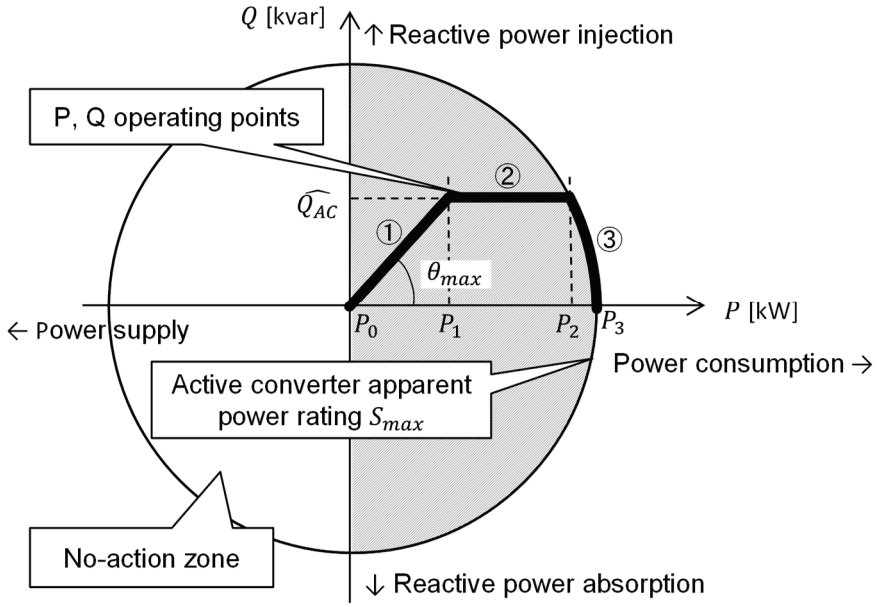

Fig. 3.2 Operating modes of VarDR

Table 3.1 Active and reactive power range of each operating mode

Operation mode	Active power range	Reactive power range	Operation of air-conditioner
①	$P_0 < P \leq P_1$	$Q \leq P \tan\theta_{max}$	Accelerate P to P_1
②	$P_1 < P \leq P_2$	$Q \leq \hat{Q}_{AC}$	Normal operation
③	$P_2 < P \leq P_3$	$Q \leq \sqrt{S_{max}^2 - P^2}$	Deaccelerate P to P_2

In operation mode ①, the building multi-type air-conditioner consumes more active power than required to maintain the room temperature, as a result, the room temperature decreases. This is because; to achieve the $\hat{Q}_{AC}$, outdoor unit operates at operating point P_1 forcedly. In this chapter, when the room temperature exceeds the set temperature +1 °C, it is assumed the impact on the occupants is excessive. Therefore, building multi-type air-conditioner should left out the VarDR event, also called "opt-out".

Operating mode ② is called free run mode. In operating range of this mode, the target reactive power $\hat{Q}_{AC}$ can be supplied at the minimum operating power factor $\cos\theta_{max}$ or higher for any of the active power P. Therefore, there is no restriction on the active power P consumed

by the building multi-type air-conditioner, and the air-conditioning control is same as normal operation.

The operation mode ③ is called power limit mode. When the active power P exceeds the operating point P_2, the target reactive power $\hat{Q}_{AC}$ cannot be supplied due to the capacity limit S_{max} of active converter. Therefore, deaccelerate the active power P to the operating point P_2, as the result, the target reactive power $\hat{Q}_{AC}$ can be supplied. However, limiting the active power leads to an increase in room temperature. In this chapter, when the temperature exceeds the set temperature +1 °C, the air-conditioner will be opt-out.

The response speed of reactive power also differs in each operating mode. For operating modes ②, response speed of reactive power is in seconds depending only on the response speed on the electronic circuit of active converter. However, in operating mode ① and ③, the response speed of the reactive power depends on the response speed of the active power. Since the active power of the building multi-type air-conditioner responds in minutes according to the change in compressor rotation speed, the response of the reactive power is also in minutes.

The response speed of reactive power in operation mode ① and operation mode ③ is in seconds up to the range of reactive power shown in Table 3.1, and thereafter it is in minutes depending on the response speed of active power. However, the active power of the building multi-type air-conditioner changes faster during deceleration than during acceleration, and in operation mode ①, the reactive power changes in proportion to the active power, whereas in operation mode ③, the reactive power rises along the right edge of the circle formed by the active converter rated apparent power shown in the Fig. 3.2. Therefore, the response speed of reactive power is faster in operation mode ③ than in operation mode ①.

3.1.3 Reactive Power Allocation Method for Cluster of Air-conditioners

In this subsection, the method of which a DERMS allocates the target reactive power to each building multi-type air-conditioner is described.

In future distribution system, the DERMS may be introduced and it would issue reactive power

control commands to each demand-side reactive power control entity. When the DERMS detects a voltage drop or a voltage rise in the distribution system, it calculates the total reactive power $\hat{Q}_{ADR}$ [kVar] to be commanded to a cluster of building multi-type air-conditioners. This chapter does not deal with the DERMS's issuing method of $\hat{Q}_{ADR}$, but, proposes how the $\hat{Q}_{ADR}$ is allocated to each building multi-type air-conditioner.

The simplest method is to divide the number of units proportionally by the Eq. (3.5).

$$\widehat{Q_{AC}^{b}} = \frac{1}{B}\hat{Q}_{ADR} \tag{3.5}$$

Here, B is the number of air-conditioners, and $\widehat{Q_{AC}^{b}}$ [kVar] is the reactive power command value of each air-conditioner. The superscript b in $\widehat{Q_{AC}^{b}}$ means the air-conditioner number ($b = 1, 2, \dots, B$).

Naturally, Eq. (3.5) does not take into account the air-conditioning load of each air-conditioner or the state of the air-conditioning and room air-conditioning comfort. A reactive power allocation method that takes these into account is necessary. In addition, in the method, it is desirable to use only variables that can be easily obtained from mass production models of building multi-type air-conditioners.

The reactive power allocation method that takes the above into account is defined as shown in the Eq. (3.6).

$$\widehat{Q_{AC}^{b}} = \frac{k_{CAP}^{b} + k_{TSA}^{b}}{\sum_{b=1}^{B}\left(k_{CAP}^{b} + k_{TSA}^{b}\right)}\hat{Q}_{ADR} \tag{3.6}$$

Here, k_{CAP}^{b} and k_{TSA}^{b} are proportional coefficients based on air-conditioning load and room air-conditioning comfort, respectively, and those variables are calculated by the following equations.

$$k_{CAP}^{b} = 1 - \alpha_1 \frac{P^{b}}{P_{max}^{b}} \tag{3.7}$$

$$k_{TSA}^{b} = \frac{1}{1 + \alpha_2 (T_{SA}^{b})^2} \tag{3.8}$$

Here α_1 and α_2 are parameters which are used to adjust the sensitivities between the load and comfort. The load is represented by the current power consumption of unit b, i.e., P^b. The comfort is the deviations of all indoor units of the unit b, i.e., T_{SA}^b.

$$T_{SA}^b = \frac{\sum_{i=1}^{I} C_{Pi}^b \left(T_{Ai}^b - T_{Si}^b\right)}{\sum_{i=1}^{I} C_{Pi}^b} \tag{3.9}$$

Here, C_{Pi}^b [kW] is the rated capacity, T_{Ai}^b [°C] is the measured room temperature, and T_{Si}^b [°C] is the set room temperature. The superscript b is the outdoor unit number and the subscript i is the indoor unit number $(i = 1,2, \ldots I)$, respectively. In other words, the average room temperature deviation T_{SA}^b is the value obtained by load averaging, the difference between the room temperature T_{Ai}^b and the set temperature T_{Si}^b of each indoor unit i in outdoor unit b by the rated cooling capacity C_{Pi}^b of the indoor unit, and is used as an index value representing the room temperature comfort of each outdoor unit.

In Eq. (3.8), the reason why T_{SA}^b is squared is to prevent excessive deviation from the room temperature and to reduce the proportional amount of reactive power in case of deviation from the set temperature, whether positive or negative. Since, both room temperature rise, and fall may occur when reactive power is supplied.

k_{CAP}^b approaches zero as the active power consumption increases, and k_{TSA}^b approaches zero as T_{SA}^b deviates in a positive or negative direction. In other words, less reactive power is allocated to building multi-type air-conditioners with high air-conditioning load and deteriorating air-conditioning comfort. Conversely, more reactive power is allocated to air-conditioners that are less air-conditioning load and have room for air-conditioning comfort.

The active power consumption P^b, the measured room temperature T_{Ai}^b, and the set room temperature T_{Si}^b required for the calculation of Eq. (3.6) are variables that can be transmitted to the Building Energy Management System (BEMS). When DERMS and BEMS are connected in the future, these variables will be easily available from DERMS.

It is assumed that Energy Resource Controller (ERC) is installed in each building. The ERC behaves front-end of the consumer energy resource from a viewpoint of DERMS, and it relays

the information between DERMS and the resources.

3.2 Air-conditioner Model

In this section, a mathematical model of building multi-type air-conditioner named Transient Air-conditioner Model (TAM) is defined to simulate the power and room temperature transient characteristics of a building multi-type air-conditioner [62]. See the Appendix A and Appendix B for further detail of developing the air-conditioner model. The TAM calculates the change in the active power consumption P [kW] of air-conditioner and room temperature T_A [°C] by the Eqs. (3.10)-(3.16). Here, T_A represents the ensemble average room temperature of all indoor units of one air-conditioner.

$$P(t+\Delta t) = P(t) + D(t)\Delta t \tag{3.10}$$

$$\begin{aligned} D(t) = S_{FR}^{P1} D_{UP} + (1 - S_{FR}^{P1})\{S_{OV}^{P2} D_{DWN} \\ +(1 - S_{OV}^{P2})[S_{OV}^{P1} S_{OV}^{\hat{P}} D_{DWN} \\ +\left(1 - S_{OV}^{\hat{P}}\right) S_{FR}^{P2} S_{FR}^{\hat{P}} D_{UP}]\} \end{aligned} \tag{3.11}$$

$$T_A(t+\Delta t) = T_A(t) + D_{TA}(t)\Delta t \tag{3.12}$$

$$D_{TA} = \frac{1}{C_H}\left(k_L Q_L(t) - Q_{AC}(t)\right) \tag{3.13}$$

$$Q_L(t) = Q_O(t) + Q_V(t) + Q_R + Q_I \tag{3.14}$$

$$Q_O(t) = k_O\left(T_{OET} - T_A(t)\right) \tag{3.15}$$

$$Q_V(t) = k_V\left(T_O - T_A(t)\right) \tag{3.16}$$

The explanations of each variable are shown in Table 3.2. In the Table 3.2, $\hat{P}$ [kW] is the power at which the room temperature change in Eq. (3.13) is exactly zero when the room temperature $T_A(t)$ reaches the set room temperature T_S. It is obtained by Eq. (3.17).

$$\hat{P} = \frac{Q_L{}'}{\eta_{COP}} \tag{3.17}$$

Table 3.2 Parameters of Transient Air-conditioner Model

Symbol	Description	Value
Δt	Simulation time interval	0.1 sec
D	Rate of change of active power	-
S_{OV}^{P1}	Excess state of active power P with respect to P_1	0 when $P \leq P_1$, 1 when $P > P_1$
S_{FR}^{P1}	Free run state of active power P with respect to P_1	1 when $P < P_1$, 0 when $P \geq P_1$
S_{OV}^{P2}	Excess state of active power P with respect to P_2	0 when $P \leq P_2$, 1 when $P > P_2$
S_{FR}^{P2}	Free run state of active power P with respect to P_2	1 when $P < P_2$, 0 when $P \geq P_2$
$S_{OV}^{\hat{P}}$	Excess state of active power P with respect to $\hat{P}$	0 when $P \leq \hat{P}$, 1 when $P > \hat{P}$
$S_{FR}^{\hat{P}}$	Free run state of active power P with respect to $\hat{P}$	1 when $P < \hat{P}$, 0 when $P \geq \hat{P}$
D_{UP}	Active power increase rate	0.025 kW/s (1.5 kW/min)
D_{DWN}	Active power decrease rate	-0.083 kW/s (5.0 kW/min)
C_H	Sum of heat capacities of walls, fixture, and air	6000 kJ/°C
Q_O	Thermal load from outer walls	1.1 kW (At set temperature)
Q_V	Ventilation load	9.7 kW (At set temperature)
Q_R	Solar radiation load	9.0 kW
Q_I	Internal heat generation load	14.0 kW
Q_L	Total heat load	33.8 kW (At set temperature)
k_O	Thermal transmission rate	0.12 kW/°C
k_V	Ventilation load factor	0.51 kW/°C
k_L	Heat load multiplier	-
T_{OET}	Outside temperature considering overheating of outer walls	45 ℃
T_O	Outside temperature	35 ℃
T_S	Set temperature	26 ℃
η_{COP}	Coefficient Of Performance: COP	3.0
P_{max}	Rated power consumption	20 kW
P_{min}	Minimum power consumption	2 kW
S_{max}	Active converter apparent power rating	20 kVA

Here, Q_L' [kW] is the balance point heat load, which is obtained by adding each heat load in the same way as in Eq. (3.14), with $T_A(t)$ same as the set room temperature T_S in the case of the thermal load from outer wall Q_O in Eq. (3.15) and the ventilation load Q_V in Eq. (3.16). The model can treat different heat loads by changing the heat load multiplier k_L in Eq.(3.13).

In actual building multi-type air-conditioners, the rate of change of active power $P(t)$ is not

determined only by the heat balance power $\hat{P}$. The rate of change of the active power is caused as a result of the embedded control refereeing the internal state of the refrigerant circuit and controlling the compressor speed of the outdoor unit. In addition, since each indoor unit originally controls the refrigerant flow rate into the heat exchanger independently, the internal state of the refrigerant circuit fluctuates in an extremely complicated manner. Therefore, the transient behavior is modeled in order to emulate second or minute order change of active power consumption of the building multi-type air-conditioners. In this research, dimensions and specifications of all rooms of buildings are assumed identical.

3.3 Simulation Conditions

3.3.1 Distribution System Model

In order to confirm the effect of VarDR, a power distribution system model was defined as shown in Fig. 3.3. The distribution system model is based on the urban area pattern C2 model [63] from

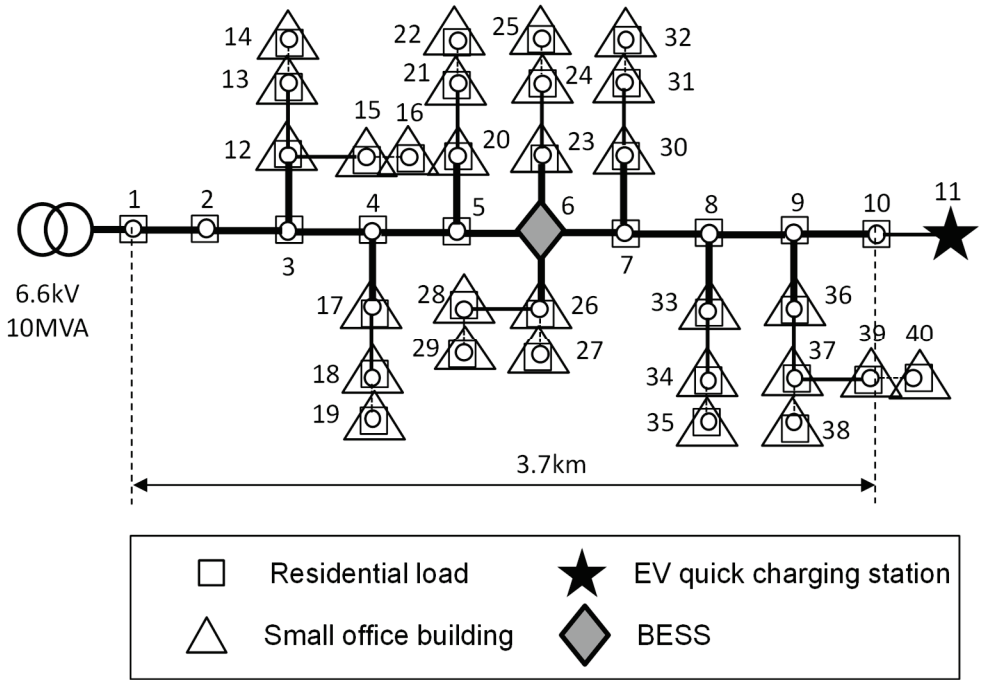

Fig. 3.3 Power distribution system model

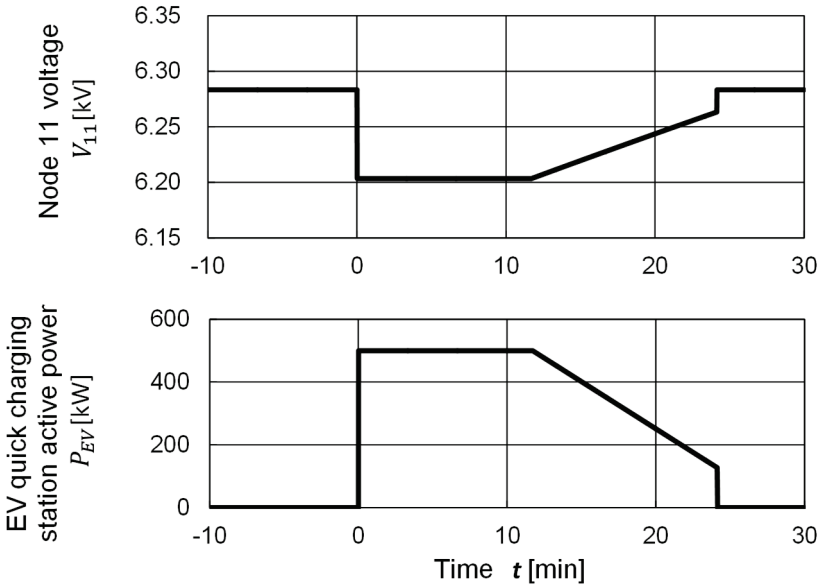

Fig. 3.4 Quick EV charging model and its node voltage

Table 3.3 List of loads in distribution system model

Load type	**Load per node**	**Number of nodes**	**Total load**
Residential	$15\ \text{kW} + j3\ \text{kVar}$ (Total of 15 houses)	38	0.57 MW
Office building	$100\ \text{kW} + j10\ \text{kVar}$ (per building)	29	2.90 MW
Quick EV station	$500\ \text{kW}$ (total peak of simultaneous charge)	1	0.50 MW
BESS	$0\ \text{kW}$ (standby mode)	1	0.00 MW
-	-	Total	3.97 MW

Electric Technology Research Association research group and some load facilities is added to the model. The list of the load facilities is shown in Table 3.3.

This simulation assumes a scenario in which the voltage drop caused by the large power consumption of the EV quick charging station installed at Node 11 at the end of the trunk line. Also, the deviation is restored to the level before the voltage drop by the DERMS using reactive power control with DERs in the distribution system.

In the distribution system model shown in the Fig. 3.3, one small office building (two-story

building with a total floor area of about $1500\ \mathrm{m}^2$) is connected at each node of each branch line and widely distributed so that the building multi-type air-conditioner's cluster can be consolidated at any node in the distribution system. Each building was assumed to have five building multi-type air-conditioners.

The building multi-type air-conditioners consume about 10 kW, which is 50% of their rated power consumption, under the heat load conditions shown in the Table 3.2. Therefore, the air-conditioning power consumption is 50 kW at each office building, and if the other general electric load is assumed $50\ \mathrm{kW} + j10$ kVar, the total power consumption per building will be $100\ \mathrm{kW} + j10$ kVar.

All low-voltage loads are assumed to be residential, with $1.0\ \mathrm{kW} + j0.2$ kVar per house connected to 15 houses per node. It is assumed that most of the residents are in the house during the daytime and the load is high according to the summer days.

As shown in Fig. 3.4, the power consumption of the EV quick charging station P_{EV} [kW] is simulated by the Constant Current Constant Voltage (CC-CV) method. Here, the future quick charger is assumed, 5 EV charger of 100 kW start the charging at the same time. The total maximum power consumption is 100 kW. The voltage of Node 11, V_{11} [kV], drops from 6.28 kV to 6.20 kV when the EV charging station start charging as shown in the Fig. 3.4. Normally, the EV quick charging station itself has a phase regulator, but for the purpose of confirming the effect of VarDR, it is assumed that reactive power control is not possible to maintain the own-end voltage.

The Battery Energy Storage System (BESS) participating in reactive power control is installed at Node 6 in the middle of the trunk line, with no active or reactive power injection when the BESS is in standby. This simulation assumes that the BESS can supply the exact reactive power requested by DERMS. To compare the VarDR and the BESS, it is assumed that the DERMS chooses either the VarDR or the BESS as reactive power source.

For simulation, OpenDSS [64] of EPRI was used as the circuit analysis solver for the distribution system model. The dynamic models of the building multi-type air-conditioners and

the EV quick charging station were created in Matlab [65] and linked with the OpenDSS. The simulation time step was set to 0.1 second.

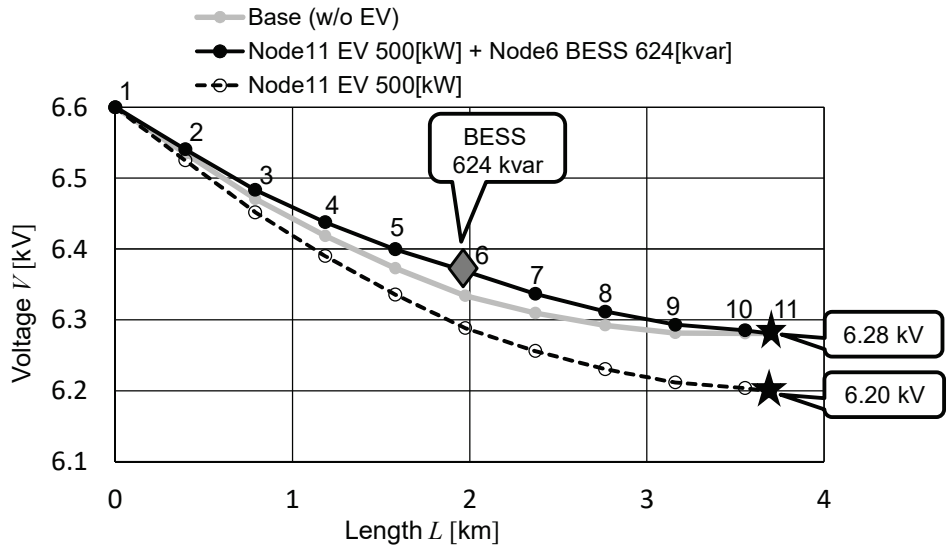

(a) Voltage recovery with a distant BESS

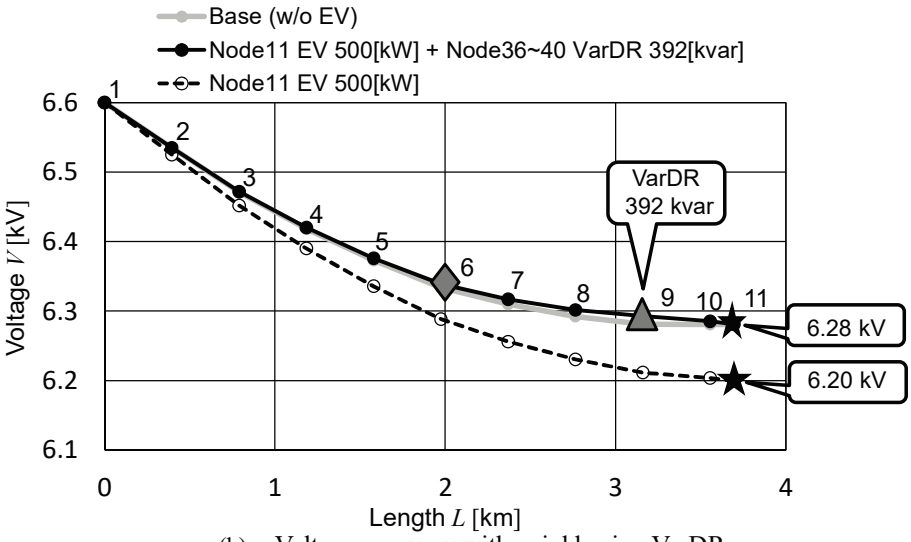

(b) Voltage recovery with neighboring VarDR

Fig. 4.5 Change of voltage profile of distribution system

3.3.2 Simulation Conditions of VarDR

During the VarDR using a cluster of building multi-type air-conditioners, 5 nodes from Node 36 to Node 40 (25 building multi-type air-conditioners in total) were participated.

It is assumed that the DERMS calculates the total amount of reactive power required to recover the voltage drop of Node 11 every moment, and to give reactive power commands to each building multi-type air-conditioner. And DERMS sends reactive power commands to each building multi-type air-conditioner at one-minute intervals because: a) the time required for the DERMS to detect a voltage drop in the distribution system, b) the time required to determine the multi-building air-conditioners to be controlled by VarDR and their sizes, c) the time required for the DERMS to send the commands to the Energy Resource Controller (ERC), and d) the communication delay between DERMS-ERC-BEMS and building multi-type air-conditioners.

The simulations were performed of the following two cases which are different heat loads and different allocation methods to assign the reactive power command to each air-conditioner.

Case1: When the heat load of the building multi-type air-conditioners is different ($k_L =$ 0.5～1.5) and the reactive power command is equally distributed according to Eq. (3.5).

Case2: When the heat load of building multi-type air-conditioners is different ($k_L =$ 0.5～1.5) and the reactive power is distributed by the reactive power allocation method according to Eq. (3.6).

The heat load multiplier k_L is set to k_L =0.5 for air-conditioners at Node 36 and Node 37, k_L =1.0 for air-conditioners at Node 38, and k_L =1.5 for air-conditioners at Node 39 and Node 40. The parameters of the reactive power allocation method defined in Eq. (3.6) are assumed as $\alpha_1 = 1.0$ and $\alpha_2 = 0.5$, respectively. The minimum operating power factor of the active converter $\cos\theta_{max}$ is set to 0.4.

3.4 Simulation Results

3.4.1 Voltage Profile

Fig. 3.5 shows the changes in the voltage profiles of the trunk line (Node 1 to Node 11) of the distribution system. Fig. 3.5 (a) shows the case of the BESS reactive power injection at Node 6, and Fig. 3.5 (b) shows the case of VarDR from Node 36 to Node 40. It is assumed that the voltage should be kept within 5% of nominal voltage.

When the quick EV station starts charging, the voltage at Node 11 drops from 6.28 kV to 6.20 kV. The amount of reactive power required to restore the voltage at Node 11 was 624 kVar at Node 6, and a total of 392 kVar at branch node, Node 9. The voltage recovery was achieved by injecting less reactive power in case of VarDR than that of BESS, because it could be done at a point closer to the problem node, Node 11.

3.4.2 Time Varying Operation of VarDR

Fig. 3.6 and Fig. 3.7 show the voltage at Node 11, V_{11} [kV], and EV quick charging station active power P_{EV} [kW] for Case1 and Case2, respectively.

The DERMS gave a target value of total reactive power $\hat{Q}_{ADR} = 400$ kVar at maximum for cluster of building multi-type air-conditioners. The EV quick charging station starts charging at $t = 0$ and the voltage at Node 11 drops to 6.20 kV shown in the Fig. 3.8. After that, at $t = 1$ minute, the building multi-type air-conditioners start VarDR, and the voltage at Node 11 recovers to 6.28 kV as the voltage before the EV charging starts. From $t = 12$ minutes and onwards, the target reactive power is gradually decreased by the DERMS every minute as the power consumption of the EV quick charger decreases.

In Case1 shown in the Fig. 3.8, immediately after the start of VarDR, the voltage at Node 11 recovers to the level as before the start of EV charging. The air-conditioners of buildings with high heat loads, at Node 39 and Node 40, are operate in operation mode ③, and the room temperature rises with the passage of time because the active power is reduced to inject the target

reactive power into the system.

On the other hand, the air-conditioners of buildings at Node 36 and Node 37 with low heat loads are operate in operation mode ①, and they consume more active power than necessary for room temperature control to inject the reactive power into the system. Therefore, the room temperature might decrease below the set temperature. The air-conditioners of building at Node 38 operate at similar heat load as in the Case1.

At $t = 14$ minutes, the air-conditioners of buildings with high heat loads at Node 39 and Node 40 reach $T_{SAA} = +1$ ℃ and withdrawal from the VarDR event occur, so-called "opt-out". As a result, the total supplied reactive power cannot maintain the target value and the voltage at Node 11 only recovered from 6.20 kV to 6.24 kV.

In the Case2, shown in the Fig. 3.9, room temperature rises and falls as in the Case1, but no opt-out occurred, as a result, the voltage at Node 11 is maintained at the same level as in the Case1. Because the reactive power command is distributed to each outdoor unit as the reactive power allocation method taking into account the air-conditioning load and room air-conditioning comfort of each building multi-type air-conditioner as Eq. (3.6) stated.

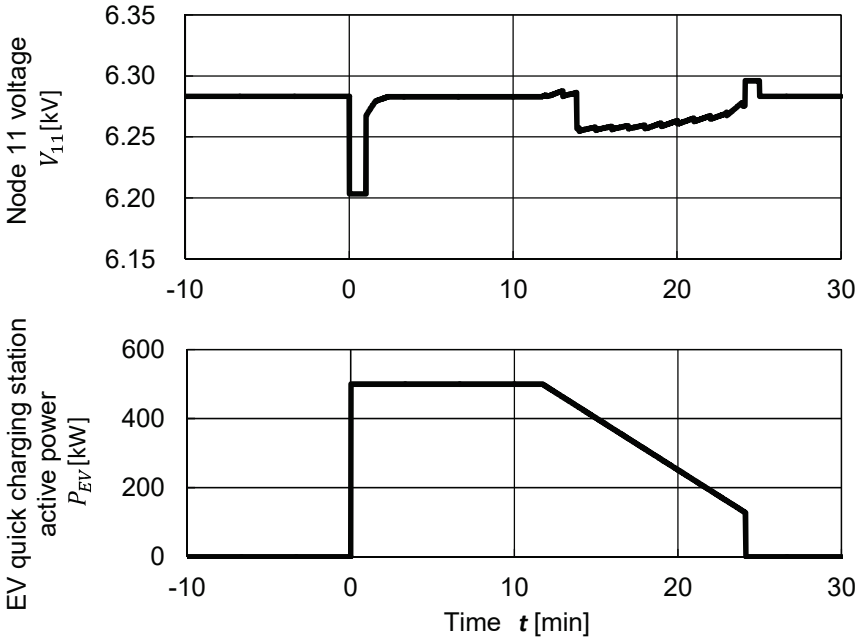

Fig. 3.6 Node 11 voltage, EV charger active power, Case1

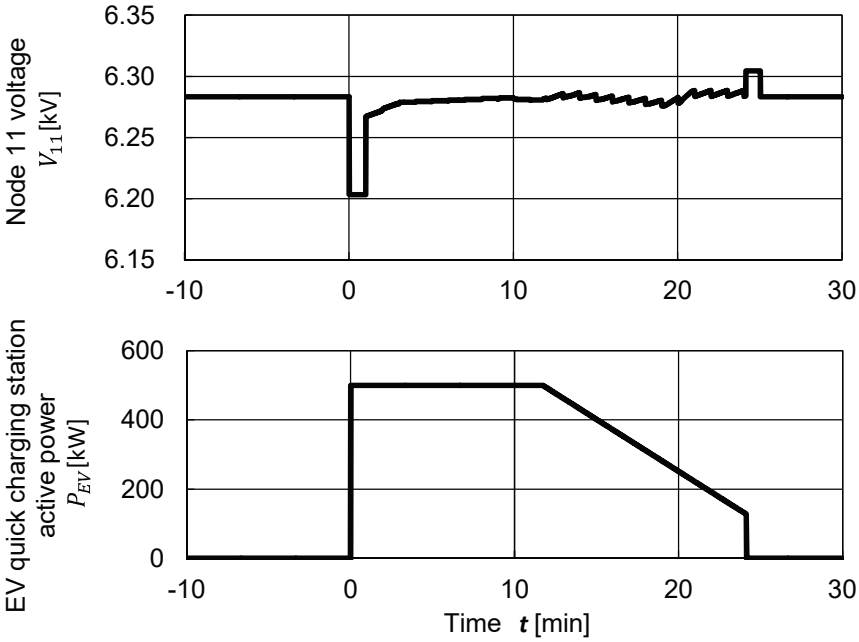

Fig. 3.7 Node 11 voltage, EV charger active power, Case2

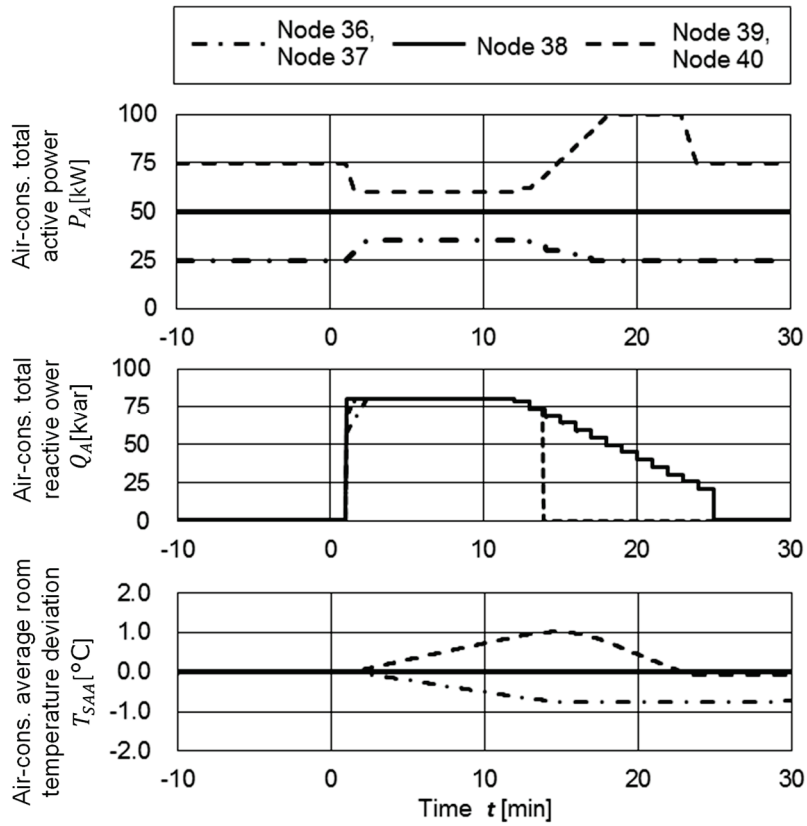

(a) Active power, reactive power, average room temperature deviation of each building

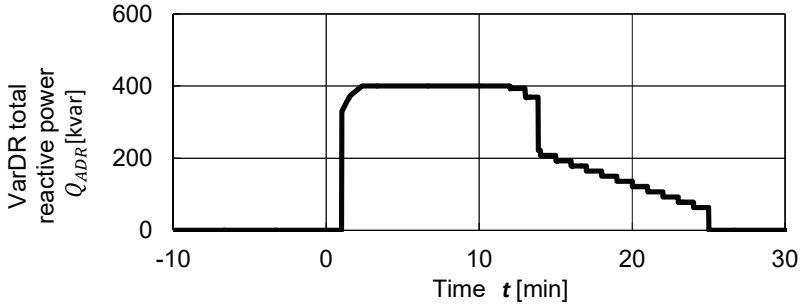

(b) VarDR total reactive power

Fig. 3.8 Simulation result of VarDR,
Case1: reactive power allocated by fixed method

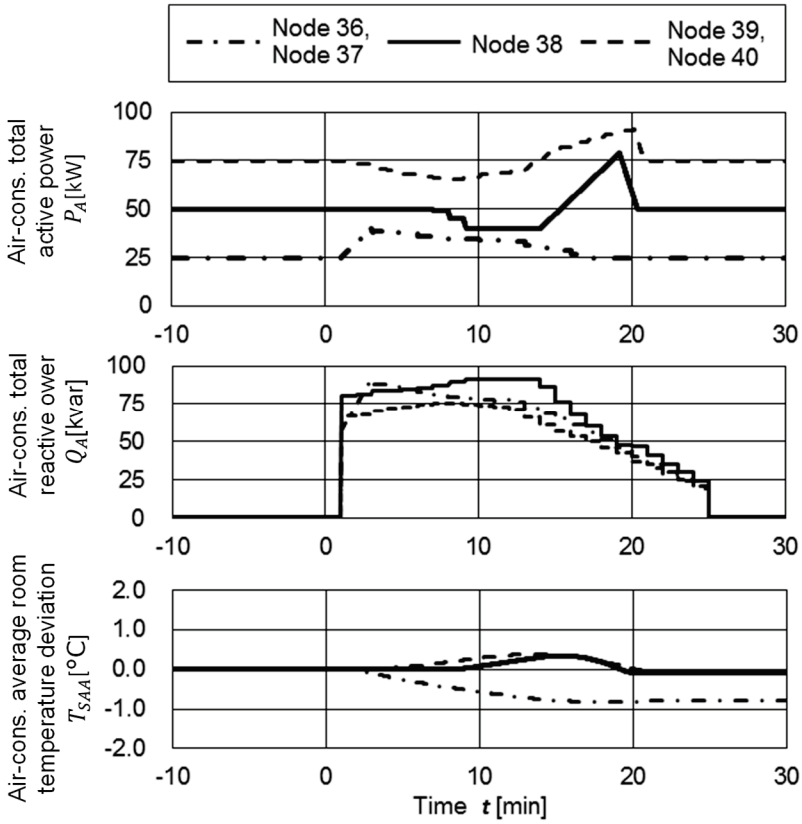

(a) Active power, reactive power, average room temperature deviation of each building

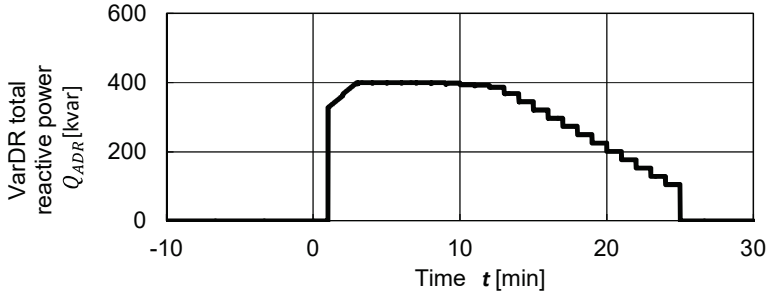

(b) VarDR total reactive power

Fig.3.9 Simulation result of VarDR,
Case2: reactive power allocated by allocation algorithm

3．5 Discussion on Interesting Facts

As shown in the Fig. 3.5, by performing VarDR using a cluster of building multi-type air-conditioners from Node 36 to Node 40, i.e., closest to problematic Node 11, the required reactive power was less than that of BESS at Node 6 away from the problem node.

As shown in Fig. 3.8, when a building multi-type air-conditioner is operating at 50% of the rated power consumption (i.e., when air-conditioning load is 50% of the rated cooling capacity), the maximum utilization of reactive power Q_{max} is as Eq. (3.18).

$$Q_{max} = \sqrt{S_{max}^2 - (0.5P_{max})^2} \approx 0.86S_{max} \tag{3.18}$$

This means that it is possible to inject/absorb the reactive power up to about 50% ($Q_{max} =$ 17.3 kVar) of the rated capacity of active converter without affecting the active power for air-conditioning.

In Case1, the air-conditioners of buildings at the Node 39 and Node 40 with high heat loads opted-out the VarDR operation due to the rise in room temperature. The simple evenly allocation of reactive power shown in Eq. (3.5) causes opt-out as described above as the air-conditioning comfort deteriorates, and the target reactive power might be not achieved even in a short period VarDR about 10 minutes.

In the Case2, the reactive power allocation method based on Eq. (3.6), which takes into account the air-conditioning load and the room air-conditioning comfort, is used to allocate more reactive power to air-conditions of the buildings with a room temperature margin, i.e., at Node 38, and allocate the low amount of reactive power to air-conditioners of the buildings where room temperature is deviating from set temperature, i.e., at Node 36, Node 37, Node 39, and Node 40. As a result, all the building multi-type air-conditioners could keep the VarDR event.

As shown in the Case2, the local voltage drop caused by EV quick charging station can be recovered by the VarDR of air-conditioners about 5 small office buildings for a time period about 10 minutes by using the reactive power allocation method of Eq. (3.6).

Chapter 4　System Design of DERMS Volt-Var Control

This chapter describes the system design of DERMS Volt-Var control with VarDR of building multi-type air-conditioner. First, the interaction between DERMS building multi-type air-conditioners is explained. Then, a method for the entire system described. Finally, for confirmation of DERMS Volt-Var control with VarDR of building multi-type air-conditioner, the simulation results are described with some assumptions of simulation conditions.

4．1 DERMS Volt-Var Control Using Air-conditioners

4．1．1 DERMS with Building Multi-type Air-conditioners

Figure 4.1 shows a conceptual diagram of the DERMS Volt-Var droop curve control system with VarDR for a building multi-type air-conditioners cluster.

DERMS is a system that centrally controls and manages the voltage in a distribution system where a large number of distributed energy resources are installed. The Volt-Var droop curve control is one of the core functions of a DERMS. It is a centralized voltage control method that injects and absorbs the reactive power from consumer equipment based on the target reactive power of the droop curve, which has the measured voltage on the horizontal axis and the reactive power on the vertical axis. In past, DERMS Volt-Var droop curve control was assumed to be used with reactive power controllable power conditioners (so-called smart inverters) in PV systems and BESSs.

However, these PV systems and BESSs are generally deployed at a fixed location and are unable to cope with situations where the problem locations move in the distribution system. In

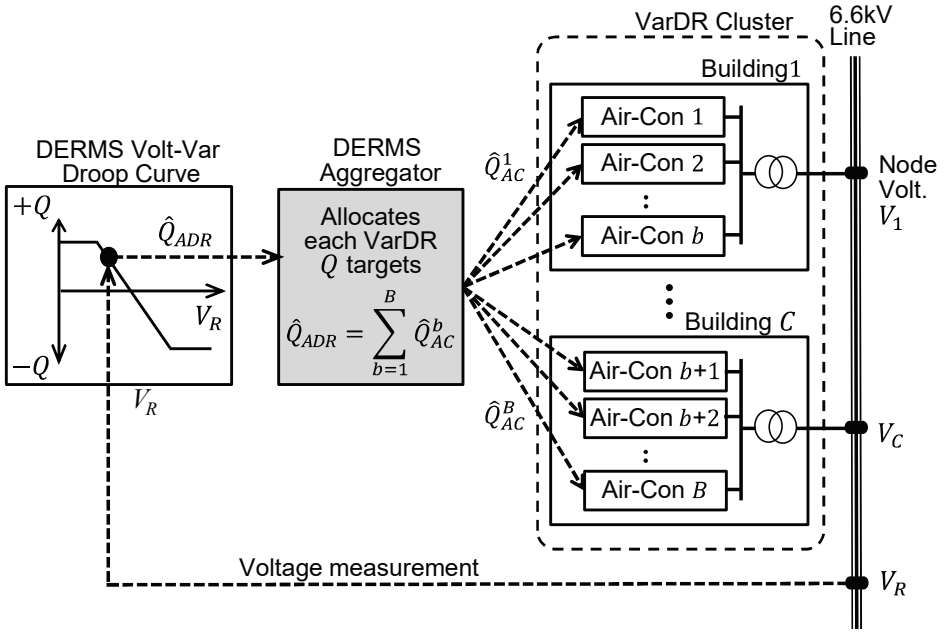

Fig. 4.1 DERMS Volt-Var droop curve control system with VarDR of building multi-type air-conditioner clusters

contrast, building air-conditioning systems are widely spread in urban areas. If reactive power control from these systems is possible, they can help to solve the problem of distribution system voltage deviations, particularly when the problem locations move over the time. In this case, it is necessary to study the design method for the DERMS Volt-Var droop curve control system with VarDR clusters.

4.1.2 Inject/Absorb Reactive Power with Active Converter

Figure 4.2 shows (recall Fig. 2.6) of reactive power injection/absorption and constraints on active power to a compressor, and the impact on air-conditioning performance (i.e., deviations in room temperature). As shown in Fig. 4.2, normally, the air-conditioner is operated at a power factor of unity. Thus, air-conditioning active power is not curtailed. However, when a reactive power inject/absorb command is received, as in the case of VarDR, the air-conditioning active power is

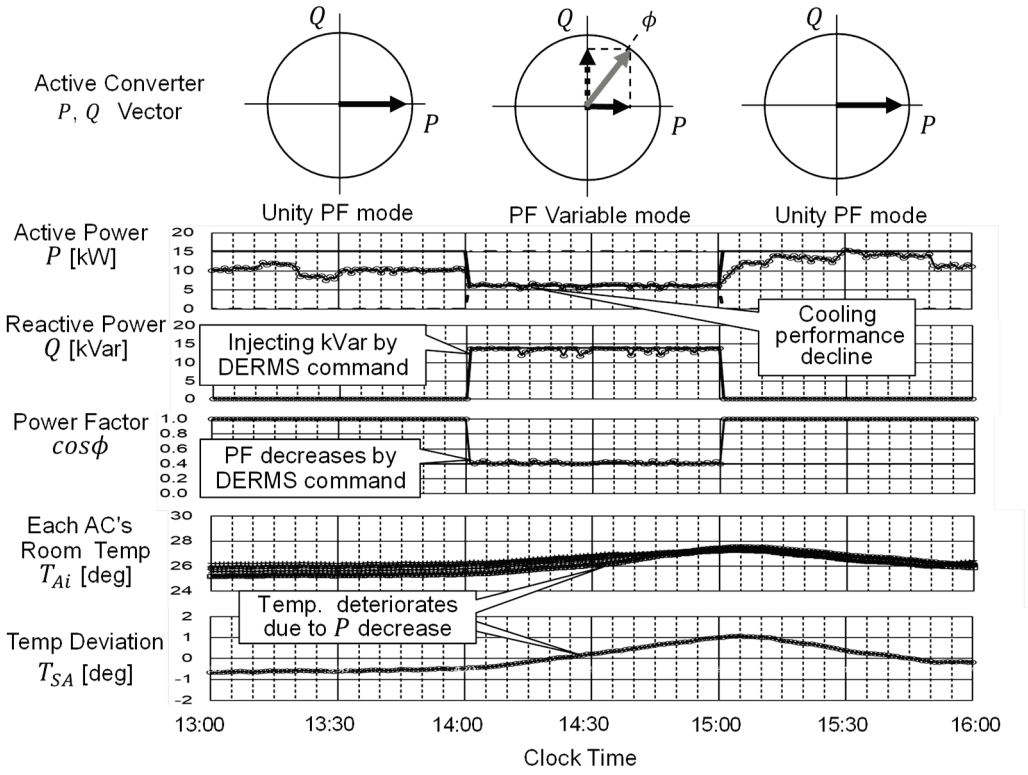

Fig. 4.2 Relationship between active/reactive power, power factor, and room temperature for an air-conditioner (recall Fig. 2.6)

curtailed depending on the control strategy. As a result, the air-conditioning capacity decreases and the room temperature rises.

Recall the challenges, the challenge of implementation of the DERMS with VarDR is as follows. First, the cluster intrinsically uses many air-conditioners, and to keep costs low, all air-conditioners are assumed to be off-the-shelf products. Second, the aggregator of the cluster must execute all DERMS functions. The aggregator is assumed to not measure the voltage of each building for droop curve control. Therefore, the aggregator uses one reference voltage value to all air-conditioners in the cluster. This usage of DERMS droop curve control is not simple and a new method is proposed to cope with these specific constraints.

4.2 Volt-Var Droop Curve Control with Building Multi-type Air-conditioners

4.2.1 Volt-Var Droop Curve with VarDR

To implement DERMS Volt-Var droop curve control with VarDR for a building multi-type air-conditioner cluster, the target reactive power $\hat{Q}_{ADR}$ must be allocated to each air-conditioner in each building at each control cycle. Because $\hat{Q}_{ADR}$ is based on the Volt-Var droop curve parameters, this is the key point to configure the DERMS Volt-Var droop curve control with VarDR.

Furthermore, the DERMS aggregator needs to allocate the total reactive power command value $\hat{Q}_{ADR}$ for the entire VarDR cluster proportionally, without having a perceptible effect on the cooling function of air-conditioners in each building. In other words, when computing the proportional allocation of $\hat{Q}_{ADR}$, each air-conditioner's load status and room temperature comfort level must be taken into account.

In general, the Volt-Var droop curve is intended to be a method in which each individual DER obtains target reactive power by its own point of connection voltage. However, for a building multi-type air-conditioning VarDR cluster, the status of each air-conditioner also plays a significant role. Simply allocating the target reactive power from the droop curve equally could

reduce room comfort levels. Therefore, in this research, the Volt-Var droop curve was thus attempted to be applied to a group of air-conditioners as a cluster by making them the target of a single droop curve control and proportionally allocating the target reactive power to individual air-conditioners according to their load status.

4.2.2 Allocation of Reactive Power Command to Each Air-conditioner

Chapter 3 described a reactive power command value allocation algorithm that takes into account the cooling load of each air-conditioner in the cluster. In this research this algorithm is used to allocate the reactive power command value $\hat{Q}_{AC}^{b}$ to each air-conditioner in the cluster based on target reactive power $\hat{Q}_{ADR}$ obtained from the DERMS Volt-Var droop curve. The DERMS aggregator in Fig. 4.1 calculates $\hat{Q}_{AC}^{b}$ for each air-conditioner according to Eq. (4.1)

$$\hat{Q}_{AC}^{b} = \frac{k_{CAP}^{b}+k_{TSA}^{b}}{\sum_{b=1}^{B}(k_{CAP}^{b}+k_{TSA}^{b})}\hat{Q}_{ADR}, \tag{4.1}$$

Where b is the air-conditioner number (b=1, 2, …, B), B is the number of air-conditioners in all buildings in the cluster, k_{CAP}^{b} is the proportional coefficient based on the air-conditioning load, and k_{TSA}^{b} is the proportional coefficient for room air-conditioning comfort. k_{CAP}^{b} and k_{TSA}^{b} are calculated by Eqs. (4.2) and (4.3), respectively.

$$k_{CAP}^{b} = 1 - \alpha_1 \frac{P^b}{P_{max}^{b}}, \tag{4.2}$$

$$k_{TSA}^{b} = \frac{1}{1+\alpha_2 (T_{SA}^{b})^2}, \tag{4.3}$$

Where P^b [kW] is the consumed active power of outdoor unit b; P_{max}^{b} [kW] is the rated active power of outdoor unit b; α_1 and α_2 are parameters to adjust the sensitivity of P^b and T_{SA}^{b}, respectively; and T_{SA}^{b} is the average room temperature deviation [°C] of multiple indoor units belonging to air-conditioner b. In a building multi-type air-conditioner, multiple indoor units belong to one outdoor unit block, each of which has its own room temperature measurement and set temperature. The room temperature change values are averaged by the size of the indoor units to express the comfort level produced by each outdoor unit.

In Chapter 3, the target reactive power is set to a certain value. Here, the target reactive power is dynamically determined using DERMS control method. Figure 4.3 shows a high-level flowchart of the method for the entire system. When the method is activated, the procedure in the flowchart is executed as a digital system control.

Before the activation, the electric company makes VarDR participation contracts with many candidate buildings. When a voltage distribution problem at some node(s) is expected to occur, the DERMS center selects one or more VarDR aggregators having a cluster as near as possible to the problem node. The DERMS center dispatches a common Volt-Var droop curve, whose parameters the center has defined as appropriate beforehand, to the selected aggregators.

Each reference voltage value for the droop curve is measured at a representative node defined on the trunk line by the DERMS center, instead of each building's connecting node.

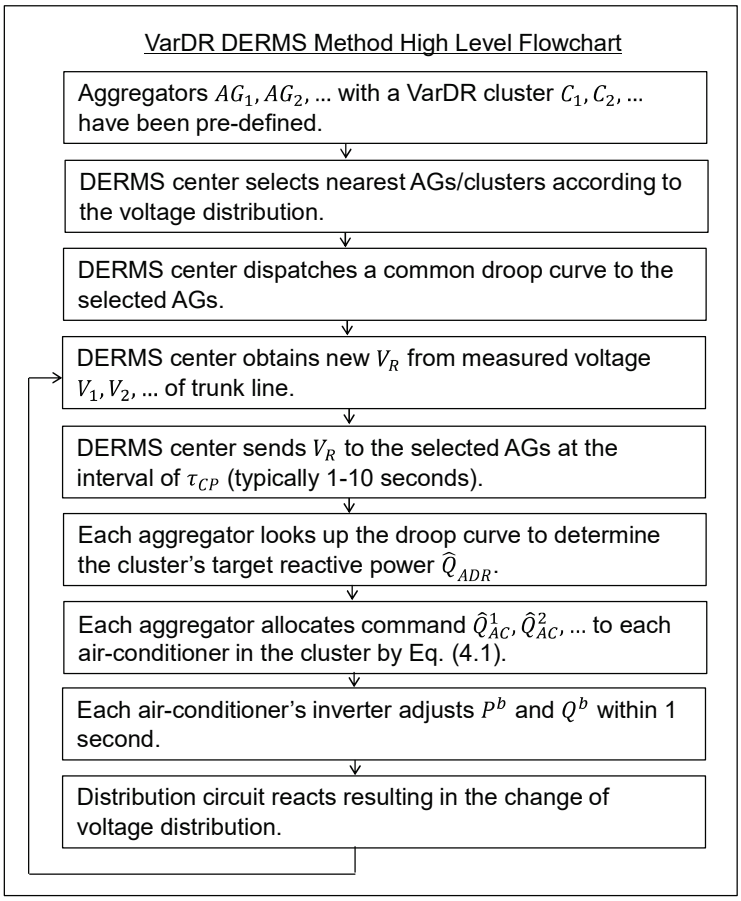

Fig. 4.3 VarDR DERMS method

The discrete control period τ_{CP} is set to 1~10 seconds to respond to the fast transient behavior of BESSs. The wide-area communication among the center/aggregator/building is assumed to be OpenADR/DER [66] with XMPP [67], which is a fast bi-direction lower layer protocol. The target reactive power $\hat{Q}_{ADR}$ divided into each reactive power command value $\hat{Q}_{AC}^{1}, \hat{Q}_{AC}^{2}, \ldots, \hat{Q}_{AC}^{B}$ by using Eqs. (4.1)-(4.3).

Consequently, by using the reference voltage V_R at trunk line and a common droop curve, each air-conditioner need not deal with each droop curve, which makes it possible to use off-the-shelf air-conditioners.

Thus, a method is developed to apply a DERMS Volt-Var droop curve control system for building multi-type air-conditioner VarDR clusters, as shown in Fig. 4.3.

4.3 DERMS Real-time Simulator

4.3.1 Composition of DERMS Real-time Simulator

A DERMS real-time simulator, shown in Fig. 4.4, was developed to confirm the effectiveness of VarDR with building multi-type air-conditioners and to identify the essential concerns. In this simulator, it is assumed that a monitoring and control center (called the DERMS center) exists within an electric power company's distribution system operator (DSO), and that the DERMS center monitors and controls a certain area with multiple distribution system feeders. The DERMS real-time simulator simulates one of the distribution system feeders.

The distribution system feeder model is based on the urban area pattern C2 model [63] of the Electric Technology Research Association research group with some additional load facilities as shown in Fig. 4.5. This distribution system feeder has 40 high voltage nodes (6.6 kV), from which low voltage consumers are supplied, but the simulator focuses only on the high voltage nodes. The DERs targeted by the simulator are limited to those connected to the 6.6 kV high voltage feeder.

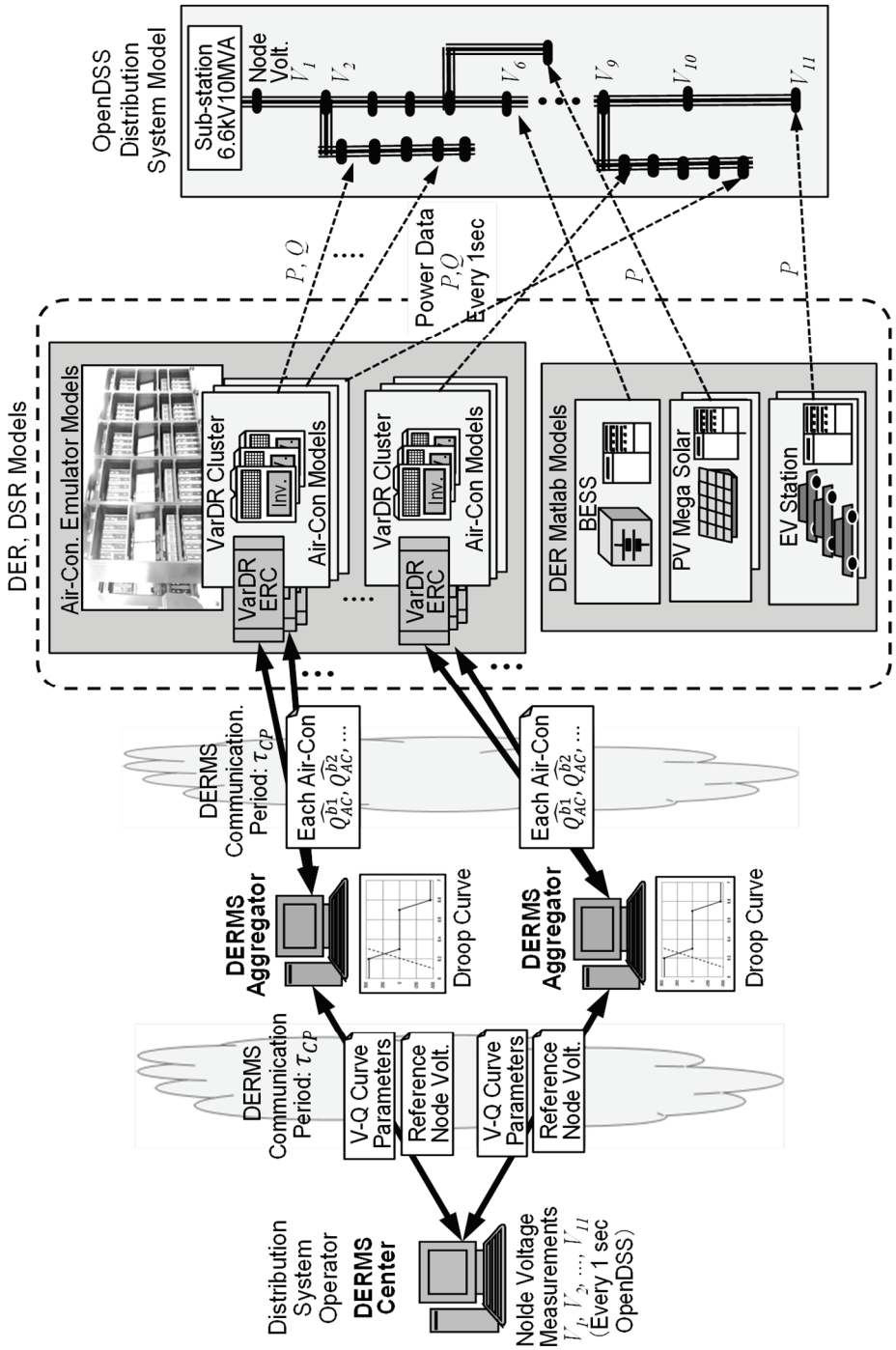

Fig. 4.4 Configuration diagram of DERMS real-time simulator

Multiple DERMS aggregators, or service providers, are assumed to intervene in parallel between the DERMS center and each customer DER to perform functions such as aggregation, allocation, monitoring, and control. The DERMS aggregators are assumed to be specialized in handling the specific monitoring and control depending on the type of target DER or VarDR cluster. In addition, these DERMS aggregators merely exchange information and are not directly involved in the electric circuits of the distribution system. Therefore, they do not necessarily need to be located in the feeder district of concern, but are assumed to be serving a wide area in some city or country.

DER devices that are connected to the high voltage grid are monitored and controlled through DERMS communication via the DERMS aggregator. In this case, the customer side is assumed to be equipped with a communication controller, called the Energy Resource Controller (ERC), that has DERMS communication and DER monitoring and control functions.

4.3.2 Operation of DERMS Real-time Simulator

In Fig. 4.4, the DERMS center monitors the distribution system's node voltages and provides the Volt-Var droop curve parameters to each individual DERMS aggregator every second. It is

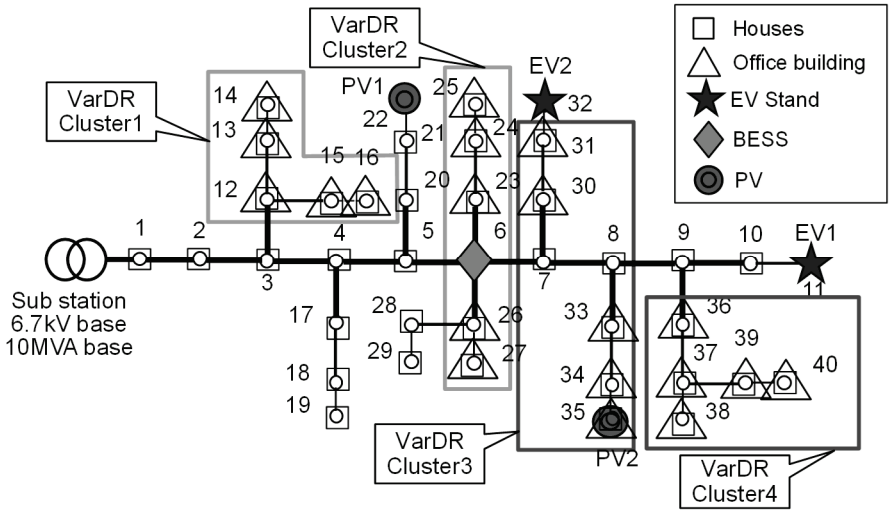

Fig. 4.5 Simulation model of the power distribution network

assumed that each building equipped with ERC, which reports the active power consumption of each air-conditioner and average room temperature deviation to the DERMS aggregator every 10 seconds. The DERMS aggregator forms the VarDR cluster and performs proportional allocation of the reactive power command value $\hat{Q}_{AC}^{b}$ to each air-conditioner in the cluster by Eq. (4.1) using the information for each air-conditioner reported by the ERCs.

For communication, OpenADR/DER/XMPP, the DERMS standard communication protocol, was used between the DERMS center and DERMS aggregator and between the DERMS aggregator and ERCs. The circuit analysis solver for the distribution system model was OpenDSS from EPRI, USA.

A simulator is made, Fig. 4.4, using a real-time function call in OpenDSS from Matlab/Simulink. All the parts of our simulator are made from digital models, i.e., virtual components. But, the entire simulation system behaves in real time as if actual system consisting of many devices are operating.

4.4 Simulation Conditions

4.4.1 Simulation Scenario Modeling

A 30-minute scenario model was created for a fictitious distribution system with combined simultaneous operation of large DERs. As shown in Fig. 4.5, two super-fast-charging EV stands (600 kW class), two large PV power plants (1.2 MW class), and one large BESS (1 MW class) were placed at various locations in the distribution system feeder. It is assumes that this is a possible load configuration in a near-future distribution system, considering examples in recent reports [68] and [69].

The EV stands were assumed to be future super-fast-charging EV stands, with three 200 kW chargers installed in one stand, which start charging every 2 minutes. Each charger takes 10 seconds to reach its maximum power, and maintains the maximum power for 5 minutes. The model is approximated by an exponential decrease in the power supply voltage, simulating the

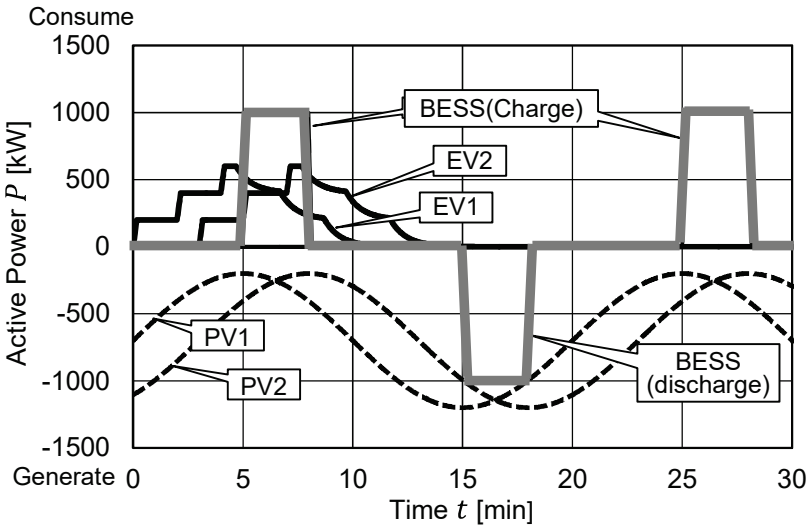

Fig. 4.6 Simulation scenario of active power change for each DER

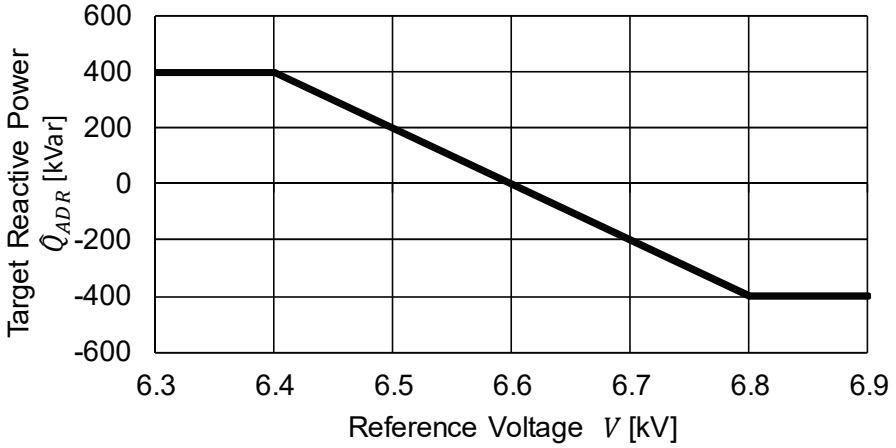

Fig. 4.7 Droop curve used in the DERMS simulation

constant current constant voltage method. In general, it is conceivable that the EV stand itself could have a cooperative function with the distribution system voltage control in grid interconnections. However, in this simulation, it is assumed that reactive power control to manage the end voltage at the EV connection point is not performed to confirm the effect of VarDR.

The PV system was modeled as a sinusoidal solar radiation intensity increase/decrease curve with a period of 20 minutes, modeling the movement of clouds, and the time difference between PV1 and PV2 at each location was assumed to have a phase difference of 3 minutes, resulting in

output fluctuations.

The BESS was considered to participate in the supply/demand coordination market and to charge/discharge independently of the state of the distribution system. The BESS was assumed to take 10 seconds to reach its maximum power of 1 MW (called “rise time”) and then charge or discharge at constant power for the next 3 minutes. In this typical scenario, the BESS rise time was chosen by keeping in mind the future power grid. In [58], a demonstration project for DERMS is presented with a BESS that can swing 8 MW power in 4 seconds. Presently, it is not necessarily that the utility scale BESSs have such fast rise time. However, in future 10 years from now, the cutting-edge battery technology might approach the rise time in seconds order. One a example is published in [78] where the medium scale battery (hundreds kW scale) approach the maximum rating in seconds order.

These DERs were combined to create a scenario in which the active power varies with time, as shown in Fig. 4.5. At $t = 5\sim8$ minutes in Fig. 4.6, the maximum EV charge, PV output decrease, and BESS charge overlap, resulting in a local voltage drop in the distribution system. Also, at $t = 15\sim18$ minutes in Fig. 4.6, a local voltage rise occurs due to the overlap of the PV output rise and the BESS discharge. Thus, the localized and transient voltage abnormalities happened within a short period of 30 minutes. This scenario is difficult to handle for slow operating grid control equipment installed at fixed locations, such as a Load Ratio Transformer (LRT) and Step Voltage Regulator (SVR).

In this scenario, the DERMS center sets a target voltage range of $6.6\ \text{kV} \pm 3\%$. In other words, if the voltage is below 6.4 kV, the lower target limit is violated, and if the voltage is above 6.8 kV, the upper target limit is violated. It was assumed that the substation is operated at 6.7 kV.

In accordance with this target voltage range, an instance of the droop curve was set up as in Fig. 4.7. The slope range is from 6.4 kV to 6.8 kV. The max injection/absorption reactive power was set to ± 400 kVar considering the number of air-conditioners in a cluster, the air-conditioning capacity, and the load relation shown in Fig. 4.6.

4.4.2 VarDR Cluster Formation Modeling

In the distribution system model shown in Fig. 4.5, a group of building multi-type air-conditioners is widely distributed with one small office building at each node of the branch line so that they can be aggregated at any node in the distribution system. Each building was assumed to have five outdoor air-conditioning units with a rated power consumption of 20 kW.

The operation of the building multi-type air-conditioner was simulated using the power and room temperature dynamic model developed in [70]. This model is characterized by the inclusion of uncertainty due to the built-in control of the air-conditioners and the uncertainty of the heat load. The weather conditions were set to 14:00 in summer and an outside temperature of 35 °C. The heat load for each building was set to 0.5 °C at 14:00 in summer. Three heat load factors were used for each building: 0.5, 1.0, and 1.5. During normal operation without reactive power control, the heat load was set to consume approximately 10 kW per outdoor unit, or 50% of the rated value, in buildings with a heat load factor of 1.0. The room temperature side-effect limit during the VarDR operation was set at ±2 °C, and it was assumed that the air-conditioning user cooperated with this limit.

Four VarDR clusters were formed as shown in Fig. 4.5. Each VarDR cluster consists of 5 buildings and 25 air-conditioners. One DERMS aggregator per VarDR cluster manages and controls the reactive power of the respective cluster. The reference voltage V_R, as shown in Fig. 4.1, for each respective DERMS aggregator is the Node 3 voltage for cluster1, Node 6 voltage for cluster2, Node 7 voltage for cluster3, and Node 9 voltage for cluster4.

Upstream VarDR clusters 1 and 2 and downstream VarDR clusters 3 and 4 were used one by one to compare the voltage improvement. Thus, 10 buildings and 50 outdoor units were subject to reactive power control in two VarDR clusters in total.

In this simulation, the DERMS center dispatched the same Volt-Var droop curve parameters for all VarDR clusters; the shape of the droop curve is shown in Fig. 4.7. Self-oscillation is known to occur when the slope of the Volt-Var droop curve exceeds the maximum slope determined by the electrical characteristics of the distribution system [59]. It was confirmed in this simulation and

determined the slope of the droop curve with a safety margin. In this simulation, approximately the half-slope of the circuit constraint curve $f(V, Q)$ is used at Node 6, which is located at the midpoint of the trunk line, to provide a safety margin, as shown in Fig. 4.7.

4.5 Simulation Results

4.5.1 Voltage Recovery Effect

Figure 4.8 shows the simulation results when downstream VarDR clusters, cluster3 and cluster4 are used. Figure 4.9 shows the simulation results when upstream VarDR clusters, cluster1 and cluster2, are used. These figures include (a) the time series of the VarDR total reactive power and problem node voltage, and (b) the time series of the total active power P_A, total reactive power Q_A, and average room temperature deviation T_{SAA} for the whole building participating in VarDR.

Here, the problem nodes were Node 11, where EV charging caused a low voltage deviation, and Node 35, where PV generation caused a high voltage deviation. The voltage graph for the problem node in (a) shows the voltage change without VarDR as a solid gray line for comparison.

In both Figs. 4.8 and 4.9, it can be seen that the outline of the time variation waveform of the grid voltage shows a time variation based on the sinusoidal variation of PV generation, superimposed on top of the staircase and exponential waveforms of the EV stands and the upper and lower square waveforms of the BESS charging and discharging.

For Node 11 in Fig. 4.8(a), the voltage is below the lower limit of 6.40 kV without VarDR during $t = 5{\sim}8$ minutes, but with VarDR the voltage increases by about 0.07 kV to around 6.53 kV due to the reactive power injection of about 400 kVar in total from the downstream clusters. During $t = 15{\sim}18$ minutes, the Node 35 voltage is above the upper limit of 6.80 kV without VarDR, but drops to around 6.77 kV with VarDR.

Similarly, the upstream VarDR clusters shown in Fig. 4.9(a) avoid high and low voltage limit deviations, but the voltage recovery is reduced by 0.04 kV, i.e., less than that of Fig. 4.8(a)

when VarDR is performed with downstream clusters. Figure 4.10 shows that all other nodes voltage are

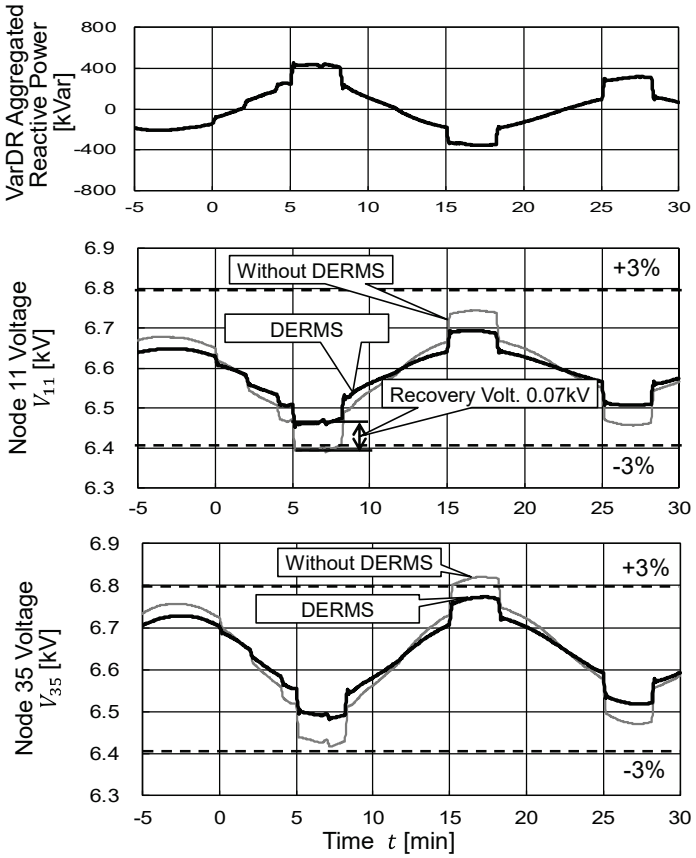

(a) VarDR total reactive power and problematic node voltages

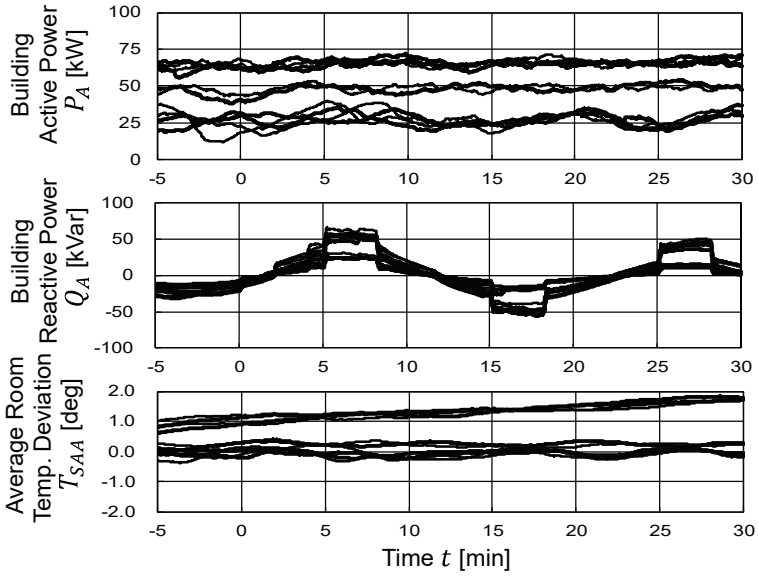

(b) Active power, reactive power, average room temperature deviation of each building

Fig. 4.8 Simulation result with VarDR cluster3 and cluster4
(in case of downstream clusters)

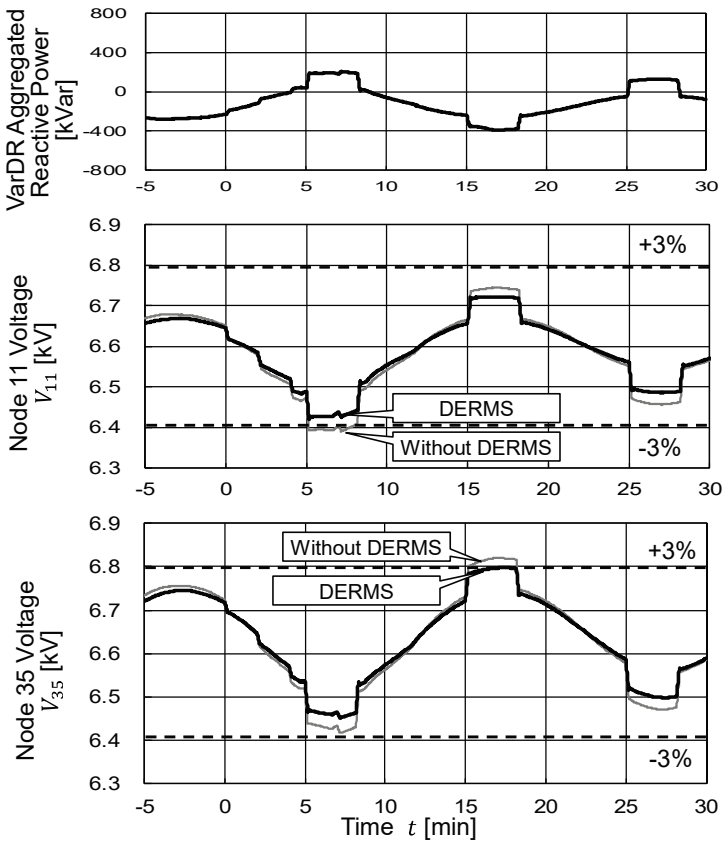

(a) VarDR total reactive power and problematic node voltages

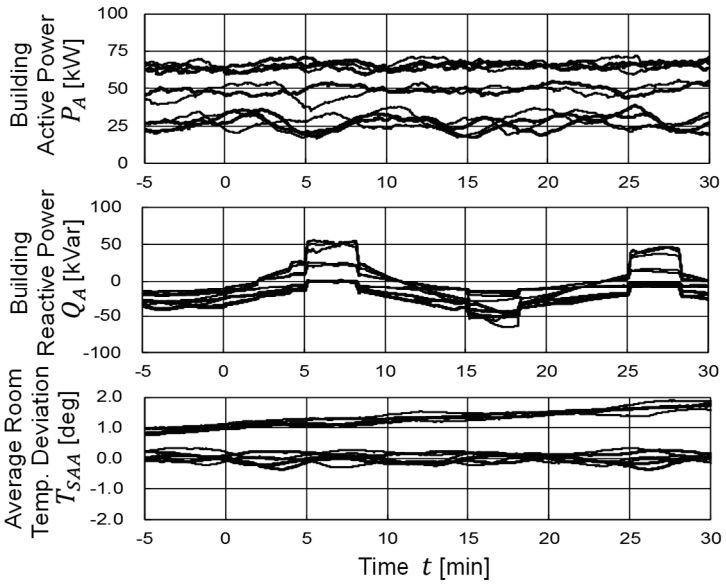

(b) Active power, reactive power, average room temperature deviation of each building

Fig. 4.9 Simulation result with VarDR cluster1 and cluster2
(in the case of upstream clusters)

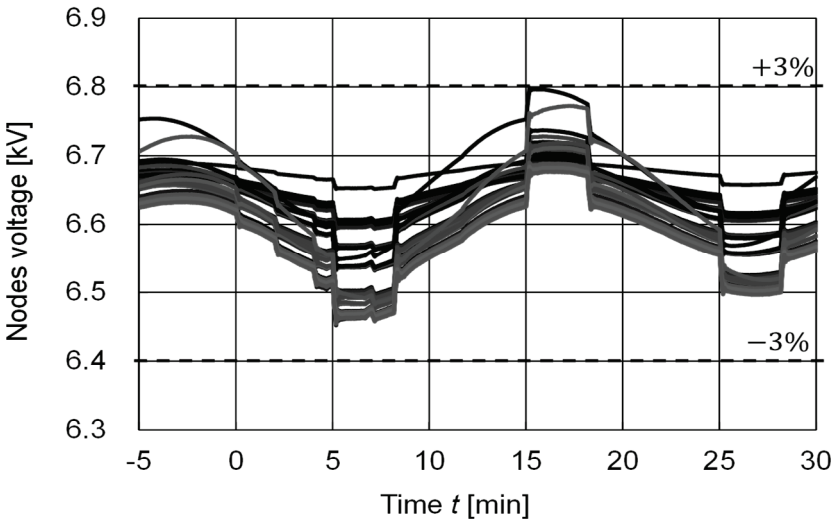

Fig. 4.10 All nodes voltage (in case of downstream clusters)

remain within the acceptable voltage limit (±3%) when VarDR is performed with downstream clusters.

4.5.2 Air-conditioning Side-effect

In Figs. 4.8(b) and 4.9(b), buildings were able to continue the reactive power control specified by the DERMS center for 30 minutes without exceeding the whole building average room temperature deviation T_{SAA} (up to +2 °C).

The reason why the active power of buildings with low power consumption, that is, low thermal load, is actually moving up and down is that the DERMS aggregator is issuing more reactive power commands to air-conditioners that have room temperature comfort margins established by the proportional allocation method of Eqs. (4.1)-(4.3).

Conversely, the DERMS aggregator issued fewer reactive power commands to air-conditioners with high thermal loads and low room temperature comfort margins, and the range of change in active power was also smaller. In other words, T_{SAA} deviations were prevented because the cooling capacity was not significantly limited by the reactive power control.

However, in some buildings, T_{SAA} almost reached +2 °C at the end of 30 minutes, and if VarDR were to be continued for longer than this, some of them would leave the VarDR event

(called opt-out). In this case, priority should also be given to the VarDR cluster that is most effective in restoring the voltage of the node where the problem occurs.

4．6 Discussion on Volt-Var Droop Curve Control

In Figs. 4.8 and 4.9 simulation results are shown for DERMS Volt-Var droop curve control with VarDR of building multi-type air-conditioner clusters fixed slop of droop curve. To further enhance the voltage control effect, the simulation experiments were repeated while changing the slope of the droop curve, and the change in voltage recovery values were investigated under the same scenario.

As shown in Figs. 4.8(a) and 4.9(a), reactive power control using the VarDR cluster of a group of building multi-type air-conditioners avoided both high and low voltage deviations, although the scenario included localized high and low voltage deviations in a short period of 30 minutes. However, the voltage recovery widths differed between the upstream and downstream clusters. The reasons for this are twofold.

The first reason is the location of the VarDR cluster in the distribution system. Because reactive power affects voltage variations along its inject/absorb path, it is more effective at performing reactive power control near the problem nodes [71]. At $t = 15{\sim}18$ minutes, the voltage recovery is greater with cluster3 and cluster4, which are closer to the problem node, even though the absolute values of the total reactive powers for clusters 3 and 4 in Fig. 4.8(a) and clusters 1 and 2 in Fig. 4.9(a) are almost the same.

The second reason is due to the shape of the droop curve at $t = 5{\sim}10$ minutes and $t = 25{\sim}30$ minutes. Namely, when voltage dips occur in the distribution system, the total reactive power injection/absorption of VarDR clusters 1 and 2 in Fig. 4.9 is lower than that of VarDR clusters 3 and 4 in Fig. 4.8. This is because Nodes 3 and 6, clusters 1 and 2 to reference the droop curve, are close to the substation and do not deviate from the reference voltage significantly. Thus, the DERMS aggregator issues only a small number of reactive power commands to each building multi-type air-conditioner using the droop curve slope in Fig. 4.7.

Chapter 5　Saturated GFM Inverter Support with VarDR

This chapter investigates whether it's possible to support continuous operation of saturated GFM inverter by reactive power demand response (VarDR) using active converters of building multi-type air-conditioners. The characteristics of GFM equivalent impedance and the operation of GFM with and without VarDR is also explored.

５．１ Importance of GFM Inverter in Microgrid

As the introduction of distributed power sources progresses, studies are underway on introduction of microgrids that supply power to consumers independently of the power system in emergencies such as accidents and disasters [75].

In a microgrid that uses photovoltaic power generation, large-capacity storage batteries, etc. as the main power source, Grid ForMing: GFM inverter [76] and [77] plays the role of establishing the system voltage and frequency instead of the synchronous generator. Microgrids without substation or synchronous generator require at least one DER with a GFM inverter as shown in Fig. 5.1. Unlike substations, which are installed with considerable allowance for system load, the capacity of GFM inverters used in emergencies is expected to be limited. GFM inverters are prone to voltage fluctuations and overcurrent due to load fluctuations, but because they are used in emergencies, they are required to continue operating even if the rating is exceeded to some extent [61].

One way to support continued operation of GFM inverters is to maintain voltage and improve power factor through reactive power control of customer equipment. In [70], by the author, targeting a normal distribution system connected to a substation, reactive power demand response

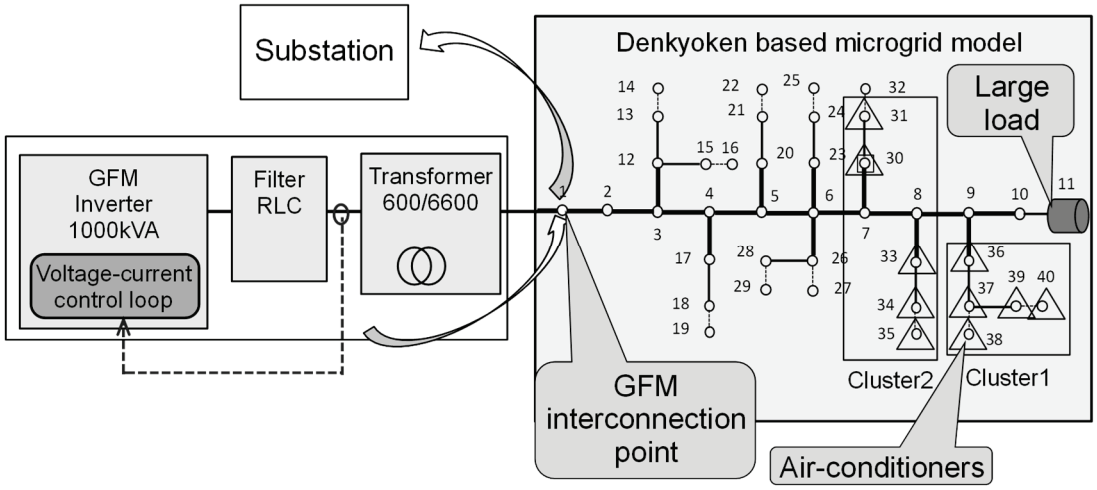

Fig. 5.1　GFM interconnection with distribution network

(Var Demand Response : VarDR), and showed that local and transient voltage fluctuations can be dealt with by controlling customer equipment.

５．２ GFM Inverter Support by Building Air-conditioning VarDR

It's well known that, in a normal distribution system, the capacity of the substation has a considerable margin for the load, and it can be assumed that the primary side is connected to an infinite bus. Fluctuations in the sending voltage due to fluctuations of load are less likely to occur. On the other hand, the capacity of GFM inverters installed for emergency use is limited, and the voltage fluctuates greatly due to load fluctuations in the distribution system.

When the voltage drops due to the load, the output current rises due to the voltage recovery control of GFM inverter itself. As the load is further increased, the rated current is exceeded and the limiter provided for circuit protection is reached, and the current begins to be limited. As a result, the voltage drops further, eventually reaching the lower operating voltage limit, causing the GFM inverter to stop operating and making it impossible to maintain the microgrid.

In addition, in a microgrid using GFM inverters, the GFM inverters themselves must supply or consume the active power and reactive power generated in the distribution system. A drop in power factor of the GFM inverter due to reactive power leads to an increase in current, which accelerates the limiter.

Therefore, in this Chapter, the voltage recovery is performed at the GFM inverter's sending end and customer's receiving end by supplying reactive power from building multi-type air-conditioners installed in evacuation shelter buildings, and reduce the current by improving the power factor of the GFM inverter. In this Chapter, even if a microgrid is formed in the event of a disaster, it is assumed that the air-conditioning operation of the evacuation shelter building will continue, and that reactive power can be supplied in response to commands from the Distributed Energy Management System (DERMS).

5．3 GFM Inverter Model

5.3.1 Equivalent Impedance of GFM Inverter

In this research, the equivalent impedance model of the GFM inverter described in Reference [76] is used as it is. A feature of this model is that it can handle the equivalent impedance of a saturated GFM inverter in a steady state. Since the effect of reactive power control depends on the operation of this model, this section deliberately explains the model in Reference [76].

Fig. 5.2 shows a control block diagram of the GFM inverter. In the control block of Fig. 5.2, a voltage and current feedback loop is developed in the αβ coordinate system. Reference [76] derives the following relationship from Fig. 5.1.

$$U_{\alpha\beta} = V_{\alpha\beta}^{G} + PR_1(M - I)I_{\alpha\beta}^{G} \quad + PR_1 \cdot M \cdot PR_2 \left(V_{\alpha\beta}^{Gref} - V_{\alpha\beta}^{G}\right) \tag{5.1}$$

The second term on the right side is the current control loop, and the third term on the right side is the determinant representing the voltage control loop. Where $U_{\alpha\beta}$ [V] is the command voltage to the PWM inverter, $V_{\alpha\beta}^{G}$ [V] is the output voltage of the GFM inverter, $I_{\alpha\beta}^{G}$ [A] is output current, and $V_{\alpha\beta}^{Gref}$[V] is the target reference voltage. PR_1 is the transfer function of proportional resonance controller in current feedback loop, and PR_2 is the transfer function of proportional resonance controller in voltage feedback loop. These are all vectors in the αβ coordinate system.

M is a diagonal matrix whose components are the current limiting coefficients m.

$$m = \begin{cases} 1 & |I_{abc}| \le I_{lim} \\ \dfrac{I_{lim}}{|I_{abc}|} & |I_{abc}| > I_{lim} \end{cases} \tag{5.2}$$

Here, I_{abc} [A] is the effective value of the line current per phase. In this research, for the sake of simplicity, it is assumed that the distribution system is a three-phase balanced load and that the line current of each phase is the same value. In Reference [76], as an example, the current is limited by Eq. (5.2), but the actual implementation differs depending on the inverter manufacturer design.

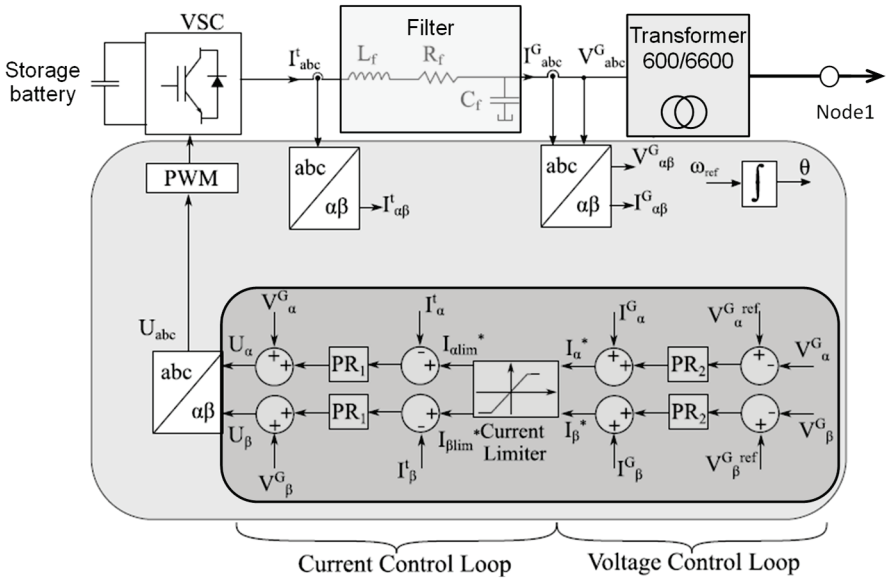

Fig. 5.2 Control Block Diagram of a GFM Inverter; adopted from [76]

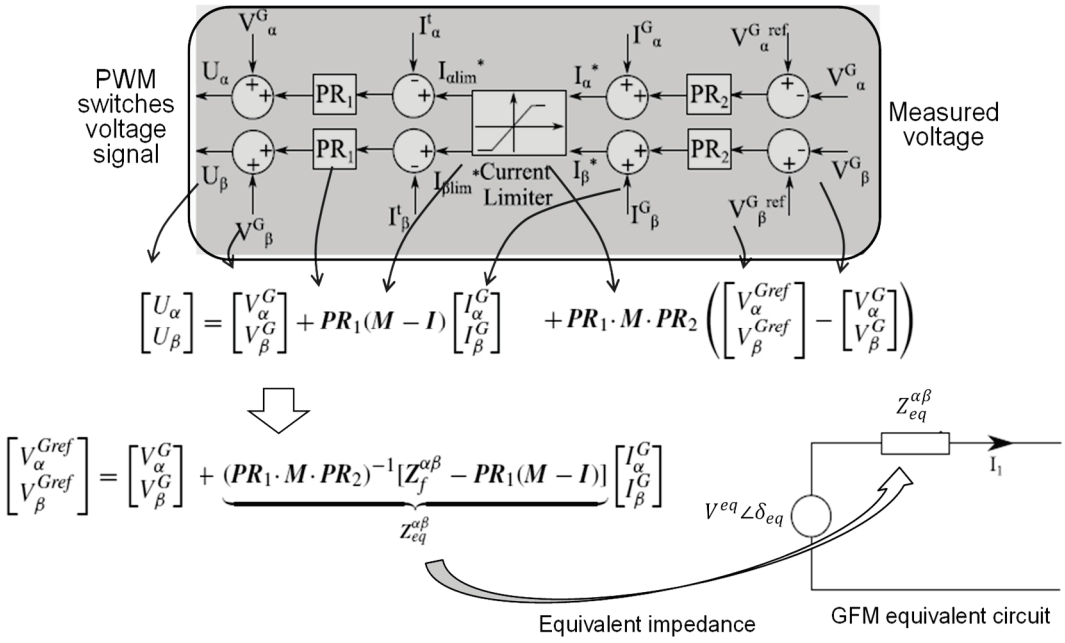

$$\begin{bmatrix} U_\alpha \\ U_\beta \end{bmatrix} = \begin{bmatrix} V_\alpha^G \\ V_\beta^G \end{bmatrix} + \boldsymbol{PR}_1(\boldsymbol{M}-\boldsymbol{I}) \begin{bmatrix} I_\alpha^G \\ I_\beta^G \end{bmatrix} + \boldsymbol{PR}_1 \cdot \boldsymbol{M} \cdot \boldsymbol{PR}_2 \left(\begin{bmatrix} V_\alpha^{Gref} \\ V_\beta^{Gref} \end{bmatrix} - \begin{bmatrix} V_\alpha^G \\ V_\beta^G \end{bmatrix} \right)$$

$$\begin{bmatrix} V_\alpha^{Gref} \\ V_\beta^{Gref} \end{bmatrix} = \begin{bmatrix} V_\alpha^G \\ V_\beta^G \end{bmatrix} + \underbrace{(\boldsymbol{PR}_1 \cdot \boldsymbol{M} \cdot \boldsymbol{PR}_2)^{-1}[Z_f^{\alpha\beta} - \boldsymbol{PR}_1(\boldsymbol{M}-\boldsymbol{I})]}_{Z_{eq}^{\alpha\beta}} \begin{bmatrix} I_\alpha^G \\ I_\beta^G \end{bmatrix}$$

Fig. 5.3 GFM equivalent impedance and transfer function

Furthermore, the following relationship is obtained by modifying Eq. (5.1) from the relationship between the filter impedance $Z_f^{\alpha\beta}$ and $U_{\alpha\beta}$ on the output side of the GFM inverter.

$$V_{\alpha\beta}^{Gref} = V_{\alpha\beta}^{G} + (PR_1 \cdot M \cdot PR_2)^{-1}\left[Z_f^{\alpha\beta} - PR_1(M - I)\right] I_{\alpha\beta}^{G} \tag{5.3}$$

$$Z_{eq}^{\alpha\beta} = \frac{R_f + j\omega_{ref}L_f - (m-1)(kp_1 + \frac{jki_1}{3\omega_{ref}})}{m(kp_1 + \frac{jki_1}{3\omega_{ref}})(kp_2 + \frac{j2ki_2}{-a_{\alpha\beta} + j2 + \left(\frac{\omega_c}{\omega_{ref}}\right)^2})} \tag{5.4}$$

Simplifying the Eq. (5.3) in zero-positive-negative sequence frame, we can get the equivalent impedance $Z_{eq}^{\alpha\beta}$ of the GFM inverter as Eq. (5.4). Reference [76] shows that, as a result, the GFM inverter can be treated as an equivalent circuit in which the equivalent impedance $Z_{eq}^{\alpha\beta}$ is connected to the ideal voltage source, as shown in Fig. 5.3 and Fig. 5.5. If this is used to convert to impedance Z_{eq} in three phases, it can be described as a function with the parameters shown in Table 1 as variables. Fig. 5.4 shows the conceptual image of m and equivalent impedance $Z_{eq}^{\alpha\beta}$.

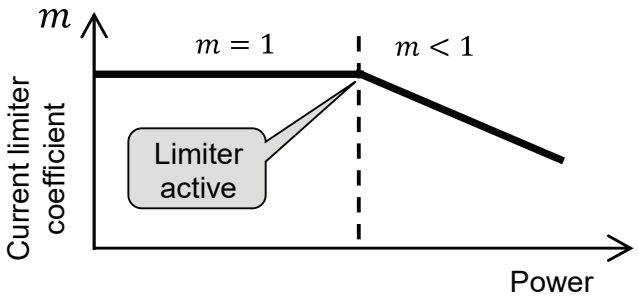

a) Transition of m, Eq. (5.2)

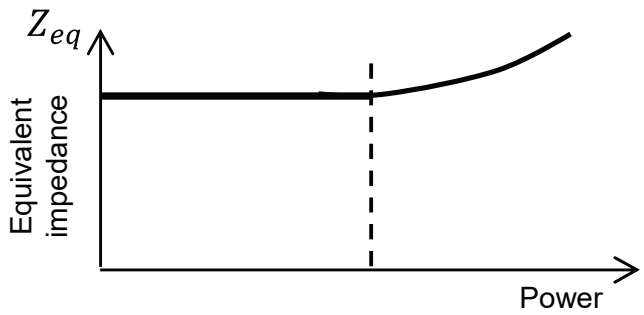

b) Non-linear behavior of Z_{eq}, Eq. (5.4)

Fig. 5.4 Conceptual image of current limiter coefficient and GFM equivalent impedance

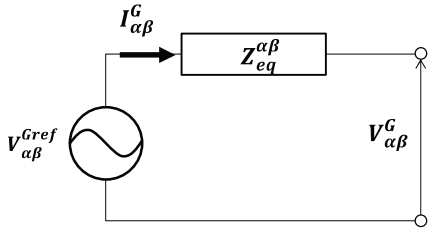

Fig. 5.5 Equivalent impedance circuit of a GFM inverter

Table 5.1 GFM Inverter Parameters; adopted from [76]

Symbol	Meaning	Value
R_f	Link point filter resistance	0.015 Ω
L_f	Link point filter reactance	0.42 mH
ω_{ref}	Reference angular frequency	377 rad/sec (60 Hz)
k_{p1}	Proportional resonant controller gain of PR_1	1
k_{p2}	Proportional resonant controller gain of PR_2	5
k_{i1}	Proportional resonant controller gain of current control loop	1
k_{i2}	Proportional resonant controller gain of PR_2	0.5
$a_{\alpha\beta}$	2nd order factor of PR_2	5
ω_c	Natural frequency of PR_2	$0.2\omega_{ref}$
I_{lim}	Current limit value	962 A
V_{nom}	Nominal voltage	600 V
S_{nom}	Nominal output	1000 kVA

5.3.2 GFM Inverter Characteristics

Fig. 5.6 shows the change in equivalent impedance amplitude $|Z_{eq}|$ of the GFM inverter when parameters shown in Table 1 are used.

The equivalent impedance is constant until the current I_{abc} of the GFM inverter reaches the limit start current I_{lim}, but when it reaches I_{lim}, it rises non-linearly, reaching about twice the impedance before the start of limit at approximately 1.2 times of I_{lim}. GFM stop the operation when its voltage drops below the 12% of rating voltage, IEEE 1547-2018 criteria [61].

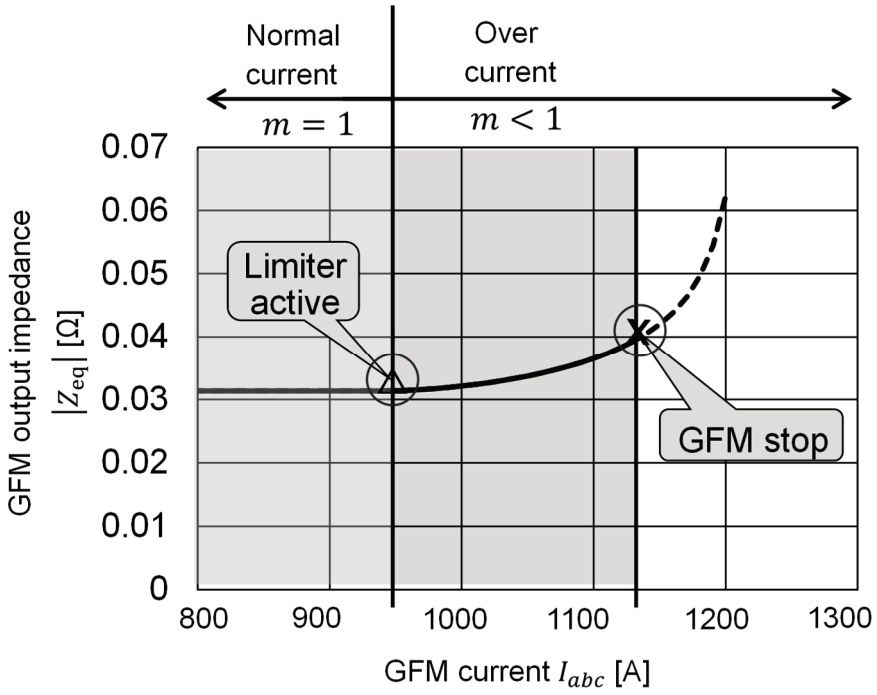

Fig. 5.6 Equivalent impedance characteristics of GFM inverter

5．4 Simulation Conditions

5.4.1 Microgrid Model

In this research, based on the urban area pattern C2 model [63] from Electric Technology Research Association research group, the microgrid shown in Fig. 5.1 is defined and used for the simulation. In this microgrid, one GFM inverter with rated capacity $S_{nom} = 1000$ kVA shown in Table 5.1 is installed instead of the original distribution substation in Node 1. The rated voltage V_{nom} of the GFM inverter is 600 V, which is boosted to 6.6 kV for grid connection.

According to IEEE1547-2018 [61], which is a regulation for grid connection of distributed energy sources, the GFM inverter is required to operate up to -12% of the reference voltage. In this research, the 5.8 kV (-12% of 6.6 kV) was set as the operating lower limit voltage V_{stop} [kV] of the GFM inverter, and the operation was stopped when the node voltage fell

Table 5.2 List of loads in microgrid model

Load type	Load per node	Number of nodes	Total load
Air-conditioners (constant load)	80 kW + j10 kVar (per building)	10	0.80 MW
Large load	0~300 kW	1	0~0.30 MW
-	-	Max. load	1.10 MW

below V_{stop}.

Assuming an emergency such as a disaster, there is no background load, and only the 10 evacuation shelter buildings and a large load at the end of the trunk line are connected.

The evacuation shelter building is equipped with 5 building multi-type air-conditioners with rated power consumption of 20 kW, and assumes a fixed consumption of 16 kW. In other words, it is assumed that a single building consumes a total of 80 kW. In this Chapter, air-conditioners load is assumed the constant load.

The large load was assumed to produce the load changing effect at the end of turn line from 0 to 300 kW. The maximum total system load is about 1100 kW + j100kVar. Table 5.2 shows the list of loads in microgrid model.

5.4.2 Building Multi-type Air-conditioners VarDR Cluster

It is assumed that the air-conditioners in each building are equipped with active converters, and reactive power control can be performed by commands from DERMS. The active converter has a rated capacity of 20 kVA and a minimum operating power factor of 0.4, up to which reactive power can be supplied to maintain the microgrid.

As shown in Fig. 5.1, 5 buildings and a total of 25 air-conditioners are grouped together to form a “VarDR cluster”. In this microgrid model example, each VarDR cluster supply the constant −200 kVar reactive power to maintain the voltage of saturated GFM and prolong its operation.

5．5 Simulation Results

5.5.1 VarDR Effect on Saturated GFM Inverter's Operation

Here, the large load at the end of trunk line is changed from 0 to 300 kW. Fig. 5.7 shows the results of microgrid VarDR simulation. In Fig. 5.7, gray line shows the GFM interconnection point voltage without VarDR and black line shows GFM interconnection point voltage with VarDR.

As shown in Fig. 5.7, without VarDR, the voltage drops as the load rises. Immediately before reaching the maximum load, the current limit is activated at 914 kVA, the voltage drops gradually, reaches the operating lower limit voltage V_{stop}, and the GFM inverter stops operating.

With VarDR, the voltage is about 0.1 kV higher than without VarDR. In addition, the voltage drop rate after activation of limiter is more gradual than without VarDR.. As a result, the GFM continuous the operation up to 1037 kVA this is the power more than its capacity.

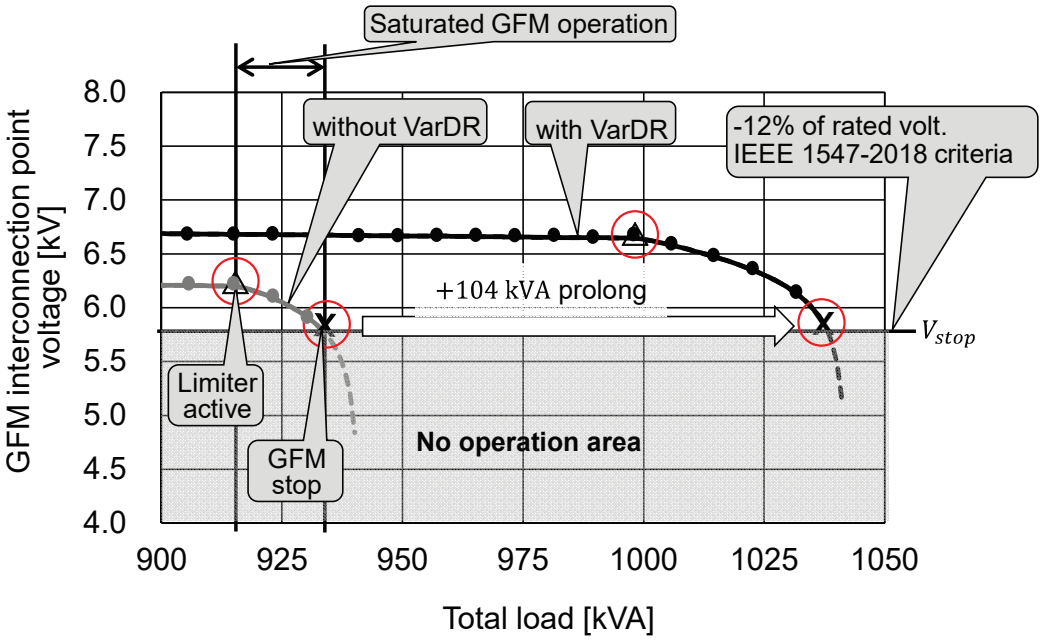

Fig. 5.7 Characteristics of saturated GFM inverter with and without VarDR

５．６ Findings for VarDR Effect in Microgrid

In this research, in a microgrid that uses GFM inverter to maintain voltage and frequency, it is investigated whether it's possible to support continuous operation of saturated GFM inverter by reactive power demand response (VarDR) using active converters in building air-conditioning load.

Numerical simulations were conducted to clarify the effect of VarDR on the operation of the GFM inverter using an equivalent impedance model in the steady state of the GFM inverter.

As a result, the following findings were obtained.

① By improving the power factor of the GFM inverter and increasing the voltage at the sending end, an example was obtained in which the operating range was extended by about 10% relative to the rated capacity.

② Even if the GFM inverter is stop without VarDR, VarDR can continue operation and keep the voltage on the customer side within ±5% of rated voltage.

In the future, a method will be studied to monitor the power factor of the GFM inverter and control the reactive power, and will confirm the effect of VarDR in the case where the Grid FoLlowing: GFL inverter powered by photovoltaic power generation or large storage batteries is connected.

Chapter 6 Discussions

This chapter provides an overall discussion on methodology, system effects due to EVs and DERs, and compensation technique to overcome the effects.

6．1 VarDR Effectiveness

It is well known that the effect of reactive power differs depending on the locational relationship in the distribution system. In the future distribution system, there is a possibility that problem nodes will be scattered temporally and spatially due to the spread of EVs and DERs.

The sensitivity coefficients of VLSM can be used to present the relationship between reactive power and location of problematic node. In this research, the sensitivity coefficients of VSLM are formulated using graph theory and simple voltage drop equation. The sensitivity coefficients are the function of voltage, the sum of reactances of common path between problematic node and helping node from source node, and sum of line length of common path between problematic node and helping node from source node.

An idea is presented to use the building multi-type air-conditioners as the new source of reactive power. The reactive power demand response (VarDR) using clusters of distributed building multi-type air-conditioners will be effective because its reactive power can be supplied each time at any location. It is not necessary to add such as large capacity phase adjustment equipment.

As shown in Chapter 3, when a building multi-type air-conditioner is operating at 50% of the rated power consumption (i.e., when the air-conditioning load is 50% of the rated cooling capacity), the maximum utilization of the reactive power Q_{max} is $0.86S_{max}$.

This means that it is possible to inject/absorb the reactive power up to about 86% of the rated capacity of the active converter of building multi-type air-conditioner without affecting the active power for air-conditioning.

Normally, the rated cooling capacity of building multi-type air-conditioners has a margin for the heat load of 50%. Therefore, they are rarely operated at full power all the time except during room temperature recovery operation (so-called pull-down operation) immediately after operation is stopped such as first time in the morning or during lunch break, or on extremely hot days. Since air-conditioners often operate at about half of its rated capacity, it can be considered that air-conditioners have a large capacity of reactive power that reaches approximately 86% of the

rated capacity of the active converter for a large part of the operation time.

In addition, during experiment, although the VarDR was set to about 10 minutes according to the charging time of the future quick EV chargers, the reactive power injection can be continued as long as in the free run operating mode. In free run operating mode, operating range of active power is not limited by the restrictions of neither the minimum power factor nor the rated capacity of the active converter. Consequently, the room temperature comfort is not affected due to any limitation on active power.

It is observed that the air-conditioners of buildings with high heat loads opted-out the VarDR operation during the VarDR period due to the rise in room temperature. The simple evenly allocation of reactive power shown in Eq. (3.5) causes opt-out as the air-conditioning comfort deteriorates, and the target reactive power might be not achieved even in a short period VarDR about 10 minutes.

To overcome the opt-out issue, the reactive power allocation method based on Eq. (3.6), which takes into account the air-conditioning load and the room air-conditioning comfort, is used to allocate more reactive power to air-conditions of the buildings with a room temperature margin and allocate the low amount of reactive power to the air-conditions of the buildings where the room temperature is deviating from the set temperature. As a result, all the building multi-type air-conditioners could keep the VarDR event.

If the reactive power is injected just after the start of air-conditioning, it may cause a delay in the room temperature becomes comfort, so it is necessary to share more of the reactive power from the air-conditioners that are already in steady state and their room temperatures are comfort. The proposed allocation method can realize such a way.

If reactive power injection is required for a longer period, or if more reactive power injection is required, it is feasible to perform VarDR using more clusters of building multi-type air-conditioners.

6.2 VarDR DERMS Volt-Var Control Performance

Chapter 4 shows the simulation results for DERMS Volt-Var droop curve control with VarDR of building multi-type air-conditioner clusters, the gradient of the droop curve is shown by one value as Fig. 5.1 illustrated.

Naturally, a larger slope of the droop curve indicates a larger reactive power command value for the same voltage change, resulting in a greater voltage control effect. However, it is known that if the slope of the droop curve is increased to the same level as the absolute value of the slope of the operating constraint curve, prolonged control oscillation occurs, causing control divergence [59]. The absolute value of the slope of the operating constraint curve is about 4000 kVar/kV, which is the limit calculated from the numerical values for the presented simulation model.

Another factor that causes oscillation is the effect of the Volt-Var droop curve look-up period, or control period. In this research, the control period was assumed to be 10 seconds, which is the communication interval itself, and the active converter response time, which was assumed to be 1 second.

As a result, in Fig. 5.2, the oscillations were observed to occur and diverge at around $t = 8$ minute. The oscillations were not observed before that point, because the command value of reactive power was in the saturated region of the droop curve.

Thus, although the slope of the droop curve should be as large as possible to increase the voltage control effect, it is necessary to design the DERMS Volt-Var droop curve control by estimating the risk of VarDR oscillation. This is done by identifying the communication delay, control period, and response time of active converter of a building multi-type air-conditioner.

Reactive power control using the VarDR cluster of a group of building multi-type air-conditioners avoided both high and low voltage variations, although the scenario included localized high and low voltage variations in a short period of 30 minutes. However, the voltage recovery widths differed between the upstream and downstream clusters. The reasons for this are twofold.

The first reason is the location of the VarDR cluster in the distribution system. Because reactive

power affects voltage variations along its inject/absorb path, it is more effective at performing reactive power control near the problem nodes. The advantage of VarDR for building multi-type air-conditioners is that the reactive power can be aggregated anywhere in the distribution system, and a DERMS can select a more effective VarDR cluster on a case-by-case basis depending on the location of the problem node.

The second reason is due to the shape of the droop curve. Specifically, when voltage dips occur in the distribution system, the total reactive power injection/absorption of VarDR at upstream side is lower than that of VarDR at downstream side. This is because upstream side are close to the substation and do not deviate from the reference voltage significantly. Thus, the DERMS aggregator issues only a small number of reactive power commands to each building multi-type air-conditioner using the droop curve slope.

Figure 5.1 plots the voltage recovery effect under a varying slope of the droop curve in this simulation setup. Naturally, a larger slope of the droop curve indicates a larger reactive power command value for the same voltage change, resulting in a greater voltage control effect. However, it is known that if the slope of the droop curve is increased to the same level as the absolute value of the slope of the operating constraint curve, prolonged control oscillation occurs, causing control divergence. The absolute value of the slope of the operating constraint curve is about 4000 kVar/kV, which is the limit calculated from the numerical values for the present

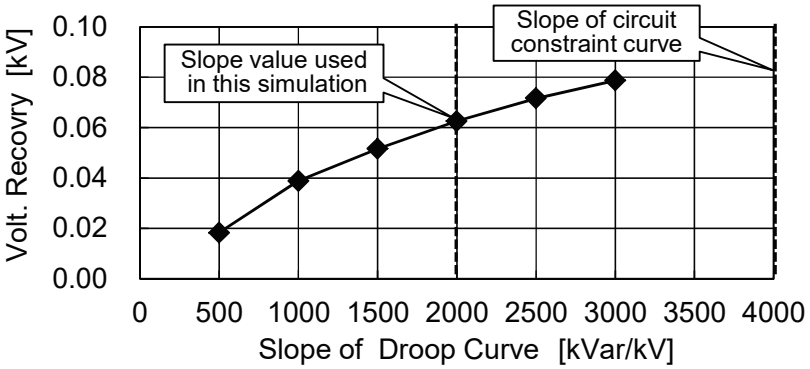

Fig. 5.1 Droop curve slope, voltage recovery effect and the gradient limit due to the circuit constraint

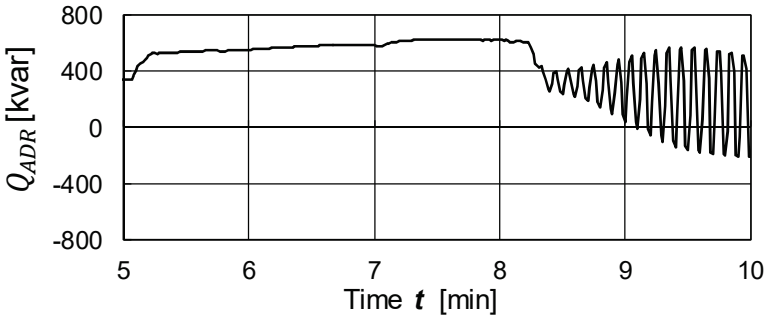

Fig. 5.2 Example of oscillation of controlled output of reactive power due to the steep slope of the Volt-Var droop curve

simulation model.

Figure 5.2 shows the case where the absolute value of the droop curve slope is adjusted to the absolute value of the constraint curve slope (4000 kVar/kV), while other conditions except the droop curve slope are kept the same. The vertical axis shows the total reactive power injected to the grid by a cluster.

In this research, the same Volt-Var droop curve was used for all VarDR clusters, but in the future, the reactive power adjustment capability of VarDR clusters could be enhanced by changing the zero-crossing point and slope of the droop curve according to the locations of VarDR clusters in relation to the nodes where problems occur. Furthermore, the value of the location should be evaluated for the voltage control of a distribution system using not only the VarDR as shown in this research but also in combination with other resources, such as battery systems.

Furthermore, slope of Volt-Var droop curve also depends on X/R ratio of distribution system [59]. In future research, the VLSM, which is presented in this research, could be used for setting the slope of Volt-Var droop curve for DERMS control of VarDR.

6．3 Costumer Incentives

Using limited information and large assumptions, a trial incentive calculation (annually) of VarDR for a typical small office building is conducted.

This is a rough trial incentive calculation. As in Chapter 3, two-story office building is assumed

with a total floor area of 1500 square meters and has 5 building multi-type air-conditioners (5 outdoor units). Assuming that during VarDR this building can provide reactive power of 50 kVar for 30 minutes, so, 25 kVarh per building.

Considering the severe distribution system situation in 10 years from now, the number of days for VarDR to be implemented per year is 100 days, which is 50% of 200 weekdays. In other words, the annual number of VarDR implementations per building is supposed 100. Therefore, the annual amount of reactive power generated by VarDR per building is rather large, $25 \text{ x} 100 = 2500$ kVarh/building/year.

Assuming that the VarDR unit price is 28 JPY/kVarh (JPY: Japanese Yen). So, the annual incentive per building will be $2500 \text{ x } 28 = 70000$ JPY and for 10 years 70000 JPY x 10 years = 700000 JPY/building. It seems that, for small two-story office building, the 700000 JPY incentive for 10 years is not bad.

However, in future research, the concrete VarDR incentive mechanisms have to be analyzed, aiming to attract the customers for VarDR.

Chapter 7 Conclusion

This research proposed a concrete method for building multi-type air-conditioners to perform reactive power demand response. It named as VarDR: Var Demand Response. An example scenario is modeled in which high and low voltage violations occurred due to EV charging, PV output fluctuations and BESS charging/discharging for model duration of 30 minutes. The effectiveness of voltage recovery by the Volt-Var droop curve was confirmed using the DERMS real-time simulator. The conclusions obtained are as follows.

① The VarDR method uses only everywhere-existing equipment, i.e., building multi-type air-conditioners; consequently it can select an ad hoc cluster of buildings neighboring the problematic location in the distribution system.

② In the modeled scenario, the VarDR method can utilize approximately 86% of maximum reactive power from the active converter built-in the air-conditioner while maintaining comfort within 1.0 ℃ deviation from the set point temperature.

③ The proposed system design of DERMS Volt-Var control for VarDR effectively calculate the target reactive power and distributes it to the aggregators using proposed allocation algorithm while maintaining room comfort within set temperature limit.

④ In example microgrid model, VarDR can prolong the saturated GFM operation approximately 10% relative to the rated capacity.

In the future, a method is plan to study for optimally combining the amount of reactive power supply based on a positional relationship between clusters of air-conditioners and problem location in a distribution system.

Acknowledgements

First and foremost, I would like to express my gratitude to Professor Chuzo Ninagawa of the Smart Grid Power Control Engineering Joint Research Laboratory, Faculty of Engineering, Gifu University, for his guidance, tolerance, patience and support during this research and the writing dissertation. His wisdom and inspiring comments have always motivated me. His appropriate guidance and care helped me not only succeed academically, but it also made the Ph.D. process a positive and fulfilling experience.

I would like to express my thanks to Professor Hiroki Yoshida and Associate Professor Hirotaka Takano of the Department of Electrical, Electronic and Computer Engineering, Faculty of Engineering, Gifu University for their advice and guidance during the review process of this dissertation .

Thanks to Mr. Kenichi Bandou, Dr. Miwako Fujita and Mr. Takayoshi Murakawa of the Chubu Electric Power Company for the kind advice on future distribution system issuses.

Special thanks to Assistant Professor Yoshifumi Aoki of the Smart Grid Power Control Engineering Joint Research Laboratory, Faculty of Engineering, Gifu University, for his help and advice. I would like to take this opportunity to acknowledge his support for helping me academically and making the Ph.D. process go smoothly.

I would like to express my thanks to former Assistant Professor Shun Matsukawa of the Smart Grid Power Control Engineering Joint Research Laboratory, Mr. Keita Suzuki of the INTERLINK, Inc., former graduate students of Ninagawa laboratory Mr. Satoshi Goto and Mr. Hiroto Tsutsui, and students of Ninagawa laboratory Mr. Ryuichi Okada, Mr. Yusuke Takahashi and Mr. Koshi Ishikawa.

List of Publications

(1) Academic papers that form the basis of this dissertation.

① A. Iqbal, Y. Aoki, C. Ninagawa, T. Murakawa : "Reactive Power Demand Response for Distribution System with Neighboring Clusters of Building Multi-type Air-conditioners", IEEJ Transactions on Power and Energy, Vol. 142, No. 6, pp 306-314, June 2022. (Reviewed)

② A. Iqbal, Y. Aoki, C. Ninagawa, T. Murakawa : "DERMS Volt-Var Control of a Power Distribution System Using Clusters of Building Multi-type Air-conditioners", IEEJ Transactions on Power and Energy, Vol. 143, No. 1, 2023. (Reviewed)

(2) Other publications.

③ A. Iqbal, Y. Aoki, C. Ninagawa, J. Morikawa and S. Kondo : "Emulation Modeling on Rebound-Compensated Aggregation of Uncertain Demand Responses from a Large Number of Building Air-Conditioners", 2020 IEEE International Symposium on Systems Engineering (ISSE), pp. 1-6, Vienna, Austria, December 2020. (Reviewed)

④ K. Suzuki, A. Iqbal, Y. Aoki, C. Ninagawa and J. Morikawa : "Stochastic Characteristics of Large-scale FastADR Aggregation Discovered by Using Diverse Building Air-conditioner Emulators", 2021 IEEE 30th International Symposium on Industrial Electronics (ISIE), pp. 01-05, Kyoto, Japan, November 2021. (Reviewed)

⑤ Y. Aoki, A. Iqbal, R. Okada, C. Ninagawa, T. Murakawa, M. Fujita, K. Bando : "Reactive Power Demand Response using Clusters of Building Multi-type Air-conditioners in Distribution Networks", IEEJ Technical Meeting on Power Engineering, PE-22-078, March 2022. (Non-reviewed)

Appendix

Appendix A Building Multi-type Air-conditioner Power Control Model

The air-conditioning power and room temperature dynamic models [72] and [73] for the building multi-type air-conditioning power limit command are modeled by the difference equation as Eq. (A.1).

$$P(t+\Delta t) = P(t) + \Delta P(t)\Delta t \tag{A.1}$$

$$\Delta P(t) = S_{OV}^{PL} D_{DWN} + (1 - S_{OV}^{PL})\{S_{OV}^{TH} D_{DWN} + (1 - S_{OV}^{TH}) S_{FR}^{PL} S_{FR}^{TH} D_{UP}\} \tag{A.2}$$

$$T_{Ai}(t+\Delta t) = T_{Ai}(t) + \Delta T_{Ai}(t)\ \Delta t \tag{A.3}$$

$$\Delta T_{Ai}(t) = \frac{1}{C_{Hi}}\left(Q_{Li}(t) - Q_{ACi}(t)\right) \tag{A.4}$$

Where t [s] is the discrete time and the model operates with a sampling width Δt [s]. $P(t)$ [kW] is power consumption, $\Delta P(t)$ [kW/s] is the rate of change in power consumption, $T_{Ai}(t)$ [°C] is the measured room temperature of indoor unit i, and $\Delta T_{Ai}(t)$ [°C / s] is the change in room temperature rate.

First, the difference equation for power consumption is described. This model changes the power consumption $P(t)$ according to the power limit command value $L(t)$ and the temperature control required power $P^*(t)$ [kW]. The required temperature control power $P^*(t)$ is the target value of power consumed by the air-conditioner when the power limit command value $L(t)$ is released ($L(t) = \infty$).

In Eq. (A.2), D_{UP} [kW/s] is the power increase rate and D_{DWN} [kW/s] is the power decrease rate. S_{OV}^{PL} and S_{FR}^{PL} are control statuses indicating the relationship between the power limit command value $L(t)$ [kW] and power consumption $P(t)$, and take two values (0 or 1) according to the conditions shown in Table A.1. k_L in the table is the power consumption tracking coefficient with respect to the power limit command value. S_{OV}^{TH} and S_{FR}^{TH} are control statuses indicating the relationship between the temperature control required power $P^*(t)$ and the power consumption $P(t)$, and change as shown in Table A.2.

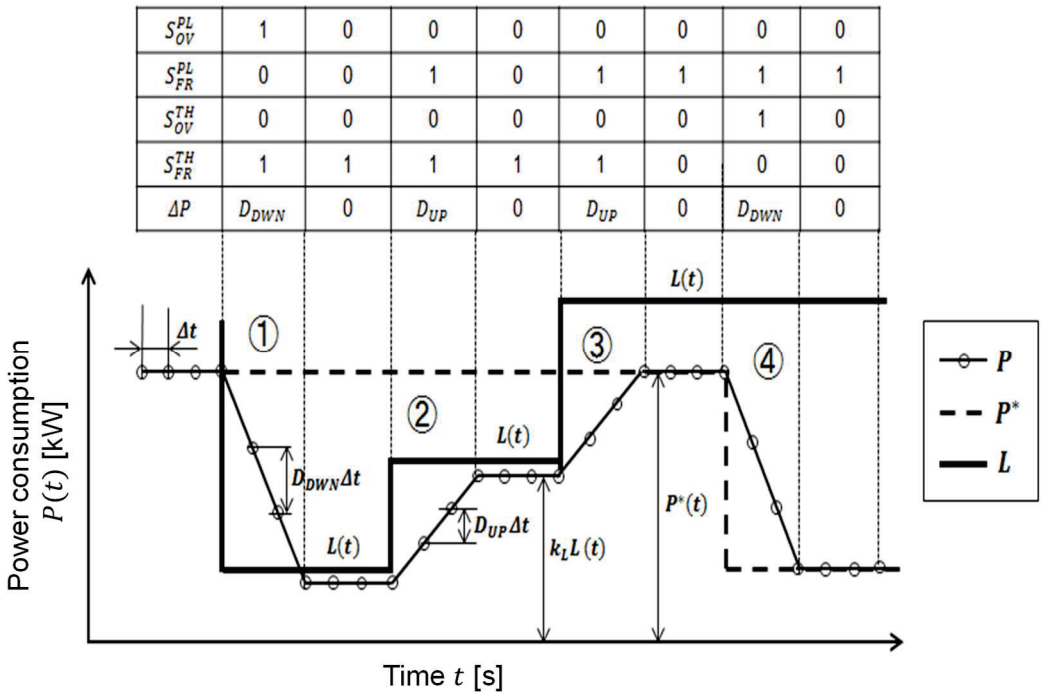

Fig. A.1 Relationship between power consumption and control status

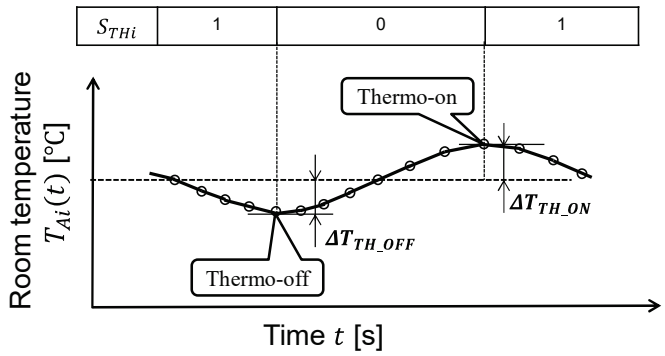

Fig. A.2 Thermo on/off state

Fig. A.1 shows the relationship between power consumption and control status. In Fig. A.1, the mode changes as ① ～ ④. ① if the current power consumption exceeds the power limit command value $L(t)$, it will drop to the power limit command value $L(t)$. ② when the power limit command value $L(t)$ is increased, the power consumption $P(t)$ increases following the power limit command value $L(t)$. ③ when the power limit command value $L(t)$exceeds the required temperature control power $P^*(t)$, the power consumption $P(t)$ increases to the required temperature control power $P^*(t)$. ④ when the required temperature control power $P^*(t)$ decreases, the power consumption $P(t)$decreases to the required temperature control power $P^*(t)$. $P(t)$ transitions with the rated power consumption P_{MAX} [kW] as the upper limit and the minimum power consumption P_{MIN} [kW] as the lower limit.

The difference equation at room temperature is described as Eq. (A.3). The difference equation for room temperature $T_{Ai}(t)$ exists independently for each indoor unit *i*. In other words, different room temperature dynamics are simulated for each indoor unit. In Eq. (A.4), C_{Hi} [kJ/℃] is the heat capacity, $Q_{Li}(t)$ [kW]is the heat load, $Q_{ACi}(t)$ [kW] is the air-conditioning capacity of the indoor unit.

The air-conditioning capacity $Q_{ACi}(t)$ of the indoor unit is distributed to the indoor unit by Eq. (A.5) using the air-conditioning capacity $Q_{AC}(t)$ [kW] exhibited by the outdoor unit.

$$Q_{AC}(t) = \eta_{COP} P(t) \tag{A.5}$$

$$Q_{ACi} = \frac{S_{THi} C_{Pi}}{\sum_{i=1}^{N_I} (S_{THi} C_{Pi})} Q_{AC} \tag{A.6}$$

Here, η_{COP} is called the coefficient of performance (COP) and represents the air-conditioning capacity [kW] per 1 [kW] of power consumption. $S_{THi}$is the thermo on / off status (0 or 1), C_{Pi} [kW] is the rated capacity of the indoor unit, and N_I is the number of indoor units.

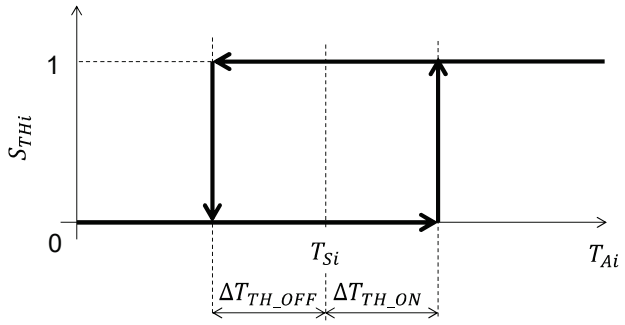

Fig. A.3 Thermo on/off hysteresis

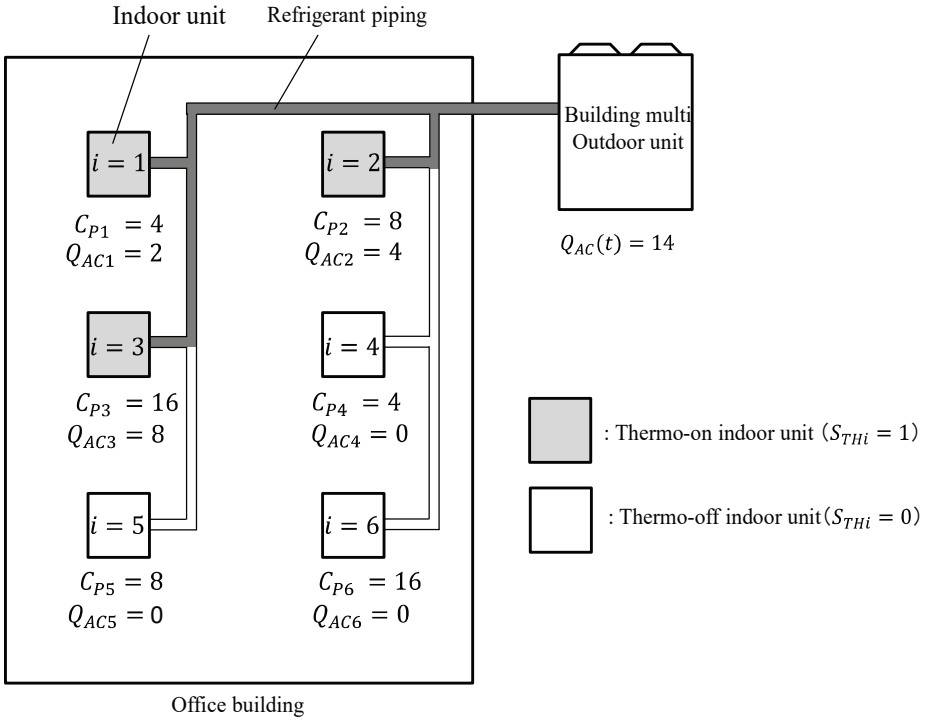

Fig. A.4 Cooling capacity distributed to indoor units

Thermo on/off is a control to switch on/off the air-conditioning of the indoor unit based on the difference between the set room temperature T_{Si} and the measured room temperature $T_{Ai}(t)$. As shown in Fig. A.2, when the measured room temperature $T_{Ai}(\mathrm{t})$ of the indoor unit reaches $T_{Si} - \Delta T_{TH\_OFF}$, the thermo unit is turned off ($S_{THi} = 0$), and the air-conditioning of the indoor unit stops. When the room temperature rises and reaches $T_{SETi} + \Delta T_{TH\_OFF}$, thermo-on ($S_{THi} = 1$)

Table A.1 Control status related to power suppression command value $L(t)$

Control status	$P(t) > k_L L(t)$	$P(t) = k_L L(t)$	$P(t) < k_L L(t)$
S_{OV}^{PL}	1	0	0
S_{FR}^{PL}	0	0	1

Table A.2 Control status related to temperature control power $P^*(t)$

Control status	$P(t) > P^*(t)$	$P(t) = P^*(t)$	$P(t) < P^*(t)$
S_{OV}^{TH}	1	0	0
S_{FR}^{TH}	0	0	1

and restart air-conditioning. Here, ΔT_{TH_ON} and ΔT_{TH_OFF} [℃] are the hysteresis width, and the state of S_{THi} is shifted only in the direction of the arrow as shown in Fig. A.3 to prevent frequent thermo on / off.

The cooling capacity distributed to indoor units will be explained using Fig. A.4, as an example. In Fig. A.4, six indoor units are connected to the outdoor unit. When 3 out of 6 indoor units are thermo-on, the cooling capacity exerted by the outdoor unit is distributed to the 3 indoor units. Refrigerant does not flow into the remaining three units that are thermo-off, and cooling capacity is not distributed.

The cooling capacity of the outdoor unit is distributed to the thermo-on indoor unit by the ratio of the rated capacity of the indoor unit. In the case of Fig. A.4, the cooling capacity of the outdoor unit is $Q_{AC}(t) = 14$ kW, and the ratio of the indoor unit rated capacity is $C_{P1}: C_{P2}: C_{P3} = 4\ \text{kW}: 8\ \text{kW}: 16\ \text{kW} = 1:2:4$. Therefore, the indoor unit cooling capacity is distributed to $Q_{AC1}: Q_{AC2}: Q_{AC3} = 1:2:4 = 2\ \text{kW}: 4\ \text{kW}: 8\ \text{kW}$ and modeled it.

In this way, the change in air-conditioning power $P(t)$ and the accompanying change in capacity to each air-conditioner, the change in each room temperature $T_{Ai}(t)$, and each setting in response to the power limit command $L(t)$ of the building multi-type air-conditioner. So, a physical model of thermo on/off behavior with temperature is obtained.

Appendix B Thermal Load Model of Standard Office Building

As shown in Eq. (A.4), the room heat capacity C_{Hi} [kJ/°C], the room heat load $Q_{Li}(t)$ [kW], the air-conditioning capacity $Q_{ACi}(t)$ [kW], and the room temperature $T_{AIRi}(t)$ [°C], the following heat balance relationship holds.

$$C_{Hi}\frac{T_{Ai}(t)}{dt} = \ Q_{Li}(t) - Q_{ACi}(t) \tag{B.1}$$

That is, room temperature responds slowly in rooms with relatively large heat capacity C_{Hi}, and responds quickly in small rooms. In a room with a large thermal load $Q_{Li}(t)$, the room temperature rises quickly when the thermostat is off ($Q_{ACi}(t) = 0$), and in a room with a small $Q_{Li}(t)$, the room temperature rises slowly. Thus, the dynamic characteristics at room temperature change depending on the heat capacity C_{Hi} and the heat load $Q_{Li}(t)$, so these must be estimated reasonably.

C_{Hi} and $Q_{Li}(t)$ are clarified by developing a building heat balance model for the section in charge of one indoor unit of the hypothetical office building shown in Fig. B.3. $Q_{Li}(t)$ is composed of the Eq. (B.2).

$$Q_{Li}(t) = \ Q_O(t) + Q_R(t) + Q_I(t) \ \ A_R = L_C \cdot S_C \tag{B.2}$$

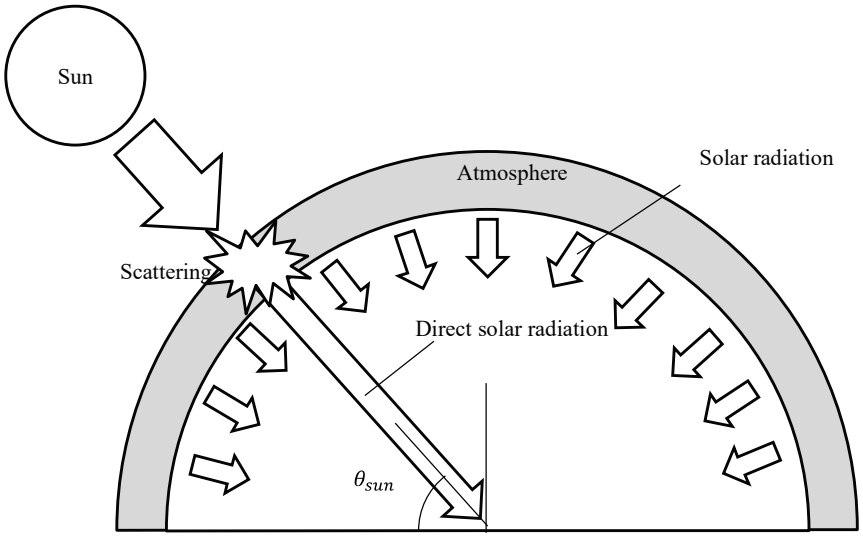

Fig. B.1 Direct solar radiation and sky solar radiation

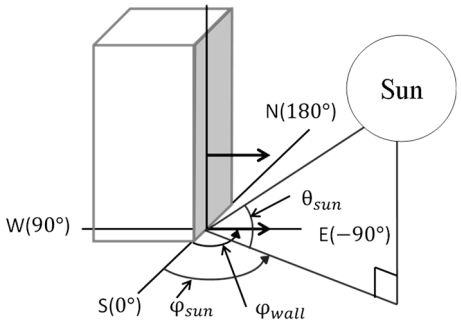

Fig. B.2 Solar altitude and direction

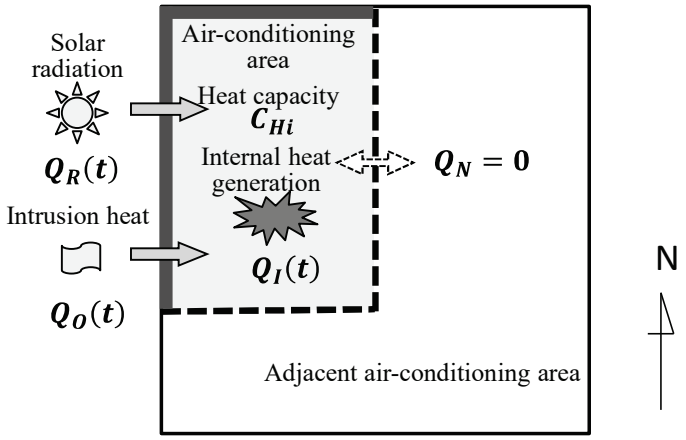

Fig. B.3 Example office building for heat balance calculation

Where $Q_O(t)$ [kW] is the intrusion heat load from the outer wall, floor, and ceiling, $Q_R(t)$ [kW] is the solar radiation load that passes through the window glass, and $Q_I(t)$ [kW] is the internal heat load. Adjacent compartments are assumed to be air-conditioned, and there is no Q_N of heat in and out of the compartments.

1) Calculation of Heat Capacity of Indoor Unit Air-conditioning Section

First, obtain the heat capacity C_{Hi} of the air-conditioning section of each indoor unit. When the air-conditioner is in operation, it cools not only room air but also walls and ceilings at the same time. Therefore, the total heat capacity of room air, floor, outer wall, window glass, ceiling, and partition is used as the heat capacity of the compartment.

In addition, this fictitious office building is composed of the members shown in Fig. B.4 as an example. The room dimensions are vertical L_C [m], horizontal S_C [m], and the height to the

ceiling H_C [m]. It was assumed that the west side of the room consisted of an outer wall and window glass, only the outer wall on the north side, and a partition on the south side.

At this time, the floor surface area A_R [m^2] is as in Eq. (B.3).

$$A_R = L_C \cdot S_C \tag{B.3}$$

Next, the window glass area A_G [m^2] is as in Eq. (B.4), assuming that the height of the window glass is H_G [m].

$$A_G = L_C \cdot H_G \tag{B.4}$$

The outer wall is located on the north and west sides, and its area A_W [m^2] is as Eq. (B.5).

$$A_W = L_C \cdot (H_C - H_G) + S_C \cdot H_C \tag{B.5}$$

Similarly, the partition area A_P [m^2] is as Eq. (B.6).

$$A_P = S_C \cdot H_C \tag{B.6}$$

Each heat capacity [kJ/℃] of air C_A, floor C_{NF}, outer wall C_{OW}, window glass C_{WG}, ceiling C_{NC}, and partition C_{PW} is the heat capacity of the building member from the boundary between air and wall to the thickness H_T [m]. Then, using the thermal constants of the materials shown in Table B.1, it is expressed as Eq. (B.7).

$$C_A = C_{PA} \cdot A_R \cdot H_C \tag{B.7}$$

$$C_{NF} = C_{PF1} \cdot A_R \cdot H_{TC} + C_{PF2} \cdot A_R \cdot (H_T - H_{TC}) \tag{B.8}$$

$$C_{OW} = C_{PO} \cdot A_W \cdot H_T \tag{B.9}$$

$$C_{WG} = C_{PG} \cdot A_G \cdot H_T \tag{B.10}$$

$$C_{NC} = C_{PC} \cdot A_R \cdot H_T \tag{B.11}$$

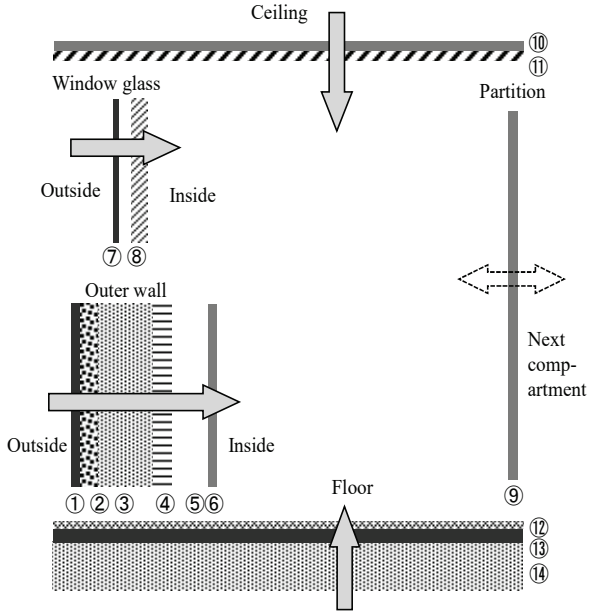

Place	Name of substance
Outer wall	① Tile
	② Cement
	③ Ordinary concrete
	④ Styro-foam
	⑤ Non-hermetic hollow layer
	⑥ Plasterboard
Window glass	⑦ Clear glass
	⑧ Light blinds
Partition	⑨ Plasterboard
Ceiling	⑩ Plasterboard
	⑪ Rock wool sound absorbing board
Floor	⑫ Carpet
	⑬ Floor P tile
	⑭ Ordinary concrete

Fig. B.4 Example of building materials for a fictitious office building

$$C_{PW} = C_{PO} \cdot A_P \cdot H_T \tag{B.12}$$

H_{TC} [m] is the carpet thickness. Therefore, the total heat capacity C_{Hi} subject to air-conditioning is becomes as Eq. (B.13).

$$C_{Hi} = C_A + C_{NF} + C_{OW} + C_{WG} + C_{NC} + C_{PW} \tag{B.13}$$

2) Calculation of External Intrusion Heat Load Q_O

Now, the intrusion heat from the outside of the room is calculated by Eq. (B.14).

$$Q_O(t) = Q_{OW}(t) + Q_{OC}(t) + Q_{OF}(t) + Q_{OG}(t) \tag{B.14}$$

$Q_{OW}(t)$ [kW] is the penetration heat from the outer wall, $Q_{OC}(t)$ [kW] is the penetration heat from the ceiling, $Q_{OF}(t)$ [kW] is the penetration heat from the floor, $Q_{OG}(t)$ [kW] is the window glass It is intrusion heat. The reason for dividing by 1000 is to convert the unit from [W] to [kW].

At this time, intrusion heat from the outer wall considers not only the outside temperature but also the influence of solar radiation. Solar radiation is absorbed by the surface and travels through

Table B.1 Thermal constants of office building materials

Name of item	Symbol	Volumetric specific heat [kJ/m³ • °C]
Plasterboard	C_{PO}	1000
Clear glass	C_{PG}	1900
Sound absorbing board	C_{PC}	26.0
Air	C_{PA}	1.3
Carpet	C_{PF1}	320
Floor tile	C_{PF2}	16.00

the wall and becomes a heat load. The effect of solar radiation is converted to an equivalent temperature, and the temperature expressed as if the outside air temperature has risen is called the equivalent outside air temperature SAT (Sol Air Temperature) [°C].

Furthermore, the intruding heat from the outer wall becomes a thermal load in the room with a time delay due to the heat capacity of the wall, so Eq. (B.15) is used: ETD (Equivalent Temperature Difference) [°C].

$$ETD(t) = \frac{\sum_{n=0}^{23} \phi_n \cdot SAT_{h-n}}{K_W} - T_{AIRi}(t) \tag{B.15}$$

Where h [hours] is the current time (0 to 23), ϕ_n [W/(m² · °C)] is the through-wall thermal response coefficient, and K_W [W/(m² · °C)] is the heat transmittance and has Eq. (B.16).

$$K_W = \sum_{n=0}^{23} \phi_n \tag{B.16}$$

From the above, the once-through heat load $Q_{OW}(t)$ [kW] is obtained by Eq. (B.17).

$$Q_{OW}(t) = K_W A_W ETD(t) \tag{B.17}$$

$$K_W = \frac{1}{\frac{1}{a_O} + \sum_{e=1}^{N_e} \frac{d_e}{\lambda_e} + \frac{1}{a_I}} \tag{B.18}$$

Where a_o [W/m² · °C] is the outer surface heat transfer coefficient, N_e is the number of

outer wall members, d_e [m] is the thickness of member number e, and λ_e [W/m · °C] is the heat conductivity of member e, a_I [W/m^2 · °C] is the inner surface heat transfer coefficient.

In addition, ETD(t) may be calculated by Eq. (B.19) using the effective temperature difference at the representative points, without using the once-through heat response coefficient ϕ_n.

$$ETD(t) = ETD_T(h) + \left(T_O(t) - T_{OT}(h)\right) - (T_{Ai}(t) - T_{AT}) \quad \text{(B.19)}$$

Where $ETD_T(h)$ [°C] is the effective temperature difference obtained from the effective temperature difference table at time h, $T_O(t)$ is the outside temperature, $T_{OT}(h)$ is the standard outside temperature, and T_{AT} is the standard Temperature (summer 26 °C, intermediate period 24 °C). $T_{OT}(h)$ is the value obtained by adding T_{AT} to the value $ETD_{T0}(h)$ [°C] of "Wall type 0" in the effective temperature difference table. That is, it is expressed as follows.

$$T_{OT}(h) = ETD_{T0}(h) + T_{AT} \quad \text{(B.20)}$$

From the above, the heat of penetration from the wall can be obtained. Furthermore, in the case of the top floor, it is necessary to consider the intrusion heat $Q_{OC}(t)$ [kW] from the ceiling. In this case, it is calculated by the following formula and added to the heat load.

$$Q_{OC}(t) = K_C \cdot A_R \cdot ETD_C(t) \quad \text{(B.21)}$$

Here, K_C [W/(m^2 · °C)] is the heat transfer rate of the ceiling, and is obtained in the same way as Eq. (B.8). ETD_C is the ceiling temperature difference and is calculated separately from the wall surface.

On the other hand, in the case of the ground floor, add the thermal load Q_{NF} from the floor. The floor is not affected by solar radiation, but instead has a once-through heat load due to temperature differences. This is expressed by Eq. (B.22).

$$Q_{NF}(t) = K_{IW} \cdot A_R \cdot (T_O(t) - T_{Ai}(t)) \cdot f_{IW} \quad \text{(B.22)}$$

Here, K_{IW} [kW/m^2.°C] is the heat transfer rate of the floor and f_{IW} is the temperature difference coefficient between inside and outside (0.0 to 1.0). The intrusion heat load from the

window glass is obtained by the following formula.

$$Q_{OG} = K_G \cdot A_G \cdot (T_O(t) - T_A(t)) \quad \text{(B.23)}$$

Here, K_G [W/(m^2 · °C)] is the heat transfer rate of glass. The Eq. (B.23) is the heat transfer due to the difference between the outside temperature and room temperature and the intrusion heat as heat conduction, and the solar radiation load is calculated separately as explained in (3) below.

3) Calculation of Solar Radiation Load

The thermal load Q_{OR} due to solar radiation that passes through the window glass can be obtained as Eq. B.24.

$$Q_R(t) = \frac{1}{1000}(I_G(h)SCA_G) \quad \text{(B.24)}$$

Where *SCA* is the shielding factor (0.0 to 1.0) of the glass. $I_G(h)$ is the glass window standard solar radiation acquisition [W/m^2], and the value of time h is used from the glass window standard solar radiation acquisition. However, this table only describes the summer and clear weather at the representative point, so it is necessary to correct the values if the conditions are different.

4) Internal Heating Load Calculation Q_I

General office buildings are assumed, the heat generated by people, lighting, and office automation equipment is defined as the internal heating load Q_I.

$$Q_I(t) = (Q_{IH}(t) + Q_{IL}(t) + Q_{IO}(t)) \quad \text{(B.25)}$$

Here, Q_{IH} [kW] is the heat load from the occupants, Q_{IL} [kW] is the heat load due to lighting, and Q_{IO} [kW] is the heat load of the OA equipment.

First, the heat load Q_{IH} from personnel in the room is obtained. Human fever has a sensible heat load due to the temperature difference between body temperature and room temperature, and a latent heat load due to sweating and breathing.

$$Q_{IH} = (SH + LH) \cdot N_H(t) \tag{B.26}$$

Here, *SH* [kW / person] is the sensible heat value of the person, and *LH* [kW / person] is the latent heat value. $N_H(t)$ is the number of people in the room.

Next, the heat load due to lighting is obtained by the following formula.

$$Q_{IL}(t) = \varepsilon_L E_L A_R \varphi_L(t) \tag{B.27}$$

Here, ε_L [kW / kW] is the heating value per 1 kW of lighting, E_{IL} [kW /m2] is the lighting power density , and $\varphi_L(t)$ is the operating rate of lighting (0.0 to 1.0).

As heat generation of OA equipment, heat generation $Q_{IP}(t)$ [kW] of personal computer and heat generation $Q_{IC}(t)$ [kW] of other indoor equipment with heat generation are examined, and each heat load is obtained.

$$Q_{IO}(t) = Q_{IP}(t) + Q_{IC}(t) \tag{B.28}$$

$$Q_{IP}(t) = q_{IP} N_{IP} \varphi_{IP}(t) \tag{B.29}$$

$$Q_{IC}(t) = q_{IC} N_{IC} \varphi_{IC}(t) \tag{B.30}$$

Here, $Q_{IP}(t)$ [kW] is the heat load from the personal computer, q_{IP} [W / unit] is the heat generation per notebook PC, N_{IP} is the number of units, and $\varphi_{IP}(t)$ is the operating rate (0.0 ~ 1.0). Similarly, $Q_{IC}(t)$ [kW] is the heat generation of other indoor equipment that generates heat, N_{IC} is the number of units, and $\varphi_{IC}(t)$ is the operating rate (0.0 ~ 1.0).

In this way, an example of obtaining a physical model of a building multi-type air-conditioning heat load assuming a fictitious office building structure, building materials, outside air and solar radiation was shown.

References

[1] United Nations : “Report of the Conference of the Parties on its twenty-first session, held in Paris from 30 November to 13 December 2015”, Framework Convention on Climate Change, Paris, France (2016)

[2] International Energy Agency : “Energy Policies of IEA Countries: Japan 2016”, (2016)

[3] International Energy Agency : “Energy Policy Review: Japan 2021”, (2021)

[4] S. L. Barba, M. de la Torre and M. Ordiales : “New Challenges for Operation of Systems with Large Renewable Capacity”, IEEE Power and Energy Society General Meeting, pp. 1-6 (2012)

[5] International Energy Agency : “The Power of Transformation”, (2015)

[6] International Energy Agency : “System Integration of Renewables: An update on Best Practice”, (2018)

[7] S. Shivashanjar, S. Mekhilef, H. Mokhlis and M. Karimi : “Mitigating Methods of Power Fluctuation Of Photovoltaic (PV) Sources–A Review”, Renewable and Sustainable Energy, Vol. 59, pp. 1170-1184 (2016)

[8] P. Sorensen, N. A. Cutululis, A. V. Rodríguez, L. E. Jensen, J. Hjerrild, M. H. Donovan and H. Madsen : “Power Fluctuations from Large Wind Farms”, IEEE Transactions on Power Systems, Vol. 22, No. 3, pp. 958-965 (2007)

[9] S. Eftekharnejad, V. Vittal, G. T. Heydt, B. Keel, and J. Loehr : “Impact of Increased Penetration of Photovoltaic Generation on Power Systems”, IEEE Transactions on Power Systems, Vol. 28, No. 2, pp. 893–901 (2013)

[10] P. Pijarski, P. Kacejko and S. Adamek : “Analysis of Voltage Conditions in Low Voltage Networks Highly Saturated with Photovoltaic Micro Installations”, Acta Energetica, pp. 4–9 (2018)

[11] IEEE Power and Energy Society : “IEEE 1453—IEEE Recommended Practice for the Analysis of Fluctuating Installations on Power Systems”, IEEE: Piscataway, NJ, USA, (2015)

[12] P. Pakonen, A. Hilden, T. Suntio and P. Verho : “Grid-connected PV Power Plant Induced Power Quality Problems—Experimental Evidence”, 18th European Conference on Power Electronics and Applications (EPE’16 ECCE Europe), pp. 1–10, Karlsruhe, Germany, (2016)

[13] V. Calderaro, V. Galdi, F. Lamberti, A. Piccolo and G. Graditi : “Voltage Support Control of

Unbalanced Distribution Systems by Reactive Power Regulation", IEEE PES Innovative Smart Grid Technologies, pp. 1-5, Europe, (2014)

[14] S. Eftekharnejad, V. Vittal, G. T. Heydt, B. Keel, and J. Loehr : "Impact of Increased Penetration of Photovoltaic Generation on Power Systems", IEEE Transactions on Power Systems, Vol. 28, No. 2, pp. 893–901 (2013)

[15] M. Farivar, C. R. Clarke, S. H. Low, and K. M. Chandy : "Inverter Var Control for Distribution Systems with Renewables", 2011 IEEE International Conference on Smart Grid Communications (SmartGridComm), pp. 457–462 (2011)

[16] D. Montenegro and M. Bello : "Coordinating Control Devices and Smart Inverter Functionalities in the Presence of Variable Weather Conditions", 2018 IEEE/PES Transmission and Distribution Conference and Exposition (T&D), pp. 1-9 (2018)

[17] P. Radatz, C. H. S. Rocha, J. Peppanen and M. Rylander : "Advances in OpenDSS Smart Inverter Modelling for Quasi-static Time-series Simulations", CIRED 2020 Berlin Workshop (CIRED 2020), pp. 243-246 (2020)

[18] E. DallAnese, S. V. Dhople, B. B. Johnson, and G. B. Giannakis : "Decentralized Optimal Dispatch of Photovoltaic Inverters in Residential Distribution Systems", IEEE Transactions on Energy Conversion, Vol. 29, No. 4, pp. 957–967 (2014)

[19] N. Lu, "An Evaluation of the HVAC Load Potential for Providing Load Balancing Service," IEEE Transactions on Smart Grid, Vol. 3, pp. 1263– 1270 (2012)

[20] H. Hao, B. M. Sanandaji, K. Poolla, and T. L. Vincent : "Aggregate Flexibility of Thermostatically Controlled Loads", IEEE Transactions on Power Systems, vol. 30, pp. 189–198 (2015)

[21] W. Zhang, J. Lian, C. Chang, and K. Kalsi : "Aggregated Modeling and Control of Air Conditioning Loads for Demand Response", IEEE Transactions on Power Systems, Vol. 28, pp. 4655–4664 (2013)

[22] N. Lu and Y. Zhang : "Design Considerations of a Centralized Load Controller using Thermostatically Controlled Appliances for Continuous Regulation Reserves", IEEE Transactions on Smart Grid, Vol. 4, pp. 914– 921 (2013)

[23] P. Palensky and D. Dietrich : "Demand Side Management: Demand Response, Intelligent Energy Systems, and Smart Loads", IEEE Transactions on Industrial Informatics, Vol. 7, No. 3, pp. 381-388

(2011)

[24] V. S. K. Murthy Balijepalli, V. Pradhan, S. A. Khaparde and R. M. Shereef : “Review of Demand Response under Smart Grid Paradigm”, ISGT2011-India, pp. 236-243 (2011)

[25] U.S. Department Of Energy (U.S. DOE) : “Getting Started with EnergyPlus: Basic Concepts Manual - Essential Information You Need about Running EnergyPlus”, p. 67 (2010)

[26] W. Goetzler : “Variable Refrigerant Flow Systems”, ASHRAE Journal 2007, pp. 24-31 (2007)

[27] Japan Refrigeration and Air Conditioning Industry Association : “Trends in Domestic Shipments of Commercial (Package) Air Conditioners”, https://www.jraia.or.jp/statistic/s_com_aircon.html (Until March 24, 2020)

[28] S. C. Dhulipala, R. V. A. Monteiro, R. F. d. Silva Teixeira, C. Ruben, A. S. Bretas and G. C. Guimarães : “Distributed Model-Predictive Control Strategy for Distribution Network Volt/VAR Control: A Smart-Building-Based Approach", IEEE Transactions on Industry Applications, Vol. 55, No. 6, pp. 7041-7051 (2019)

[29] Energies : “Distributed Energy Resources Management 2018”, (2019)

[30] A. Renjit : “Distributed Energy Resources Management Systems Reference Control Methods”, EPRI, Doc. No.3002014467 (2018)

[31] IEEE : “IEEE Guide for Distributed Energy Resources Management Systems (DERMS) Functional Specification”, IEEE Std 2030.11 (2021)

[32] I. Rahman, N. Selak and E. Paaso : “Distributed Energy Resource Management System (DERMS) solution for feeder Voltage Management for Utility integrated DERs”, 2021 IEEE Power & Energy Society Innovative Smart Grid Technologies Conference (ISGT), pp. 1-5 (2021)

[33] J. Wang, J. Huang and X. Zhou : “Performance Evaluation of Distributed Energy Resource Management Algorithm in Large Distribution Networks”, IEEE Power & Energy Society General Meeting (PESGM), pp. 1-5 (2021)

[34] R. Maeda, T. Fukuoka, Y. Yoshioka, A. Harada : “Expectation for Smart Inverter & DERMS for Electric Power System Task”, IEEJ Transactions on Power and Energy, Vol.138, No.6, pp.412-415 (2018)

[35] Q. Li, Y. Zhang, T. Ji, X. Lin and Z. Cai : “Volt/Var Control for Power Grids with Connections of Large-Scale Wind Farms: A Review”, IEEE Access, Vol. 6, pp. 26675-26692 (2018)

[36] C. Ninagawa : “Virtual Power Plant System Integration Technology”, Springer (2021)

[37] K. Thulasiraman, M. Yadav and K. Naik : “Network Science Meets Circuit Theory: Resistance Distance, Kirchhoff Index, and Foster’s Theorems With Generalizations and Unification”, IEEE Transactions on Circuits and Systems I: Regular Papers, Vol. 66, No. 3, pp. 1090-1103 (2019)

[38] X. Zhu, J. Wang, N. Lu, N. Samaan, R. Huang and X. Ke : “A Hierarchical VLSM-Based Demand Response Strategy for Coordinative Voltage Control Between Transmission and Distribution Systems”, IEEE Transactions on Smart Grid”, Vol. 10, No. 5, pp. 4838-4847 (2019)

[39] J. Grainger, W. D. Stevenson, “Power System Analysis”, Chapter 9, (1994)

[40] O. Ma, N. Alkadi, P. Cappers, P. Denholm, J. Dudley, S. Goli, M. Hummon, S. Kilcote, J. MacDonald, N. Matson, D. Olsen, C. Rose, M. Sohn, M. Starke, B. Kirby and M. O'malley : “Demand Response for Ancillary Services”, IEEE Transactions on Smart Grid, Vol. 4, No. 4, pp. 1988-1995 (2013)

[41] H. Hao, Y. Lin, A. S. Kowli, P. Barooah, and S. Meyn : “Ancillary Service to the Grid Through Control of Fans in Commercial Building HVAC Systems”, IEEE Transactions on Smart Grid, Vol. 5, No. 4, pp. 2066-2074 (2014)

[42] Y. Lin, P. Barroah, S. Meyen and T. Middlekoop : “Experimental Evaluation of Frequency Regulation From Commercial Building HVAC Systems”, IEEE Transactions on Smart Grid, Vol. 6, No. 2, pp. 776-783 (2015)

[43] K. Ma, G. Hu and C. Spanos : “Distributed Energy Consumption Control via Real-Time Pricing Feedback in Smart Grid”, IEEE Transactions on Control System Technology, Vol. 22, No. 5, pp. 1907-1914 (2014)

[44] S. Noh, J. Yun and K. Kim : “An Efficient Building Air-Conditioning System Control Under Real-Time Pricing”, 2011 Int. Conf. on Advanced Power System Automation and Protection, pp. 1283-1286 (2011)

[45] S. Ramdaspallli, M. Pipattanasomporn, M. Kuzlu and S. Rahman : “Transactive Control for Efficient Operation of Commercial Buildings”, IEEE Innovative Smart Grid Technologies Europe ISGT Europe, pp. 1-5 (2016)

[46] J. Aguero, F. Rodriguez, M. Castilla and M. Pereira : “Productiveness and Real Time Prices in Energy Management for HVAC Systems”, 39th IEEE Conf. on Industrial Electronics IECON2013, pp. 7956-7961 (2013)

[47] I. Murata and Y. Takarada : “Modeling of Dynamics in Demand Response for Real-Time Pricing”, IEEE Int. Conf. on Smart Grid Communications, pp. 806-811 (2014)

[48] C. Ninagawa : “Distributed Building Air-Conditioner IoT/AI Control”, Gihodo Publishing Co. (2021)

[49] A. Iqbal, Y. Aoki, C. Ninagawa, J. Morikawa and S. Kondo : “Emulation Modeling on Rebound-Compensated Aggregation of Uncertain Demand Responses from a Large Number of Building Air-Conditioners”, 2020 IEEE International Symposium on Systems Engineering (ISSE), pp. 1-6 (2020)

[50] K. Yamane, D. Orihara, D. Iioka, Y. Aoto, J. Hashimoto, T. Goda : “Determination Method of Volt-Var and Volt-Watt Curve for Smart Inverters Applying Optimization of Active/Reactive Power Allocation for each Inverter”, IEEJ Transactions on Power and Energy, Vol.139, No.8, pp.513-521 (2019)

[51] IEEJ Technical Report of the Japanese Electrotechnical committee: “Energy Service by Building Air-Conditioners”, JEC-TR-59004:2019 (2019)

[52] K. Sumito, T. Kanie, T. Sato : “Development of 3-Phase Active Converter for Packaged Air Conditioners”, Mitsubishi Heavy Industries Technical Review, Vol.33, No.6, pp.416-419 (1996)

[53] H. Yamashita, P. Jintakosonwit, H. Fujita, H. Akagi, J. Shinohara, H. Hakoda : “Voltage Regulation Performance of a Shunt Active Filter Intended for Installation on a Power Distribution System”, IEEJ Transactions on Industry Applications, Vol.123, No.11, pp.1351-1358 (2003)

[54] M. Kono, K. Ota, H. Kojima, R. Kawashima : “Power Factor Control in Buildings Using Air Conditioners with Built-in Active Filters”, IEEJ Transactions on Industry Applications, Vol.141, No.4, pp.339-344 (2021)

[55] K. Kondo, J. Baba : “Evaluation of Harmonic Current Effect and Distribution Line Voltage Control Ability of Reactive Power Control by use of Power Factor Correction Converter in Consumer Load”, IEEJ Transactions on Power and Energy, Vol.139, No.11, pp.678-687 (2019)

[56] Y. Aoki, A. Iqbal, R. Okada, C. Ninagawa, T. Murakawa, M. Fujita, K. Bando: “Reactive Power Demand Response using Clusters of Building Multi-type Air-conditioners in Distribution Networks”,

IEEJ Technical Meeting on Power Engineering, PE-22-078 (2022)

[57] M. Kono, K. Ota, H. Kojima, R. Kawashima : “Power Factor Control in Buildings Using Air Conditioners with Built-in Active Filters”, IEEJ Transactions on Industry Applications, Vol.141, No.4, pp.339-344 (2021)

[58] Pacific Gas and Electric Company : “EPIC 2.02 DERMS Report”, (2019)

[59] W. Wang and A. Huque : “Oscillation Mechanism and Setting Guideline for Inverter Volt-Var Control”, EPRI White Paper, Doc. No. 3002019776 (2020)

[60] B. Seal and M. McGranaghan : “Standard Language Protocols for PV and Storage Grid Integration”, Tech. Rep., EPRI, (2010)

[61] IEEE : “IEEE Standard for Interconnection and Interoperability of Distributed Energy Resources with Associated Electric Power Systems Interfaces”, IEEE Std 1547 (2018)

[62] Y. Aoki, S. Matsukawa, S. Goto, C. Ninagawa, J. Morikawa, S. Kondo, H. Otake : “Transfer Reinforcement Learning of Area Complex Adaptive Control of Building Multi-type Air-conditioning Facilities for Real-Time Pricing”, Journal of the Society of Heating, Air-Conditioning and Sanitary Engineers of Japan, Vol.45, No.285, pp.9-16 (2020)

[63] Electric Technology Research Association : “Denki Kyodo Kenkyu”, Vol.37, No.3 (1981)

[64] R. Dugan, D. Montenegro : “Reference Guide the Open Distribution System Simulator (OpenDSS)”, EPRI (2020)

[65] MathWorks : https://www.mathworks.com/help/matlab/ref/rand.html

[66] OpenADR Alliance : “OpenADR 2.0b Profile Specification Distributed Energy Resources (DER)”, Doc. No. 20190201-2 (2019)

[67] XMPP : https://xmpp.org/

[68] R. Kuga, M. Esquerra and A. Portilla : “Distributed Energy Resource Management System”, Pacific Gas and Electric Company EPIC Final Report, p41 and pp.65-67, EPIC 2.02 DERMS (2019)

[69] S. Sardic and S. Lukic : “Towards Extreme Fast Charging”, IEEE Electrification Magazine, pp.22-31 (2019)

[70] A. Iqbal, Y. Aoki, C. Ninagawa, T. Murakawa: “Reactive Power Demand Response for Distribution

System with Neighboring Clusters of Building Multi-type Air-conditioners", IEEJ Transactions on Power and Energy, Vol.142, No.6 (2022)

[71] K. Tamiya, H. Asano, S. Bando : "A Development of an Evaluation Method of the Locational Value of Distributed Batteries as a Voltage Control Device in a Distribution System with Large Penetration of Photovoltaic Generation Systems", IEEJ Transactions on Power and Energy, Vol.140, No.9, pp.680-686 (2020)

[72] J. Morikawa and C. Ninagawa: "Fast Real-Time Pricing Optimization Control of Power Consumption and Room Temperature for Building Multi-type Air-conditioning Facilities", IEEJ Trans. on Power and Energy, Vol.136, pp.817-823 (2016) (in Japanese)

[73] Y. Aoki, H. Ito, C. Ninagawa, J. Morikawa, T. Inaba and S. Kondo : "Complex Coordina-tion Control with Entire Power Limitation and Partial Temperature Priority of Building Multi-type Air-conditioning Facilities for Real-Time Pricing", IEEJ Trans. on Industry Applications, Vol.138, No.10, pp.777-786 (2018) (in Japanese)

[74] JARN News : World VRF Market, Japan Air Conditioning, Heating & Refrigeration News (JARN), Special issue, Serial no. 628-S, (May 25, 2021)

[75] N. L. Díaz, J. C. Vasquez and J. M. Guerrero : "A Communication-Less Distributed Control Architecture for Islanded Microgrids With Renewable Generation and Storage", IEEE Transactions on Power Electronics, Vol. 33,Nno. 3, pp. 1922-1939 (2018)

[76] V. C. Cunha, R. C. Dugan, et al., : "Generalized Formulation of Steady-State Equivalent Circuit Models of Grid-Forming Inverters", IEEE Open Access Journal of Power and Energy, Vol. 8, pp. 352-364 (2021)

[77] N. S. Gurule, J. Hernandez-Alvidrez, M. J. Reno, A. Summers, S. Gonzalez and J. Flicker : "Grid-forming Inverter Experimental Testing of Fault Current Contributions", 2019 IEEE 46th Photovoltaic Specialists Conference (PVSC), pp. 3150-3155, Chicago, IL, USA (2019)

[78] Nikkei newspaper : "A new LFC Battery System Discharges within 1 Second", 7th January 2023